



Defense Threat Reduction Agency  
8725 John J. Kingman Road, MS  
6201 Fort Belvoir, VA 22060-6201



DTRA-TR-16-81

# TECHNICAL REPORT

## High-Performance Low-Cost Portable Radiological and Nuclear Detectors Based on Colloidal Nanocrystals (TOPIC 07-B)

Distribution Statement A. Approved for public release; distribution is unlimited.

July 2016

HDTRA1-08-1-0021

Marek Osinski

Prepared by:  
University of New Mexico  
1700 Lomas Blvd. NE  
Albuquerque, NM 87131

DESTRUCTION NOTICE:

Destroy this report when it is no longer needed.  
Do not return to sender.

PLEASE NOTIFY THE DEFENSE THREAT REDUCTION  
AGENCY, ATTN: DTRIAC/ J9STT, 8725 JOHN J. KINGMAN ROAD,  
MS-6201, FT BELVOIR, VA 22060-6201, IF YOUR ADDRESS  
IS INCORRECT, IF YOU WISH IT DELETED FROM THE  
DISTRIBUTION LIST, OR IF THE ADDRESSEE IS NO  
LONGER EMPLOYED BY YOUR ORGANIZATION.

# REPORT DOCUMENTATION PAGE

Form Approved  
OMB No. 0704-0188

The public reporting burden for this collection of information is estimated to average 1 hour per response, including the time for reviewing instructions, searching existing data sources, gathering and maintaining the data needed, and completing and reviewing the collection of information. Send comments regarding this burden estimate or any other aspect of this collection of information, including suggestions for reducing the burden, to Department of Defense, Washington Headquarters Services, Directorate for Information Operations and Reports (0704-0188), 1215 Jefferson Davis Highway, Suite 1204, Arlington, VA 22202-4302. Respondents should be aware that notwithstanding any other provision of law, no person shall be subject to any penalty for failing to comply with a collection of information if it does not display a currently valid OMB control number.

PLEASE DO NOT RETURN YOUR FORM TO THE ABOVE ADDRESS.

1. REPORT DATE (DD-MM-YYYY) 00-07-2016		2. REPORT TYPE Final		3. DATES COVERED (From - To) 5/Feb/2008 - 4/Feb/2012	
4. TITLE AND SUBTITLE High-Performance Low-Cost Portable Radiological and Nuclear Detectors Based on Colloidal Nanocrystals (Topic 07-B)				5a. CONTRACT NUMBER	
				5b. GRANT NUMBER #HDTRA1-08-1-0021	
				5c. PROGRAM ELEMENT NUMBER	
6. AUTHOR(S) Marek Osinski				5d. PROJECT NUMBER	
				5e. TASK NUMBER	
				5f. WORK UNIT NUMBER	
7. PERFORMING ORGANIZATION NAME(S) AND ADDRESS(ES) Regents of the University of New Mexico 1700 Lomas Blvd NE Albuquerque New Mexico 87131-0001				8. PERFORMING ORGANIZATION REPORT NUMBER	
9. SPONSORING/MONITORING AGENCY NAME(S) AND ADDRESS(ES) Defense Threat Reduction Agency John J. Kingman Road Fort Belvoir, VA 22060-6201				10. SPONSOR/MONITOR'S ACRONYM(S) DTRA	
				11. SPONSOR/MONITOR'S REPORT NUMBER(S) DTRA-TR-16-81	
12. DISTRIBUTION/AVAILABILITY STATEMENT Distribution Statement A. Approved for public release; distribution is unlimited.					
13. SUPPLEMENTARY NOTES					
14. ABSTRACT Results of basic research towards room-temperature, high-speed, high-efficiency, and high-energy-resolution portable scintillating detectors based on colloidal nanocrystals are reported. Novel scintillating nanocrystals were synthesized for the first time, using colloidal approach. For neutron detection, the nanoparticles contain neutron capture elements, while the host polymers serve a dual role of acting as moderators and scintillators. It is expected that this project, if DTRA chooses to continue funding it, will lead to development of high-performance room-temperature portable detectors of nuclear radiation.					
15. SUBJECT TERMS Nuclear radiation detectors, Colloidal nanocrystals, Scintillating nanocrystals, High-performance room-temperature scintillating detectors, Nanoscintillators					
16. SECURITY CLASSIFICATION OF:			17. LIMITATION OF ABSTRACT  SAR	18. NUMBER OF PAGES  107	19a. NAME OF RESPONSIBLE PERSON David Petersen
a. REPORT  U	b. ABSTRACT  U	c. THIS PAGE  U			19b. TELEPHONE NUMBER (Include area code) 703-767-3164

## UNIT CONVERSION TABLE

U.S. customary units to and from international units of measurement<sup>\*</sup>

U.S. Customary Units	<div style="display: flex; align-items: center; justify-content: center;"> <div style="margin-right: 10px;"> </div> Multiply by </div> <div style="display: flex; align-items: center; justify-content: center;"> <div style="margin-right: 10px;"> </div> Divide by<sup>†</sup> </div>	International Units
<b>Length/Area/Volume</b>		
inch (in)	2.54 × 10 <sup>-2</sup>	meter (m)
foot (ft)	3.048 × 10 <sup>-1</sup>	meter (m)
yard (yd)	9.144 × 10 <sup>-1</sup>	meter (m)
mile (mi, international)	1.609 344 × 10 <sup>3</sup>	meter (m)
mile (nmi, nautical, U.S.)	1.852 × 10 <sup>3</sup>	meter (m)
barn (b)	1 × 10 <sup>-28</sup>	square meter (m <sup>2</sup> )
gallon (gal, U.S. liquid)	3.785 412 × 10 <sup>-3</sup>	cubic meter (m <sup>3</sup> )
cubic foot (ft <sup>3</sup> )	2.831 685 × 10 <sup>-2</sup>	cubic meter (m <sup>3</sup> )
<b>Mass/Density</b>		
pound (lb)	4.535 924 × 10 <sup>-1</sup>	kilogram (kg)
unified atomic mass unit (amu)	1.660 539 × 10 <sup>-27</sup>	kilogram (kg)
pound-mass per cubic foot (lb ft <sup>-3</sup> )	1.601 846 × 10 <sup>1</sup>	kilogram per cubic meter (kg m <sup>-3</sup> )
pound-force (lbf avoirdupois)	4.448 222	newton (N)
<b>Energy/Work/Power</b>		
electron volt (eV)	1.602 177 × 10 <sup>-19</sup>	joule (J)
erg	1 × 10 <sup>-7</sup>	joule (J)
kiloton (kt) (TNT equivalent)	4.184 × 10 <sup>12</sup>	joule (J)
British thermal unit (Btu) (thermochemical)	1.054 350 × 10 <sup>3</sup>	joule (J)
foot-pound-force (ft lbf)	1.355 818	joule (J)
calorie (cal) (thermochemical)	4.184	joule (J)
<b>Pressure</b>		
atmosphere (atm)	1.013 250 × 10 <sup>5</sup>	pascal (Pa)
pound force per square inch (psi)	6.984 757 × 10 <sup>3</sup>	pascal (Pa)
<b>Temperature</b>		
degree Fahrenheit (°F)	[T(°F) - 32]/1.8	degree Celsius (°C)
degree Fahrenheit (°F)	[T(°F) + 459.67]/1.8	kelvin (K)
<b>Radiation</b>		
curie (Ci) [activity of radionuclides]	3.7 × 10 <sup>10</sup>	per second (s <sup>-1</sup> ) [becquerel (Bq)]
roentgen (R) [air exposure]	2.579 760 × 10 <sup>-4</sup>	coulomb per kilogram (C kg <sup>-1</sup> )
rad [absorbed dose]	1 × 10 <sup>-2</sup>	joule per kilogram (J kg <sup>-1</sup> ) [gray (Gy)]
rem [equivalent and effective dose]	1 × 10 <sup>-2</sup>	joule per kilogram (J kg <sup>-1</sup> ) [sievert (Sv)]

<sup>\*</sup> Specific details regarding the implementation of SI units may be viewed at <http://www.bipm.org/en/si/>.

<sup>†</sup> Multiply the U.S. customary unit by the factor to get the international unit. Divide the international unit by the factor to get the U.S. customary unit.

FINAL REPORT

**DTRA Basic Research Grant HDTRA1-08-1-0021**

SUBMITTED TO:

DEFENSE THREAT REDUCTION AGENCY  
8725 JOHN J. KINGMAN ROAD, MSC 6201, FORT BELVOIR, VA 22060-6201

Technical Point of Contact:

DR. MICHAEL ROBINSON, Chief, Physical Sciences Division, Basic and Applied Sciences Directorate  
Tel. (703) 767-3076  
Fax (703) 767-3387  
Email: michael.robinson@dtra.mil

TITLE:

**HIGH-PERFORMANCE LOW-COST PORTABLE RADIOLOGICAL AND  
NUCLEAR DETECTORS BASED ON COLLOIDAL NANOCRYSTALS  
(TOPIC 07-B)**

*Principal Investigator:*

**PROF. MAREK OSIŃSKI**

Period of performance: 5 Feb. 2008 – 4 Feb. 2012

**Original submission date: 8 February 2013, revised report submitted on 29 September 2015**

Prepared by:

MAREK OSIŃSKI  
Center for High Technology Materials  
University of New Mexico  
1313 Goddard SE  
Albuquerque, New Mexico 87106-4343  
Tel. (505) 272-7812  
Fax (505) 272-7801  
Email: osinski@chtm.unm.edu

## TABLE OF CONTENTS

	Page
List of Abbreviations.....	v
1. Objectives.....	1
2. Summary of Effort.....	1
3. Introduction.....	2
3.A. Potential Advantages of Nanoscale Devices for Nuclear Radiation Detection.....	5
3.B. Nanocrystalline Films and Pressed Ceramics.....	7
3.C. Prior Work on Nanoscintillators.....	7
4. Properties of Bulk Cerium-Doped Lanthanum Fluoride and Lanthanum Bromide.....	8
4.A. Physical Properties and Light Emission Mechanism.....	8
4.B. Radiation Absorption Parameters.....	10
5. Colloidal Synthesis of Lanthanide Halide Scintillating Nanocrystals (Task 1).....	12
5.A. Colloidal Synthesis of LaF <sub>3</sub> :Eu, LaF <sub>3</sub> :Ce, and LaF <sub>3</sub> :Ce/LaF <sub>3</sub> Scintillating Nanocrystals.....	13
5.A.a. Synthesis in Aqueous Solutions.....	13
5.A.a.i. Preparation of stock solutions.....	13
5.A.a.ii. Synthesis procedure.....	14
5.B. Colloidal Synthesis of Ce <sub>x</sub> La <sub>1-x</sub> F <sub>3</sub> Nanocrystals.....	15
5.C. Aqueous Synthesis of Ln-Doped LaF <sub>3</sub> Colloidal Nanocrystals Capped with Polyethylene Glycol.....	15
6. Colloidal Synthesis of Lead-Based Scintillating Nanocrystals (Task 2).....	15
6.A. Colloidal Synthesis of PbI <sub>2</sub> Scintillating Nanocrystals.....	16
6.B. Colloidal Synthesis of PbIOH Nanocrystals.....	17
6.C. Colloidal Synthesis of Water-Soluble Pb <sub>3</sub> O <sub>2</sub> I <sub>2</sub> Scintillating Nanocrystals.....	17
6.D. Colloidal Synthesis of Pb <sub>3</sub> O <sub>2</sub> I <sub>2</sub> Scintillating Nanocrystals in Trioctylphosphine Oxide.....	18
7. Characterization of Lanthanide Halide Scintillating Nanocrystals (Task 3, Part 1).....	18
7.A. Structural Characterization of Lanthanide Halide Nanocrystals.....	18
7.A.a. Structural Characterization of LaF <sub>3</sub> :Eu and LaF <sub>3</sub> :Ce Nanocrystals Synthesized in Aqueous Solution.....	18
7.B. Optical Characterization of Lanthanide Halide Nanocrystals.....	20
7.B.a. Optical Characterization of LaF <sub>3</sub> :Eu and LaF <sub>3</sub> :Ce Nanocrystals Synthesized in Aqueous Solution.....	20
7.C. Optimization of Ce Content in LaF <sub>3</sub> :Ce Colloidal Nanocrystals.....	24
7.C.a. Optical Characterization of Ce <sub>x</sub> La <sub>1-x</sub> F <sub>3</sub> Nanocrystals Synthesized Using Aqueous Route.....	24
7.D. Characterization of PEG-Capped LaF <sub>3</sub> Colloidal Nanocrystals Synthesized in Water...26	
7.D.a. Structural Characterization of PEG-Capped LaF <sub>3</sub> Nanocrystals Synthesized in Water.....	26
7.D.b. Optical Characterization of PEG-Capped LaF <sub>3</sub> Nanocrystals Synthesized in Water.....	27
8. Characterization of Lead-Based Scintillating Nanocrystals (Task 3, Part 2).....	28
8.A. Structural Characterization of Time-Evolving PbI <sub>2</sub> -Based Crystals.....	29
8.A.a. Transmission Electron Microscopy and Corresponding Energy-Dispersive	

Spectroscopy Analysis of Time-Evolving PbI <sub>2</sub> NCs.....	29
8.A.b. Scanning Electron Microscopy and Corresponding Energy-Dispersive Spectroscopy Analysis of Time-Evolving PbI <sub>2</sub> -Based Crystals.....	30
8.B. Optical Characterization of Time-Evolving PbI <sub>2</sub> -Based Crystals.....	31
8.B.a. Quantum Efficiency and PL Lifetime Measurements of Time-Evolving PbI <sub>2</sub> -Based Crystals.....	33
8.C. Characterization of PbIOH Nanocrystals.....	34
8.D. Characterization of Water-Soluble Pb <sub>3</sub> O <sub>2</sub> I <sub>2</sub> Nanocrystals.....	36
8.E. Characterization of Pb <sub>3</sub> O <sub>2</sub> I <sub>2</sub> Nanocrystals Synthesized in TOPO.....	38
8.E.a. Structural Characterization of Pb <sub>3</sub> O <sub>2</sub> I <sub>2</sub> Nanocrystals Synthesized in TOPO.....	38
8.E.b. Optical Characterization of Pb <sub>3</sub> O <sub>2</sub> I <sub>2</sub> Nanocrystals Synthesized in TOPO.....	39
9. Characterization of Scintillating Nanocrystals Embedded in Polymers (Task 3, Part 3).....	40
10. Demonstration of Nanocrystalline Detectors of Gamma Radiation (Task 4).....	40
10.A. Scintillation Response of LaF <sub>3</sub> :Ce Nanocrystals to Autunite.....	41
10.B. Scintillation Response of LaF <sub>3</sub> :Ce Nanocrystals to Monoenergetic Gamma Sources.....	42
10.C. Scintillation Response of PbI <sub>2</sub> -Based Nanocrystals to Autunite.....	43
10.D. Scintillation Response of Pb <sub>3</sub> O <sub>2</sub> I <sub>2</sub> Nanocrystals to Monoenergetic Gamma Sources.....	45
11. Study of Nanocrystal Reliability under Gamma Irradiation (Task 5).....	46
11.A. Eberline Source Calibration.....	46
11.B. Exposure to Dose Conversion.....	48
11.C. Effects of Gamma Irradiation on Colloidal Nanocrystals.....	48
11.D. Rapid Degradation of CdSe/ZnS Colloidal QDs Exposed to Gamma Irradiation.....	50
11.D.a. Synthesis of CdSe/ZnS Colloidal QDs.....	50
11.D.b. Gamma Irradiation Testing.....	50
11.D.c. Mechanisms of Rapid Degradation under Gamma Irradiation.....	52
12. Numerical Simulation of Gamma Detection in Nanocrystals (Task 6).....	54
13. Colloidal Synthesis of Lanthanide Halide Nanocrystals with Neutron Captors (Task 7).....	54
13.A. Gadolinium as a Neutron Detector.....	54
13.B. Colloidal Synthesis of LaF <sub>3</sub> :Gd, GdF <sub>3</sub> , and GdF <sub>3</sub> :Ce Nanocrystals.....	55
13.C. Characterization of LaF <sub>3</sub> :10%Gd <sup>3+</sup> , GdF <sub>3</sub> , and GdF <sub>3</sub> :Ce <sup>3+</sup> Nanocrystals.....	56
13.C.a. Structural Characterization of LaF <sub>3</sub> :10%Gd <sup>3+</sup> , GdF <sub>3</sub> , and GdF <sub>3</sub> :Ce <sup>3+</sup> Nanocrystals.....	56
13.C.b. Optical Characterization of LaF <sub>3</sub> :10%Gd <sup>3+</sup> , GdF <sub>3</sub> , and GdF <sub>3</sub> :Ce <sup>3+</sup> Nanocrystals.....	59
14. Colloidal Synthesis and Characterization of Gd-Containing Nanocrystals for Neutron Detection (Modified Task 8).....	60
14.A. Colloidal Synthesis of Undoped and Doped Gd <sub>2</sub> O <sub>3</sub> Scintillating Nanocrystals Capped with Oleic Acid.....	60
14.B. Characterization of Undoped and Doped Gd <sub>2</sub> O <sub>3</sub> Scintillating Nanocrystals Capped with Oleic Acid.....	61
14.B.a. Structural Characterization of Undoped and Doped Gd <sub>2</sub> O <sub>3</sub> Scintillating Nanocrystals Capped with Oleic Acid.....	61
14.B.b. Optical Characterization of Undoped and Doped Gd <sub>2</sub> O <sub>3</sub> Scintillating Nanocrystals Capped with Oleic Acid.....	63

14.C. Nanocomposite PVT Loaded with $Gd_2O_3:10\%Ce$ NCs.....	66
14.C.a. Loading Gadolinium Oxide NCs into Poly(Vinyl Toluene).....	66
14.C.b. Optical Characterization of Gadolinium Oxide NCs Loaded into Poly(Vinyl Toluene).....	66
15. Numerical Simulation of Neutron Detection in Nanocrystals (Task 9).....	67
15.A. MCNPX Simulations of $Gd_2O_3$ Response to $^{252}Cf$ .....	67
16. Demonstration of Nanocrystalline Detectors of Neutron Radiation (Task 10).....	71
16.A. Scintillation Event Measurement Setup.....	71
16.B. Gamma-Ray Detection Experiments.....	72
16.C. Thermal Neutron Detection Experiments with Gd-Containing $LnF_3$ Nanocrystals.....	73
16.D. Thermal Neutron Detection Experiments with Gd-Containing $Ln_2O_3$ Nanocrystals....	76
16.D.a. Thermal Neutron Detection Experiments with Gd-Containing $Ln_2O_3$ Nanocrystals Suspended in Toluene.....	76
16.D.b. Thermal Neutron Detection Experiments with Gadolinium Oxide NCs Loaded into Poly(Vinyl Toluene).....	77
17. References.....	80
18. Personnel Supported.....	89
19. Publications.....	92
20. Interactions/Transitions.....	93
21. New Discoveries, Inventions, or Patent Disclosures.....	95
22. Honors/Awards.....	95



## **LIST OF ABBREVIATIONS**

2D – two-dimensional  
3D – three-dimensional  
CHTM - Center for High Technology Materials  
CNC – colloidal nanocrystal  
CWO – cadmium tungstate  
DDA – dodecylamine  
DEG – diethylene glycol  
DHS – Department of Homeland Security  
DI – de-ionized  
DLS – dynamic light scattering  
DMSO – dimethyl sulfoxide  
DTT – dithiothreitol  
ECE – Electrical and Computer Engineering  
EDS – energy-dispersive spectroscopy  
FLN – fluorescence line-narrowing  
FWHM – full width at half maximum  
HRTEM – high-resolution TEM  
HVL – half-value layer  
ICSD - Inorganic Crystal Structure Database  
LD QCS - low-dimensional quantum confinement system  
LEDs – light-emitting diodes  
LuAG – lutetium aluminum garnet  
LYSO – lutetium yttrium oxyorthosilicate  
MCA – multi-channel analyzer  
NC – nanocrystal  
NIST – National Institute for Standards and Technology  
ORNL – Oak Ridge National Laboratory  
PEG – polyethylene glycol  
PET – positron emission tomography  
PL – photoluminescence  
PLE – photoluminescence excitation  
PMT – photomultiplier tube  
PVT – polyvinyl toluene  
QD – quantum dot  
QE – quantum efficiency  
RT - room temperature  
SEM – scanning electron microscopy  
TEM - transmission electron microscopy  
THF – tetrahydrofuran  
TOF – time of flight  
TOP – trioctylphosphine  
TOPO – trioctylphosphine oxide  
UNM - University of New Mexico  
UV – ultraviolet

VIS – visible

VT – vinyl toluene

## **1. OBJECTIVES**

This project was in support of DTRA's Basic Research Program for Combating Weapons of Mass Destruction. It addresses the following Topic in the HDTRA1-07-BRCWMD Broad Agency Announcement: *07-B. Advanced Radiological-Nuclear Detection and Forensics*.

The objective of this project was to conduct basic research on low-cost, room-temperature, high-speed, high-efficiency, and high-energy-resolution portable scintillating detectors based on colloidal nanocrystals. Initially, colloidal synthesis methods for novel lead- and lanthanide-halide-based nanocrystals was developed. Extensive optical and structural characterization was performed. The plan was to protect hygroscopic cores synthesized in a glovebox filled with argon and with < 0.1 ppm levels of oxygen and water vapor by higher-bandgap stable hydrophobic shells. Subsequently, the nanocrystals were to be dispersed in liquid, porous glass, and aerogel hosts and their response to gamma irradiation was to be investigated. Performance of undoped nanocrystals was to be compared with nanocrystals containing activating dopants, such as Ce. For neutron detection, the host materials was to contain neutron capture isotopes, using boron and lithium compounds enriched in  $^{10}\text{B}$  and  $^6\text{Li}$ . Direct doping of the nanocrystals with neutron capture isotopes was also explored. Interaction between the incident nuclear radiation and nanocrystalline scintillators was simulated numerically to assist in optimizing the detector design. It was expected that this project would pave the way towards development of low-cost high-performance room-temperature portable detectors of nuclear radiation.

The ultimate objective of the proposed basic research was ***demonstration of nuclear radiation detectors based on colloidal nanocrystals with unprecedented performance***, in terms of higher efficiencies, higher energy resolution, faster speed, and improved robustness compared to current scintillators.

All the objectives of this project remained as stated in the original proposal.

## **2. SUMMARY OF EFFORT**

The following Technical Research Tasks were planned for Year 1 of this project (ending on Feb. 4, 2009):

- Task 1: Colloidal synthesis of lanthanide halide scintillating nanocrystals
- Task 2: Colloidal synthesis of  $\text{PbI}_2$  scintillating nanocrystals
- Task 3: Structural and optical characterization of nanocrystals
- Task 4: Demonstration of nanocrystalline detectors of gamma radiation

The following Technical Research Tasks were planned for Year 2 of this project (ending on Feb. 4, 2010):

- Task 5: Study of NC reliability under gamma irradiation
- Task 6: Numerical simulation of gamma detection in NCs
- Task 7: Colloidal synthesis of lanthanide halide NCs with neutron captors

The following Technical Research Tasks were planned for Year 3 of this project (ending on Feb. 4, 2011):

Task 8: Colloidal synthesis of  $\text{PbI}_2$  NCs with neutron captors

Task 9: Numerical simulation of neutron detection in NCs

Task 10: Demonstration of nanocrystalline detectors of neutron radiation

The project then went into its no-cost-extension year and ended on Feb. 4, 2012. Tasks 1, 3, 6, 8, and 9 continued to be our major activities during the no-cost-extension year. It should be noted that the due date of September 1, 2010 for the Annual Progress Report falls in the middle of the no-cost-extension year, hence the current report describes only a portion of the activities planned to occur during that year. As described in detail in this report, we have successfully completed all of the proposed tasks.

### **3. INTRODUCTION**



Fig. 3.1. “Compact” electrically cooled high- purity Ge gamma ray detector system [Katagiri 2003].

Nuclear radiation detectors are becoming increasingly important for a wide range of applications, including the homeland security against catastrophic terrorist threats, nuclear forensic analysis, monitoring treaty compliance, counterproliferation, long term monitoring of nuclear waste storage sites, environmental safety, use of nuclear waste energy, high energy physics, biomedical imaging (PET, radiotherapy), industrial defectoscopy, and oil well logging. An ideal nuclear detector should combine a number of features presently distributed among many different types of detectors: high energy resolution, high sensitivity, high efficiency, room-temperature (RT) operation, scalability, robustness, *etc.* For example, high energy resolution of better than 0.2% at 1.33 MeV can be achieved using bulk high-purity Ge detectors [Katagiri 2003]. However, the need to cool down the detector to 110 K results in a “compact” system of a vacuum cleaner size (Fig. 3.1). CdZnTe detectors offer good RT performance with 1% energy resolution at 662 keV [Verger 2005], but their linear size is limited to a few cm. The most commonly used  $\text{NaI:Tl}^+$  scintillating crystals can be grown in large size and operate at RT, but at the expense of poorer energy resolution of ~6-7% at 662 keV [Shah 2004], high hygroscopicity, and poor shock resistance. The tradeoffs between different detectors become even more apparent when other parameters are considered, such as high speed, low cost, good proportionality, high stopping power, portability, resistance to shock, and so on. Nanotechnology offers new prospects for meeting those competing requirements.

In contrast to ample literature on scintillators based on large-size crystals, there have been only a handful of reports on radiation response of colloidal nanocrystals (CNCs). The term “scintillation” is sometimes, perhaps confusedly, used to indicate wavelength conversion from UV to the visible [Mutlugun 2007], [Mutlugun 2008]. In this report, we consider scintillation to mean optical response (visible or UV) to ionizing radiation.

CNCs are particles with the dimensions on the scale of 5-50 nanometers across, synthesized by chemical processes. At these scales, the crystals exhibit enhanced quantum mechanical effects such as bandgap widening, decrease in carrier lifetime, and the dominance of surface effects. The chemical assembly of these materials is commonly known as “bottom up” nanotechnology, where self-assembly is used to create large quantities of nanoscale materials that would be prohibitively expensive to create using other techniques such as e-beam lithography.

CNCs have attracted tremendous interest over the last few years for a wide range of biomedical applications [Osiński 2006], [Osiński 2007], [Osiński 2008], [Osiński 2009], [Osiński 2010], [Parak 2011], [Parak 2012], to produce fast efficient phosphors for light emitting diodes [Chander 2005], [Matsui 2005], [Chen 2006a], [Li 2007], as active element in photovoltaic devices [Klimov 2006], [Gupta 2009], in biochemical sensing [Sommers 2007], and as photocatalysts [Tada 2009]. So far, however, very little attention to CNCs has been given by the nuclear detection community. In contrast to wide exploitation of quantum confinement effects in optoelectronic and electronic devices, the physics and technology of inorganic scintillators is still primarily limited to bulk materials. Virtually all of the previous studies of nuclear radiation detectors have focused on investigating bulk single crystal materials or pressed ceramics. Yet, compared to currently used large-size single crystals or scintillating particles of bulk micrometer size, nanocrystals (NCs) offer the prospect of significantly improved performance.

Large single-crystal inorganic scintillators have high output efficiency, but are very fragile, expensive to grow, and the size of high-quality crystals is limited. Particulate scintillating semiconductors of micrometer size could bring scalability and robustness to the field of inorganic scintillators. Their use, however, is limited by their low solubility in organic and polymeric matrices, and when prepared in inorganic matrices, such as sol-gel, they produce an optically opaque gel, which significantly reduces scintillation output. One important approach to overcoming these limitations could be using suspensions or composites of nanocrystalline materials. Due to their small size, CNCs are expected to have better solubility in organic and polymeric matrices, and to cause much less scattering when loaded into inorganic sol-gel or porous host materials, which should result in higher efficiency of the scintillator. CNCs of known and novel scintillation materials will allow for production of large robust nanocomposites with a variety of shapes and sizes.

Due to three-dimensional confinement and much better overlap of electron and hole wavefunctions, the band-to-band optical transitions in CNCs are expected to be more efficient and much faster than in bulk scintillators, which should eliminate the major problem of relatively slow response and afterglow of scintillator detectors.

For these reasons, detection of nuclear radiation by its conversion to UV or visible light can be another attractive application of CNCs. The luminescence of lanthanide ions in organic media

has been shown to greatly improve by doping them in the inorganic core of nanoparticles that are soluble in organic solvents [Stouwdam 2003]. This is due to the fact that the long-lived excited state of the lanthanide ions is quenched very effectively by the high-energy vibrations of closely spaced organic groups [Klink 2000]. With scintillating nanoparticles, novel radiation-based cancer treatments may become possible [Chen 2006b].

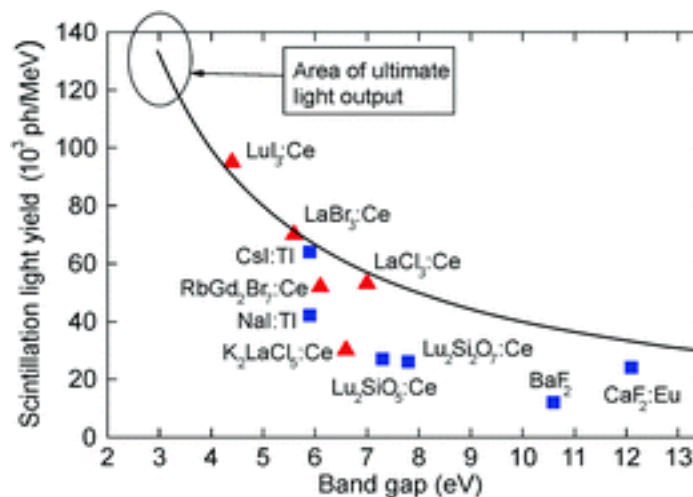


Fig. 3.2. Scintillation light yield in 1000's of photons per MeV for various single-crystal bulk scintillators [Krämer 2006].

Scintillators are the most widely used detectors for  $\gamma$ -ray spectroscopy. Over the last decade, the quest for an ideal scintillator has resulted in a large number of new materials with remarkable properties, including single-crystal lanthanide halides (LaBr₃:Ce, LaCl₃:Ce, CeF₃, CeBr₃, LuI₃), alkali halides (CsI:Na, CsI:Ti), tungstates (PbWO₄ – PWO, CdWO₄ – CWO, ZnWO₄), perovskites (YAlO₃:Ce – YAP:Ce, LuAlO₃:Ce – LuAP:Ce, Lu₁₋ₓYₓAlO₃:Ce – LuYAP:Ce), orthoborates (LuBO₃:Ce, LuBO₃:Pr), oxyorthosilicates (Lu₂SiO₅:Ce – LSO:Ce, Y₂SiO₅:Ce – YSO:Ce, Lu₂(1-x)Y₂xSiO₅:Ce – LYSO:Ce, Gd₂SiO₅:Ce – GSO:Ce), pyrosilicates (Lu₂Si₂O₇:Ce – LPS:Ce), garnets (Y₃Al₂(AlO₄)₃:Ce – YAG:Ce, Y₃Ga₂(GaO₄)₃:Yb – YGG:Yb, Lu₃Al₂(AlO₄)₃:Ce – LuAG:Ce), direct-gap semiconductors (CuI, HgI₂, PbI₂, ZnO:Ga, CdS:In), and optical ceramics (YAG:Nd, LuAG:Ce, Gd₃Ga₂(GaO₄)₃:Ce, Y₂O₃:Nd, (Gd,Y)₂O₃:Eu, Lu₂O₃:Eu, Gd₂O₂S:Ce). Among those, lanthanide halides have produced the highest light outputs (Fig. 3.2) combined with speeds much faster than traditional materials [van Loef 2001b], [Shah 2003], [Dorenbos 2005], [Moses 2005], [Birowosuto 2005]. Compared to the light yield of 38,000 photons per MeV and the decay time of 230 ns for NaI:TI⁺ [Derenzo 1992], which dominated the scintillator market for over 50 years, the corresponding values for LaBr₃ doped with 5% Ce³⁺ are 70,000 and 16 ns, and for LuI₃: Ce³⁺ 95,000 and 24 ns [Krämer 2006]. Also, the stopping power of lanthanide halides compares favorably to NaI. Using the material data from ORNL Radiological Toolbox [Eckerman 2003], we estimate that a 1-cm-thick layer of NaI absorbs 11.5% of incident 662-keV photons, while LaBr₃ absorbs 13.7%, and LuI₃ 16.5%. Table 3.1 shows the Z-numbers of selected elements of interest to nanoscintillator applications, as well as the relative abundances of their naturally occurring isotopes.

Cerium-doped lanthanum halides are a class of scintillators that combine high levels of light output [Krämer 2006], [Bizarri 2007], relatively short scintillation decay time [Moses 1990b], [van Loef 2001a], high energy-resolution [van Loef 2001b], and good linearity of response

[Bizarri 2006]. Their interesting properties also include efficient radiation absorption and highly luminescent activator (cerium) protected by the host material from luminescence quenching.

Table 3.1. Z-numbers and relative abundances of naturally occurring isotopes of selected elements. Radioactive isotopes with relatively short half-lives are marked in red

Element	Atomic Number Z	Stable Isotopes/Natural Abundance	Radioactive Isotopes/Natural Abundance/Half-Life
H	1	$^1\text{H}$ (99.985%), $^2\text{H}$ (0.015%)	–
O	8	$^{16}\text{O}$ (99.76%), $^{18}\text{O}$ (0.20%), $^{17}\text{O}$ (0.04%)	–
F	9	$^{19}\text{F}$ (100%)	–
Na	11	$^{23}\text{Na}$ (100%)	–
S	16	$^{32}\text{S}$ (95.02%), $^{34}\text{S}$ (4.21%), $^{33}\text{S}$ (0.75%), $^{36}\text{S}$ (0.02%)	–
Zn	30	$^{64}\text{Zn}$ (48.6%), $^{66}\text{Zn}$ (27.9%), $^{68}\text{Zn}$ (18.8%), $^{67}\text{Zn}$ (4.1%), $^{70}\text{Zn}$ (0.6%)	–
Se	34	$^{80}\text{Se}$ (49.61%), $^{78}\text{Se}$ (23.78%), $^{76}\text{Se}$ (9.36%), $^{77}\text{Se}$ (7.63%), $^{74}\text{Se}$ (0.87%)	$^{82}\text{Se}$ (8.73%), $1.08 \times 10^{20}$ y
Br	35	$^{79}\text{Br}$ (50.69%), $^{81}\text{Br}$ (49.31%)	–
Cd	48	$^{112}\text{Cd}$ (24.13%), $^{111}\text{Cd}$ (12.80%), $^{110}\text{Cd}$ (12.49%)	$^{114}\text{Cd}$ (28.73%), $>9.3 \times 10^{17}$ y; $^{113}\text{Cd}$ (12.22%), $7.7 \times 10^{15}$ y; $^{116}\text{Cd}$ (7.49%), $2.9 \times 10^{19}$ y; $^{106}\text{Cd}$ (1.25%), $>9.5 \times 10^{17}$ y; $^{108}\text{Cd}$ (0.89%), $>6.7 \times 10^{17}$ y
I	53	$^{127}\text{I}$ (100.00%)	–
La	57	$^{139}\text{La}$ (99.91%)	$^{138}\text{La}$ (0.09%), $1.05 \times 10^{11}$ y
Ce	58	$^{140}\text{Ce}$ (88.45%), $^{142}\text{Ce}$ (11.11%), $^{138}\text{Ce}$ (0.25%), $^{136}\text{Ce}$ (0.19%)	–
Lu	71	$^{175}\text{Lu}$ (97.41%)	$^{176}\text{Lu}$ (2.59%), $3.78 \times 10^{10}$ y
Pb	82	$^{208}\text{Pb}$ (52.4%), $^{206}\text{Pb}$ (24.1%), $^{207}\text{Pb}$ (22.1%), $^{204}\text{Pb}$ (1.4%)	–

In this project, we focus on exploratory investigations of two classes of NCs, cerium-doped lanthanum halide NCs and lead-iodide-based NCs, in order to determine their potential as gamma and neutron radiation detectors.

### **3.A. Potential Advantages of Nanoscale Devices for Nuclear Radiation Detection**

Commonly used inorganic scintillators consist of a transparent insulator and an activator functioning as a luminescence center. They are, in many cases, either slow or have low radiative efficiency. Indeed, in developing ultrafast scintillators, the luminescence via an intermediate

excited state of an impurity is rather disadvantageous. Currently, the conventional  $\text{Ce}^{3+}$ -activated inorganic scintillators provide the best combination of speed and efficiency, but their radiative decay times are limited to  $\sim 10\text{-}60$  ns [Shah 2003], [Weber 2002]. Direct excitonic luminescence from pure semiconductors could be employed by using the direct recombination of an electron and a hole with a decay time constant shorter than 10 ns, and in some cases even on a picosecond time scale. For example, ZnO has radiative lifetimes measured at 50-300 ps for  $\text{D}^0\text{X}$  and 400-900 ps for free excitons [Wilkinson 2004]. However, undoped semiconductors have rarely been used as scintillators, because of their poor luminescence efficiency at RT. The excitonic level in a semiconductor is below the bottom of the conduction band by the binding energy  $E_b$  of the exciton. In most bulk semiconductors, the excitonic level is not deep enough to prevent the thermal dissociation of excitons, and, as a result, the significant thermal quenching of excitonic luminescence at RT. Recently, very fast and efficient performance has been demonstrated from pure semiconducting scintillators such as  $\text{PbI}_2$  and  $\text{HgI}_2$  at cryogenic temperatures [Derenzo 2002], [Klintenberg 2002], [Klintenberg 2003]. Cooling the system to very low temperatures increased the population of excitons, rather than free carriers, by effectively suppressing the thermal perturbations proportional to the thermal energy  $k_B T$ .

Increasing the binding energy  $E_b$  of the exciton to the values exceeding the thermal energy  $k_B T$  at RT ( $\sim 26$  meV) is the requirement to thermally stabilize the excitonic level at RT. This can be realized by employing quantum confinement effect observed in low-dimensional quantum confinement systems (LD QCS). Enhancement of Coulomb interaction between the electron and hole due to spatial confinement is known to deepen the excitonic level in a low-dimensional system. For example, the binding energy of the lowest exciton confined in a two-dimensional (2D) quantum-well system is four times higher than that of the free exciton in the corresponding 3D bulk system [Papavassiliou 1997]. In addition to providing improved thermal stability of the excitonic population, quantum confinement affects the excitonic radiative and nonradiative lifetimes in a way that would further enhance the radiative efficiency. Due to much better overlap between the electron and hole wavefunctions in a LD QCS, the excitonic oscillator strength increases and the excitonic radiative lifetime shortens [Amand 1992], [Xu 1993]. At the same time, the nonradiative lifetime lengthens due to a decrease in the effective density of nonradiative centers that can be encountered by the spatially confined excitons. So far, the validity of this “quantum scintillator” approach has been confirmed for 2D multiple quantum well system based on lead-halide perovskite-type organic-inorganic compounds [Shibuya 2004a], [Shibuya 2004b].

The advantageous effects of quantum confinement are expected to be even more pronounced in NC-based scintillators (complete 3D quantum confinement). The very first experimental indication of this effect was the markedly enhanced X-ray excitation luminescence from thin  $\text{CsI}:\text{Na}$  films, ascribed to the formation of  $\text{NaI}$  nanoparticles caused by heat treatment [Nakayama 2002], [Nakayama 2004], [Nakayama 2005]. More recently, radioluminescence of  $\text{Y}_2\text{SiO}_5:\text{Ce}$  nanophosphors was shown to be twice more intense compared to bulk  $\mu\text{m}$ -size powder made of the same material [McKigney 2007]. The oscillator strength of 0.017 for radiative transitions in  $\text{Y}_2\text{SiO}_5:\text{Ce}$  measured for the nanophosphors compares favorably to the corresponding value of 0.009 for the bulk powder.



### **3.B. Nanocrystalline Films and Pressed Ceramics**

By sintering nanocrystalline powders of known scintillating materials, optically transparent films can be fabricated. While the advantages of 3D quantum confinement are lost, this approach offers low cost and design flexibility, which makes it a very attractive alternative to the growth of large-size single crystals.

(Gd,Y)<sub>2</sub>O<sub>3</sub>:Eu transparent optical ceramics were investigated by Kim *et al.*, who used glycine-nitrate combustion method to produce nanocrystalline powder that subsequently was hot-pressed and annealed [Kim 2004]. 100 keV X-rays were used to measure radioluminescence, which peaked at ~610 nm and was twice as strong as from a CWO single crystal.

Sol-gel combustion process was used to prepare LuAG:Ce nanocrystalline powder with grain size of ~40 nm, which then was sintered under vacuum and annealed in air [Liu 2006]. The compacted disks emitted light at ~550 nm under 50 keV X-ray illumination. The same group has very recently used the sol-gel combustion process with glycine as a fuel to form Eu-doped lutetia (Lu<sub>2</sub>O<sub>3</sub>:Eu) nanopowders that were calcinated and sintered [Liu 2007]. Radioluminescent spectra showed intense emission centered at 612 nm.

Solution-based sol-gel process followed by sintering was used for CWO NCs with a variety of dopants (Li<sup>+</sup>, B<sup>3+</sup>, and Bi<sup>3+</sup>) [Shang 2006]. Addition of dopants was found to enhance densification and to maintain small size (~200 nm) of the grains during sintering. No radiation response of these films has been reported so far.

### **3.C. Prior Work on Nanoscintillators**

The first demonstration of CNCs as scintillators for radiation detection was reported by Dai *et al.* [Dai 2002], who used CdSe/ZnS core/shell colloidal quantum dots (QDs). The QDs were rendered water soluble by exchanging the surface ligands with dithiothreitol (DTT), added during the preparation of lithiated <sup>6</sup>LiOH gels, and embedded in a transparent sol-gel matrix. Using a standard setup with a photomultiplier tube (PMT), amplifier, and a multichannel board, scintillation was observed under  $\alpha$  irradiation from a <sup>210</sup>Po source. Neutron detection, although intended, was not demonstrated in this material system.

Commercial CdSe/ZnS colloidal QDs suspended in toluene were used in [Létant 2006a]. The QDs were inserted in porous glass with pores enlarged to 10-20 nm in diameter in order to increase their concentration. Scintillation from 1/16 in. thick nanocomposite was observed under  $\alpha$  irradiation from 0.2  $\mu$ Ci <sup>243-244</sup>Cm source. Due to a poor match between the QD emission at 540 nm and a PMT used to record scintillation events, only 0.4% of photons emitted by the QDs were amplified, resulting in a poor, barely detectable signal. These results were significantly improved in a subsequent paper by the same authors [Létant 2006b], where a PMT with 15% quantum efficiency at 510 nm produced a clear pulse height spectrum, significantly above the background.

Nanoporous glass impregnated with CdSe/ZnS colloidal QDs emitting at 510 nm was also used to detect radiation from 1  $\mu$ Ci <sup>241</sup>Am source, emitting 59 keV  $\gamma$  rays [Létant 2006b]. Energy

resolution of  $\sim 15\%$  obtained by recording the scintillation output from 1 in. thick nanocomposite over the period of 3 days was twice better than the corresponding energy resolution of  $\sim 30\%$  observed for 1 in.  $\times$  1 in.  $\varnothing$  bulk NaI:Tl crystal.

Quantum dot/organic semiconductor composite based on CdSe/ZnS core-shell QDs was tested under electron-beam excitation using cathodoluminescence [Campbell 2006].

X-ray luminescence of BaFBr NCs doped with Eu or Mn, and of LaF<sub>3</sub>:Ce was studied in [Chen 2006b]. BaFBr:Eu,Mn exhibited persistent luminescence (afterglow) for as long as 8 minutes after the X-ray excitation source was turned off, hence it is not suitable for fast radiation detectors.

Preliminary data on scintillation response of LaF<sub>3</sub>:Ce NCs embedded in an organic matrix and exposed to <sup>241</sup>Am as well as <sup>57</sup>Co (89% 122 keV and 11% 136 keV photons) sources were given in [McKigney 2007]. The energy resolution was stated as “not good”, reportedly due to low quantum efficiency of the LaF<sub>3</sub>:Ce NCs, poor stopping power of unoptimized nanocomposites, and low concentration of NCs in liquid solutions.

#### **4. PROPERTIES OF BULK CERIUM-DOPED LANTHANUM FLUORIDE AND LANTHANUM BROMIDE**

For our initial studies, lanthanum fluoride was chosen in order to simplify the synthesis and application of CNCs, since the high electronegativity of fluorine makes it a robust compound, while other lanthanum halides, such as LaCl<sub>3</sub> and LaBr<sub>3</sub>, are hygroscopic [van Loef 2001a], [van Loef 2001b].

##### **4.A. Physical Properties and Light Emission Mechanism**

Bulk lanthanum fluoride doped with cerium, Ce<sub>x</sub>La<sub>1-x</sub>F<sub>3</sub>, has density between 5.936 g/cm<sup>3</sup> for 0% [Krivandina 2006] and 6.16 g/cm<sup>3</sup> for 100% Ce content [Anderson 1989].

The luminescence of the trivalent lanthanide ions arises either from intraconfigurational  $4f^n \rightarrow 4f^{n-1}$  transitions within the 4f shell (Eu<sup>3+</sup>, Er<sup>3+</sup>), or from interconfigurational  $4f^{n-1}5d^1 \rightarrow 4f^n$  transitions (Ce<sup>3+</sup>, Pr<sup>3+</sup>) between 5d and 4f shells. These excited states can be very efficiently quenched in the presence of high-energy vibrations of organic solvents, polymers, or ligands. Doping of the lanthanide ions into LaX<sub>3</sub> (X = Cl, F, Br, I) materials provides strong shielding of the 4f and 5d electrons from the environment. The 5d electron states, however, turn out to be very sensitive to the local environment of the host material [Dorenbos 2000a-d]. In particular, a profound influence of the halide anions on the energy of the 5d levels of Ce<sup>3+</sup> in LaX<sub>3</sub> (X = Cl, Br, I) has been reported [van Loef 2003]. As a result, emission from the lowest-energy state deriving from the 5d<sup>1</sup> electron configuration in Ce<sup>3+</sup> is observed as a broad peak, with central wavelength ranging from 259 nm in RbCaCl<sub>3</sub>:Ce<sup>3+</sup> to 700 nm in LaLuS<sub>3</sub>:Ce<sup>3+</sup> and MgSc<sub>2</sub>S<sub>4</sub>:Ce<sup>3+</sup> [Dorenbos 2000b].

The free-ion ground configuration of Ce<sup>3+</sup> consists of a xenon-like core with 54 electrons and a valence shell containing one 4f electron. This 4f configuration is further split by spin-orbit interaction into <sup>2</sup>F<sub>7/2</sub> and <sup>2</sup>F<sub>5/2</sub> levels. The first excited 5d configuration is also split into <sup>2</sup>D<sub>3/2</sub> and

$^2D_{5/2}$  energy levels due to spin-orbit interactions. In a crystalline environment, the energy level configuration changes considerably. For example, in  $\text{LaF}_3$  crystalline environment the crystal field interaction dominates over the spin-orbit interaction, depressing the average energy of the 5d configuration by the centroid shift  $\epsilon_c$  and splitting the 5d configuration into five distinct levels, with the lowest and highest 5d levels separated by the crystal field splitting  $\epsilon_{cf}$  (Fig. 4.1) [Dorenbos 2000c].

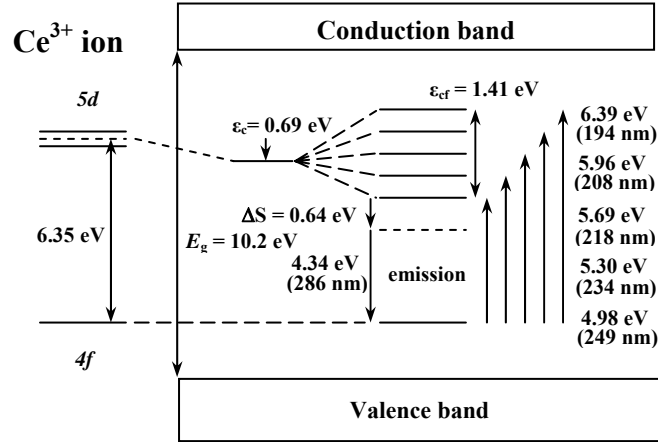


Fig. 4.1. Energy level configuration of  $\text{Ce}^{3+}$  ion doped into  $\text{LaF}_3$  host lattice (based on data from [Dorenbos 2000c]).

Table 4.1. Summary of scintillation properties of  $\text{Ce}_x\text{La}_{1-x}\text{F}_3$  [Moses 1990]

Cerium fraction, $x$	Emission peak	3.0 ns decay component	26.5 ns decay component	“Long” decay component
1%	290 nm	15%	64%	21% @ 273 ns
10%	300 nm	10%	86%	4% @ 185 ns
50%	300 nm	10%	87%	3% @ 185 ns

Table 4.2. Summary of scintillation properties of bulk  $\text{LaBr}_3:\text{Ce}$  [Glodo 2005]

Cerium fraction	Emission peak	$\tau_1$	$\tau_2$	$\tau_3$
0.5%	355 nm	19 ns @ 56%	15.2 ns @ 28%	55 ns @ 16%
10%	360 nm	16.5 ns @ 89%	4.5 ns @ 5%	55 ns @ 6%
30%	365 nm	18 ns @ 91%	2.5 ns @ 4%	55 ns @ 6%

Both in bulk  $\text{LaF}_3:\text{Ce}^{3+}$  [Moses 1990b] and  $\text{LaBr}_3:\text{Ce}^{3+}$  [Glodo 2005], the emission was found to be dependent on Ce concentration, presumably through the Stokes shift  $\Delta S$  sensitive to the lattice phonons. Scintillation response in Ce-doped lanthanum halide compounds [Bizarri 2007] is governed by the intrinsic lifetime of the emitting 5d state of Ce, with prompt (faster than 1 ns) capture of free charge carriers from the ionization track by Ce leading to 4f-5d excitation and followed by fast 5d-4f emission. The emission peak position and scintillation decay times in bulk  $\text{Ce}_x\text{La}_{1-x}\text{F}_3$  at various Ce contents, taken from [Moses 1990b], are shown in Table 4.1. The

emission peak position and scintillation decay times in bulk  $\text{Ce}_x\text{La}_{1-x}\text{Br}_3$  at various Ce contents, taken from [Glodo 2005], are presented in Table 4.2.

#### **4.B. Radiation Absorption Parameters**

One of important figures of merit for a scintillator is how efficiently the material absorbs gamma radiation. Neglecting non-absorptive scattering effects, a material or element can be characterized with the **mass energy-transfer coefficient**,  $\mu_{\text{tr}}/\rho$ , expressed in units of  $\text{cm}^2/\text{g}$ . This parameter is related to the portion of attenuated energy that is originally absorbed by the material as kinetic energy by electrons or re-emitted immediately as characteristic X-rays.

The mass energy-transfer coefficient for a compound material of density  $\rho$  can be calculated from the elemental data of its constituents [Attix 1986]:

$$\left(\frac{\mu_{\text{tr}}}{\rho}\right)_{\text{mix}} = \left(\frac{\mu_{\text{tr}}}{\rho}\right)_A f_A + \left(\frac{\mu_{\text{tr}}}{\rho}\right)_B f_B + \dots, \quad (4.1)$$

where  $f_A, f_B, \dots$  are the mass fractions of the elements given by

$$f_X = \frac{N_{\text{Atoms of X/Molecule}} W_{\text{Atomic Weight of X}}}{M_{\text{Atomic Weight of Molecule}}}. \quad (4.2)$$

The **mass energy-absorption coefficient**,  $\mu_{\text{en}}/\rho$  with units of  $[\text{cm}^2/\text{g}]$ , describes the amount of energy retained by the material. It is smaller than the mass energy-transfer coefficient due to energy loss from Brehmsstrahlung radiation from ionized electrons. For single-element materials,  $\mu_{\text{en}}/\rho$  is related to  $\mu_{\text{tr}}/\rho$  by the parameter  $g$ , where

$$\mu_{\text{en}}/\rho = (1 - g)\mu_{\text{tr}}/\rho. \quad (4.3)$$

For compound materials,  $\mu_{\text{en}}/\rho$  can be calculated from the stoichiometric formula and the elemental data for the mass energy-transfer coefficient  $\mu_{\text{tr}}/\rho$ , using the formula [Attix 1986]:

$$\left(\frac{\mu_{\text{en}}}{\rho}\right)_{\text{mix}} = \left(\frac{\mu_{\text{tr}}}{\rho}\right)_A (1 - fg_{\text{mix}})f_A + \left(\frac{\mu_{\text{tr}}}{\rho}\right)_B (1 - fg_{\text{mix}})f_B + \dots, \quad (4.4)$$

where

$$fg_{\text{mix}} = f_A g_A + f_B g_B + \dots, \quad (4.5)$$

and the average fraction  $g_x$  of secondary-electron energy that is lost in radiative interactions in material  $x$  is

$$g_x = 1 - \left( \frac{\mu_{\text{en}}/\rho}{\mu_{\text{tr}}/\rho} \right)_x. \quad (4.6)$$

From these formulae and physical parameters for lanthanum, fluorine, and cerium, retrieved from public access NIST database [Hubbel 2004], we have calculated the mass-energy absorption coefficient for  $\text{LaF}_3$ ,  $\text{CeF}_3$ , and  $\text{LaF}_3$  doped with 5% and 10% cerium. As shown in Fig. 4.2(a), in the gamma photon energy range from 1 keV to 20 MeV, the curves of mass-energy absorption coefficient are almost indistinguishable, except in close vicinity of the L and K edges of the lanthanides. Fig. 4.2(b) shows the L edges in more detail.

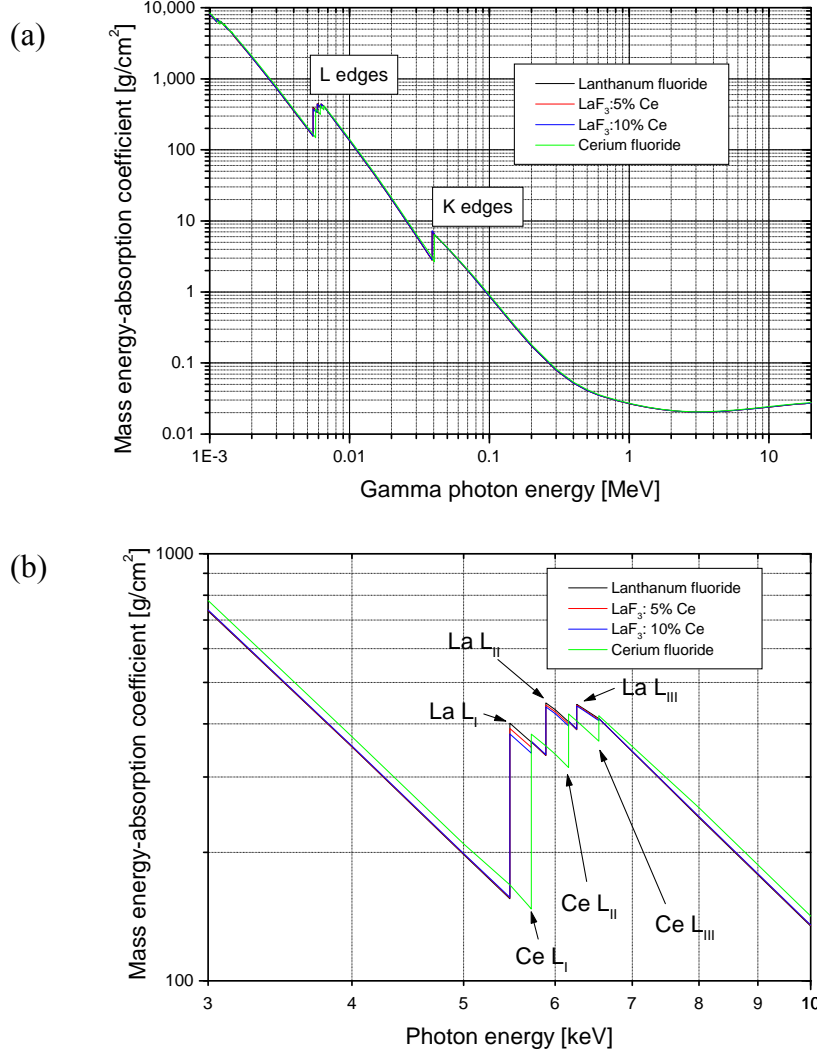


Fig. 4.2. (a) Mass energy-absorption coefficient graph for lanthanum fluoride, cerium fluoride, lanthanum fluoride with 5% cerium doping, and lanthanum fluoride with 10% cerium doping. (b) Portion of Fig. 4.1(a) near the L-edges of the lanthanides.

To calculate the amount of energy absorbed or scattered by a sheet of material of thickness  $d$ , the formula

$$I = I_0 \exp[-(\mu/\rho)\rho d] \quad (4.7)$$

is used, where the original gamma ray flux is  $I_0$ ,  $\mu$  is the linear attenuation coefficient, and  $\rho$  is the density of the material.

Table 4.3 shows the calculated half-value layer (HVL) thickness, equal to  $\ln(2)/\mu$ , for some of the materials of interest to nanocrystalline scintillator research.

The values of mass attenuation coefficient  $\mu/\rho$  in Table 4.3 have been calculated using elemental data from public access NIST database [Hubbel 2004] and the Bragg rule for mixing elements [Attix 1986]:

$$\left(\frac{\mu}{\rho}\right)_{\text{mix}} = \sum_{i=1}^n \left(\frac{\mu}{\rho}\right)_i f_i, \quad (4.8)$$

where  $(\mu/\rho)_{\text{mix}}$  is the mass attenuation coefficient for the mixture,  $(\mu/\rho)_i$  is the mass attenuation coefficient for the element  $i$ ,  $f_i$  is the weight fraction of the element  $i$ , and  $n$  is the number of elements in the mixture.

Table 4.3. Mass attenuation coefficient  $\mu/\rho$  and half value layer thickness (HVL) at 662 keV for selected materials

Material	Density [g/cm <sup>3</sup> ]	$\mu/\rho$ [cm <sup>2</sup> /g]	HVL [cm]
NaI	3.67 <sup>(a)</sup>	$7.77 \times 10^{-2}$	2.43
ZnS	4.09 <sup>(b)</sup>	$7.52 \times 10^{-2}$	2.25
LaBr <sub>3</sub>	5.06 <sup>(c)</sup>	$7.5 \times 10^{-2}$	1.83
CeBr <sub>3</sub>	5.18 <sup>(c)</sup>	$7.56 \times 10^{-2}$	1.77
CdSe	5.81 <sup>(d)</sup>	$7.38 \times 10^{-2}$	1.62
LaF <sub>3</sub>	5.94 <sup>(e)</sup>	$7.83 \times 10^{-2}$	1.49
LuI <sub>3</sub>	5.69 <sup>(f)</sup>	$8.40 \times 10^{-2}$	1.45
CeF <sub>3</sub>	6.16 <sup>(g)</sup>	$7.96 \times 10^{-2}$	1.41
PbI <sub>2</sub>	6.16 <sup>(h)</sup>	$9.42 \times 10^{-2}$	1.19
PbIOH	6.85 <sup>(i)</sup>	$9.93 \times 10^{-2}$	1.02
Pb <sub>3</sub> I <sub>2</sub> O <sub>2</sub>	7.57 <sup>(j)</sup>	$10.25 \times 10^{-2}$	0.89

<sup>(a)</sup>[Lecoq 2000]; <sup>(b)</sup>[Okuyama 1997]; <sup>(c)</sup>[Higgins 2008]; <sup>(d)</sup>[Broser 1982]; <sup>(e)</sup>[Klein 1967], [Krivandina 2006]; <sup>(f)</sup>[Krämer 2006]; <sup>(g)</sup>[Anderson 1989]; <sup>(h)</sup>[Klintenberg 2003]; <sup>(i)</sup>[Dennis 1965]; <sup>(j)</sup>[Kramer 1985].

## **5. COLLOIDAL SYNTHESIS OF LANTHANIDE HALIDE SCINTILLATING NANOCRYSTALS (TASK 1)**

This section reports main accomplishments and new findings obtained under Task 1, devoted to colloidal synthesis of lanthanide halide scintillating NCs.

With the reported light yield of  $\sim 2,000$  photons/MeV and the dominant scintillation decay component as short as 26.5 ns [Moses 1990b], bulk LaF<sub>3</sub>:Ce scintillators do not possess the best

combination of efficiency and speed among a variety of Ce-doped lanthanum halide crystals that show good scintillation detection properties. For example, Ce-doped bulk  $\text{LaBr}_3$  was reported to have a light yield of 60,000 photons/MeV, 2.5% full-width-to-half-maximum energy resolution for 662 keV  $\gamma$  rays, and 25 ns short decay time [Derenzo 2005]. However, while having those attractive properties,  $\text{LaBr}_3\text{:Ce}$  bulk crystals are expensive and difficult to manufacture and use. The crystals are highly hygroscopic and very fragile, and hence have to be protected from external environment both during growth and use.

## **5.A. Colloidal Synthesis of $\text{LaF}_3\text{:Eu}$ , $\text{LaF}_3\text{:Ce}$ , and $\text{LaF}_3\text{:Ce/LaF}_3$ Scintillating Nanocrystals**

### **5.A.a. Synthesis in Aqueous Solutions**

For aqueous synthesis of  $\text{Ce}_x\text{La}_{1-x}\text{F}_3$  CNCs [Sankar 2009], we have used a modified procedure of [Wang 2006], originally developed to produce chitosan-coated Eu-doped  $\text{LaF}_3$  CNCs. Fig. 5.1 illustrates schematically the setup used in colloidal synthesis.

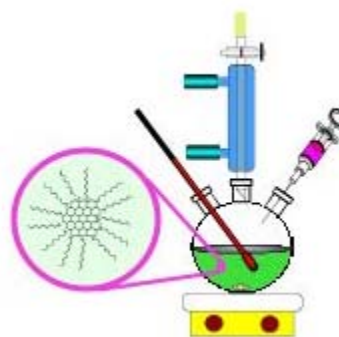


Fig. 5.1. Setup for CNC synthesis: three-neck round-bottom flask, cooling column, nitrogen adaptor, thermometer, and syringe.

#### **5.A.a.i. Preparation of stock solutions**

Chitosan (medium molecular weight) was purchased from Fluka. Lanthanum (III) chloride heptahydrate ( $\text{LaCl}_3 \cdot 7\text{H}_2\text{O}$ , 99.9%), europium (III) chloride heptahydrate ( $\text{EuCl}_3 \cdot 7\text{H}_2\text{O}$ , 99.999%), cerium (III) chloride heptahydrate ( $\text{CeCl}_3 \cdot 7\text{H}_2\text{O}$ , 99.999%), ammonium fluoride ( $\text{NH}_4\text{F}$ , 98+%), and 37% (12.1M) hydrochloric acid were all purchased from Sigma-Aldrich. De-ionized (low conductivity) water was obtained from the DI water plant at CHTM/UNM.

Three stock solutions were used as reagents and prepared before the synthesis. 0.2 M  $\text{LaCl}_3$  stock solution was prepared by dissolving 17.668 g of lanthanum (III) chloride heptahydrate in 250 ml of DI water. 0.2 M  $\text{EuCl}_3$  stock solution was prepared by dissolving europium (III) chloride heptahydrate in DI water. Similarly, 0.2 M  $\text{CeCl}_3$  stock solution was prepared by dissolving 3.758 g of cerium (III) chloride heptahydrate in 50 ml of DI water. 1 g of highly viscous chitosan was dissolved in a mixture of 0.428 g of 37% HCl solution and 100 ml of deionized (DI) water adjusted to pH of 1.3 (0.05 M) to obtain 1 wt% chitosan stock solution. All stock solutions were stirred using a stirrer and a stir bar to facilitate complete dissolution of the solute in the solvent.

### **5.A.a.ii. Synthesis procedure**

A 500-ml three-neck flask used for the synthesis was kept under argon atmosphere in a Schlenk line setup. The flask was placed on a heating and stirring mantle controlled by a programmable ramping temperature controller through a type-J thermocouple and a stirring controller (Fig. 5.2).

The calculated quantities of the  $\text{LaCl}_3$ ,  $\text{EuCl}_3$  (or  $\text{CeCl}_3$ ), and chitosan stock solutions were added to the flask and stirred using a stir bar. For example, for the synthesis of  $\text{LaF}_3$  doped with 5% Ce, 9.5 ml of 0.2 M  $\text{LaCl}_3$  solution and 0.5 ml of 0.2 M  $\text{CeCl}_3$  solution were added to 25 ml of chitosan solution and mixed thoroughly using a stir bar. Then, 0.2222 g of ammonium fluoride ( $\text{NH}_4\text{F}$ ) was mixed with 10 ml of DI water to prepare 2.17 wt% ammonium fluoride solution, and was transferred to the flask. The pH of the solution in the flask was adjusted to 6.5 using 0.5 M diluted ammonia solution. Subsequently, the flask was purged with argon and closed. The temperature controller was programmed to ramp the temperature of the solution in the flask uniformly to 75 °C and maintain the temperature for 2 hours, with constant stirring under argon atmosphere. After 2 hours, the solution was cooled to room temperature and washed with equal amounts of DI water and 0.5% acetic acid solution by centrifuging at 4000 rpm. Finally, after discarding the supernatant, the precipitate was collected, dissolved in DI water and stored in a vial. Following the above procedure, samples of chitosan-capped  $\text{LaF}_3$ :  $\text{Eu}^{3+}$  and chitosan-capped  $\text{LaF}_3$ :  $\text{Ce}^{3+}$  water-soluble CNCs were obtained.

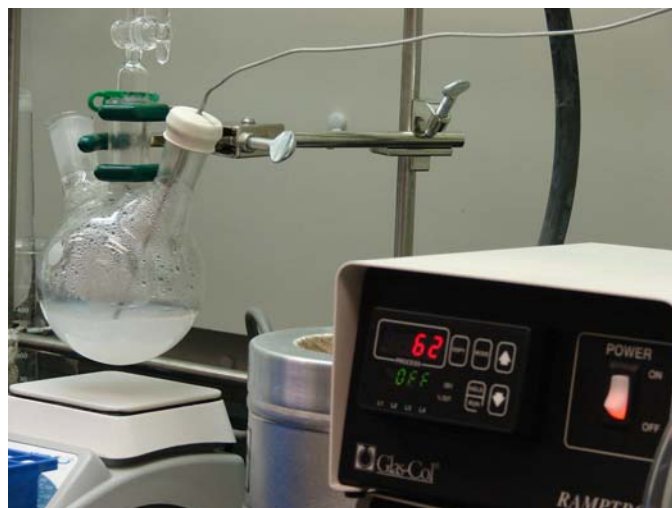


Fig. 5.2. Synthesis of chitosan/ $\text{LaF}_3$ : $\text{Ce}^{3+}$  NCs: The solution undergoes cooling down to room temperature after the synthesis period.

The appearance and pH of the solution were monitored during the addition of the stock solutions to the flask prior to heating. After the addition of  $\text{LaCl}_3$ ,  $\text{EuCl}_3$ , and chitosan stock solutions, the solution appeared to be clear and the pH was at 2.06. Just after the ammonium fluoride stock solution was added to the flask, the solution started turning milky and an instantaneous pH rise to 2.98 was observed. Then, the pH gradually reduced back and stabilized at 2.19. This observation provided evidence of initiation of the co-precipitation process and thereby the release of ammonium ions that temporarily increased the pH, turning the solution milky (Fig. 5.2) and on further reaction forming the  $\text{LaF}_3$  NC nuclei, which resulted in a gradual decrease in the pH



level. Further pH monitoring was not possible, since the solution was heated under argon atmosphere in a closed flask.

The concentration of cerium in the stock solution and the concentration of cerium incorporated in the NCs (assuming that no cerium was lost while washing the NCs) were calculated and their ratio determined to be 10:1.

In order to optimize the procedure, different syntheses were carried out by changing certain parameters one at a time, such as synthesis temperature, quantity of stock solutions, and adjusted pH value.

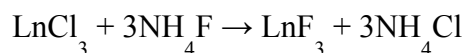
### **5.B. Colloidal Synthesis of $\text{Ce}_x\text{La}_{1-x}\text{F}_3$ Nanocrystals**

In order to determine an optimal Ce concentration for maximum PL emission,  $\text{Ce}_x\text{La}_{1-x}\text{F}_3$  samples with Ce compositions ranging from 0.5% to 100% were prepared using the aqueous method.

$\text{Ce}_x\text{La}_{1-x}\text{F}_3$  CNCs with various Ce content were synthesized at 75 °C in a mixture of HCl, ammonia, and water as described in Section 5.A.a by varying the amount of  $\text{CeCl}_3$  solution used in the synthesis. While maintaining all other synthesis parameters unchanged, eight different syntheses were performed with the intended Ce content ( $x$ ) of 0.5%, 5%, 10%, 15%, 20%, 25%, 75%, and 100% with respect to the total lanthanide (cerium and lanthanum) content.

### **5.C. Aqueous Synthesis of Ln-Doped $\text{LaF}_3$ Colloidal Nanocrystals Capped with Polyethylene Glycol**

With a slight modification to our earlier protocol [Sankar 2009], consisting in replacement of chitosan with polyethylene glycol (PEG), PEG-capped  $\text{LnF}_3$  NCs were synthesized using a co-precipitation reaction in water:



Ln represents any lanthanide, such as for example La, Ce, Eu, or Gd. The NCs were synthesized in the presence of 0.25 g of 10 kDa molecular weight PEG in order for the  $\text{LnF}_3$  NCs to possess good colloidal stability in aqueous solvent. The precursors used were 10 mL of 0.2M  $\text{LnCl}_3$  aqueous solution and 0.111 g of  $\text{NH}_4\text{F}$  in 10 mL of  $\text{H}_2\text{O}$ . The precursors were allowed to react at 75 °C for 2 h, before being centrifuged at 20,000 rpm for 30 min and dispersed in water.

## **6. COLLOIDAL SYNTHESIS OF LEAD-IODIDE-BASED SCINTILLATING NANOCRYSTALS (TASK 2)**

This section reports main accomplishments and new findings obtained under Task 2, devoted to colloidal synthesis of lead-iodide-based scintillating NCs.

Lead-based compound NCs are of interest as potential novel scintillation materials due to their high density and the high atomic weight of Pb. In addition, all naturally occurring isotopes of lead are non-radioactive, thus there is no intrinsic radiation background associated with the use

of lead in a scintillator. However, known lead-based bulk scintillators show poor light output: 50 photons/MeV light output was reported for  $\text{PbWO}_4$  [Brown 2008], 760 photons/MeV for  $\text{PbCO}_3$  [Moses 1990a], and 4,900 photons/MeV for  $\text{PbSO}_4$  [Moses 1992]. Bulk  $\text{PbI}_2$  material produces 3300 photons/MeV at 11 K, with no emission at all above 40 K [Derenzo 2002]. While the bulk materials may have poor efficiency of light emission at room temperature, the effects of quantum confinement are expected to greatly enhance the probability of radiative transitions, as well as reduce the radiative recombination lifetime. Hence, NCs offer a possibility of utilizing the materials that may not even emit light at room temperature in their bulk form.

### **6.A Colloidal Synthesis of $\text{PbI}_2$ Scintillating Nanocrystals**

The procedure for synthesizing nominally  $\text{PbI}_2$  NCs has been adopted from Finlayson and Sazio [Finlayson 2006]. It involved dissolution of bulk (micrometer size) lead iodide powder in a coordinating solvent tetrahydrofuran (THF), subsequent re-crystallization with the addition of a non-coordinating solvent (anhydrous methanol), and addition of a capping agent dodecylamine (DDA) to obtain solvent-stabilized  $\text{PbI}_2$  NCs. Lead (II) iodide (99.999%), THF, anhydrous methanol, and DDA were purchased from Sigma Aldrich and used directly.

In a typical procedure, 100 mg of high purity (99.999%) lead (II) iodide powder was initially dissolved in 15 ml of THF under continuous stirring at room temperature and under atmospheric pressure. The above conditions are important, since solubility is a strong function of temperature and pressure. Subsequently, the solution was sonicated in centrifuge tubes in order to obtain a saturated solution. Then, to remove any insoluble suspension still present, the saturated solution was centrifuged and the clear deep yellow supernatant was decanted out into a flask. Finally, while stirring this solution continuously under nitrogen atmosphere, 10 ml of anhydrous methanol was gradually added to the flask.

A change in color from deep yellow to a colorless solution was noticed upon addition of methanol. Since  $\text{PbI}_2$  is only slightly soluble in methanol, this change was interpreted as indication of the formation of nascent nanoparticles due to re-precipitation in the solution. For this reason, the volumetric ratio of THF to methanol was very important in determining the growth kinetics and nature of the resulting nanoparticles. The re-precipitation process was allowed to continue for 24 hours under constant stirring in nitrogen atmosphere. After that, the process was quenched by addition of DDA at a ratio of 1 mg per 1 ml of the resulting nanoparticulate colloidal solution and the solution was stored in a vial at room temperature. Aliquots were taken at predetermined time intervals to study the time evolution of the synthesis process.

It should be noted that although DDA was added with the intention to stop growth by capping the crystals, as recommended in [Finlayson 2006], we found this quenching procedure to be inefficient, as synthesized NCs left in THF/methanol/DDA solvent kept growing over time, reaching a micrometer size in about 50-day period.

## **6.B Colloidal Synthesis of PbIOH Nanocrystals**

In an effort to identify the highly luminescent crystals described in Sections 8.A,B, we have synthesized PbIOH (also known as iodolaurionite) NCs as a candidate material that has the relative compositional fractions of Pb, I, and O consistent with Fig. 8.4(d) (note that hydrogen does not show up in the EDS analysis).

Bulk crystals of lead hydroxide iodide have been previously synthesized by gel growth methods described in [Dennis 1965] and [Schwartz 1973]. Stable bluish-white cathodoluminescence from PbIOH crystals at room temperature was reported in [Dennis 1965]. No PL was observed at room temperature, whereas at liquid-nitrogen temperature a broad-band PL spectrum was observed, with a 560 nm peak [Schwartz 1973]. Above 200 K, the luminescence was reported to be thermally quenched with an activation energy of 0.3 eV.

Our procedure for synthesis of PbIOH NCs was developed by modifying of a rapid mechanochemical solution method for PbClOH synthesis, reported in [Zhang 2005]. Lead (II) iodide (99.999%) and sodium hydroxide (99.998%) were purchased from Sigma Aldrich, while DI water was obtained from CHTM DI Water Plant. All chemicals were used as received, without further purification. First, a 0.1 M solution of NaOH or KOH was prepared. In method A, 461 mg (~1 mmol) of PbI<sub>2</sub> powder was ground with 3 ml of 0.1 M hydroxide solution in a mortar with a pestle for 2 minutes. In method B, 240 mg of PbI<sub>2</sub> powder was ground with 5 mL of the hydroxide solution in a mortar with a pestle for 2 minutes. The solution from either method was then alternately centrifuged at 4000 rpm 3 times for 5 minutes with DI water and ethanol. The PbIOH NCs were then collected, suspended in ethanol, and stored in a scintillation vial.

## **6.C. Colloidal Synthesis of Water-Soluble Pb<sub>3</sub>O<sub>2</sub>I<sub>2</sub> Scintillating Nanocrystals**

Since the optical properties of PbIOH NCs have not supported the hypothesis that PbI<sub>2</sub>-based NCs evolved into PbIOH (see Section 8.C), we have explored another option, namely iodomendipite (Pb<sub>3</sub>O<sub>2</sub>I<sub>2</sub>).

The synthesis procedure for Pb<sub>3</sub>O<sub>2</sub>I<sub>2</sub> NCs was created by modifying the Pb<sub>3</sub>O<sub>2</sub>Cl<sub>2</sub> NC synthesis reported in [Lozano 2006]. The method is based on thermolysis of a lead iodide octanoate complex in the absence of solvent. Lead (II) iodide (99.999%), sodium octanoate [NaOOC(CH<sub>2</sub>)<sub>6</sub>CH<sub>3</sub>, 99%], and ethylenediamine (C<sub>2</sub>H<sub>8</sub>N<sub>2</sub>, >99%) were purchased from Sigma Aldrich and used as such. DI water was obtained from CHTM DI Water Plant. First, the precursor was prepared by adding 0.332 g of high purity (99.999%) PbI<sub>2</sub> powder to 32 ml of distilled water. The precursor was stirred at high speed for several minutes and then sonicated for 15 minutes. A solution of 0.17 g of sodium octanoate (NaOOC(CH<sub>2</sub>)<sub>6</sub>CH<sub>3</sub>) and 25 mL of chloroform (CHCl<sub>3</sub>) was added to the precursor and mixed vigorously. A two-phase solution was obtained and separated using a separatory funnel. The organic phase on the bottom was put into a flask and the aqueous phase was discarded. 0.5 mL of ethylenediamine was added to the organic phase and the solution was evaporated using a rotary evaporator. A white powder was formed at the bottom of the flask after evaporation and the flask was heated to 170 °C for 60 minutes in air.

After heating, a yellow powder was collected from the flask using chloroform and stored in a scintillation vial.

#### **6.D. Colloidal Synthesis of $\text{Pb}_3\text{O}_2\text{I}_2$ Scintillating Nanocrystals in Trioctylphosphine Oxide**

As a modification of [Lozano 2006], in which trioctylphosphine oxide (TOPO) solvent was used,  $\text{Pb}_3\text{O}_2\text{I}_2$  CNCs were synthesized in TOPO using hexadecylamine surfactant as a stabilizing agent. The  $\text{PbI}_2$  precursor was oxidized at 210 °C for 60 minutes under an air atmosphere and the resulting NCs were washed in methanol before being stored in chloroform.

### **7. CHARACTERIZATION OF LANTHANIDE HALIDE SCINTILLATING NANOCRYSTALS (TASK 3, PART 1)**

This section reports main accomplishments and new findings obtained under part of Task 3 devoted to structural and optical characterization of lanthanide halide scintillating NCs.

#### **7.A. Structural Characterization of Lanthanide Halide Nanocrystals**

For structural characterization, TEM samples were prepared by placing a drop of the colloidal solution in a 200-mesh carbon coated copper grid and the solvent was allowed to dry, fixing the NCs on the grid. High-resolution transmission electron microscope, JEOL-2010F operating at 200 kV was used with the OXFORD Link ISIS energy-dispersive spectroscopy (EDS) apparatus. To get the EDS data, the electron beam was focused on a single NC and the peaks were identified using the Oxford Instruments ISIS software. Data obtained from multiple single-NC measurements showed good repeatability.

The TEM analysis is known to somewhat underestimate the size of the measured crystalline objects by not properly detecting their outermost surface atomic layers. Dynamic light scattering (DLS) analysis, on the other hand, provides information about hydrodynamic size of particles, which accounts for any ligand molecules modifying the surface of nanoparticles (hydrophilic hydroxyl groups for the NCs synthesized using anhydrous approach). DLS measurements were taken with a DynaPro Titan dynamic light scattering module from Wyatt Technology Corporation.

##### **7.A.a. Structural Characterization of $\text{LaF}_3\text{:Eu}$ and $\text{LaF}_3\text{:Ce}$ Nanocrystals Synthesized in Aqueous Solution**

Fig. 7.1 shows a typical high-resolution TEM image of  $\text{LaF}_3\text{:5%Ce}$  NCs. EDS measurements shown in Fig. 7.2 confirm that Ce was indeed incorporated inside the  $\text{LaF}_3$  NCs. Figs. 7.3 and 7.4 compare the size distribution of  $\text{LaF}_3$  NCs doped with 5% and 10% Ce, respectively. The size and shape of the NCs was basically similar in both cases, with hexagonal platelets about 8-20 nm wide and 15-30 nm high.

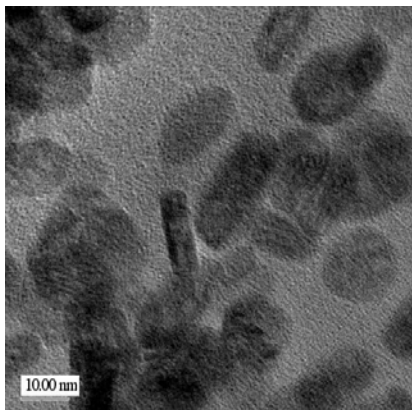


Fig. 7.1. High-resolution bright-field TEM image of  $\text{LaF}_3:5\%\text{Ce}$  NCs synthesized at 75 °C in a mixture of HCl, ammonia, and water.

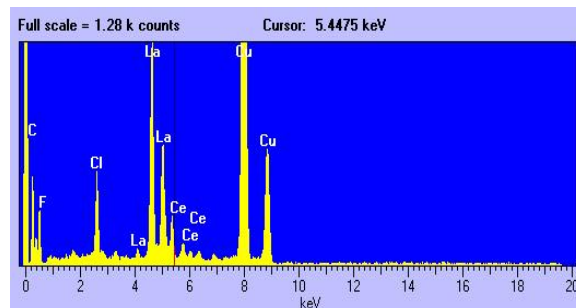


Fig. 7.2. Energy-dispersive spectroscopy (EDS) analysis of the  $\text{LaF}_3:5\%\text{Ce}$  NCs shown in Fig. 7.1. Note clear peaks of La, F, and Ce. The Cu and C peaks originate from the holding grid.

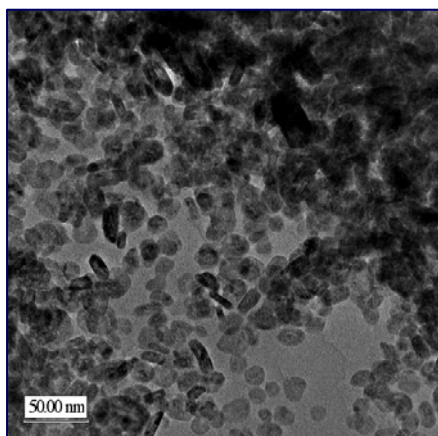


Fig. 7.3. Bright-field TEM image of  $\text{LaF}_3:5\%\text{Ce}^{3+}$  NCs synthesized at 75 °C in a mixture of HCl, ammonia, and water. Hexagonal platelets are 10-20 nm wide and 15-30 nm high.

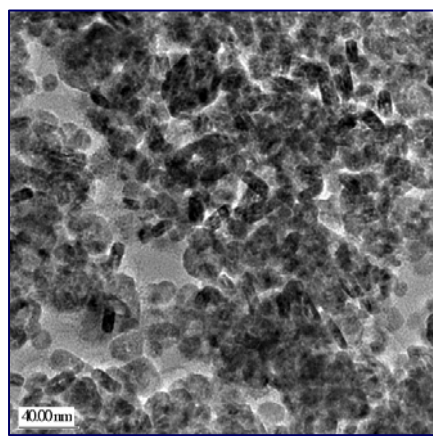


Fig. 7.4. Bright-field TEM image of  $\text{LaF}_3:10\%\text{Ce}^{3+}$  NCs synthesized at 75 °C in a mixture of HCl, ammonia, and water. Hexagonal platelets are 8-10 nm wide and 20-30 nm high.

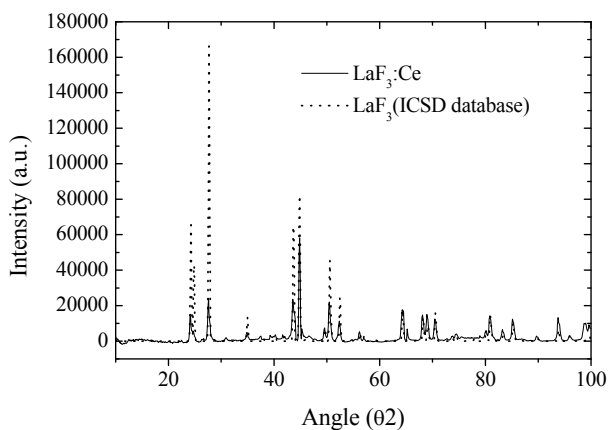


Fig. 7.5. Powder X-ray diffraction spectrum of  $\text{LaF}_3:5\%\text{Ce}^{3+}$  NCs.

Fig. 7.5 shows an X-ray diffraction spectrum of calcinated  $\text{LaF}_3\text{:}5\%\text{Ce}$  NC powder, taken using PANalytical X'Pert PRO multi-purpose diffractometer. A very good agreement can be seen between the measured spectrum and the  $\text{LaF}_3$  spectrum from the ICSD database.

## **7.B. Optical Characterization of Lanthanide Halide Nanocrystals**

The synthesized NCs were characterized using the absorption, photoluminescence (PL) emission, and excitation spectroscopy. Absorption spectra measurements were performed on a Cary 400 UV-VIS spectrophotometer. The PL spectra and excitation spectroscopy measurements were performed using a Horiba Jobin Yvon Fluorolog-3 spectrofluorometer, at 250 nm excitation wavelength (unless stated otherwise). The excitation wavelength of 250 nm was the shortest available with the Xe lamp source.

The fluorescence lifetime measurements were taken on the same Horiba Jobin Yvon Fluorolog-3 spectrofluorometer in time-correlated single photon counting mode. The excitation source was a 250 nm ultraviolet LED, operated at 1 MHz pulse repetition rate.

### **7.B.a. Optical Characterization of $\text{LaF}_3\text{:Eu}$ and $\text{LaF}_3\text{:Ce}$ Nanocrystals Synthesized in Aqueous Solution**

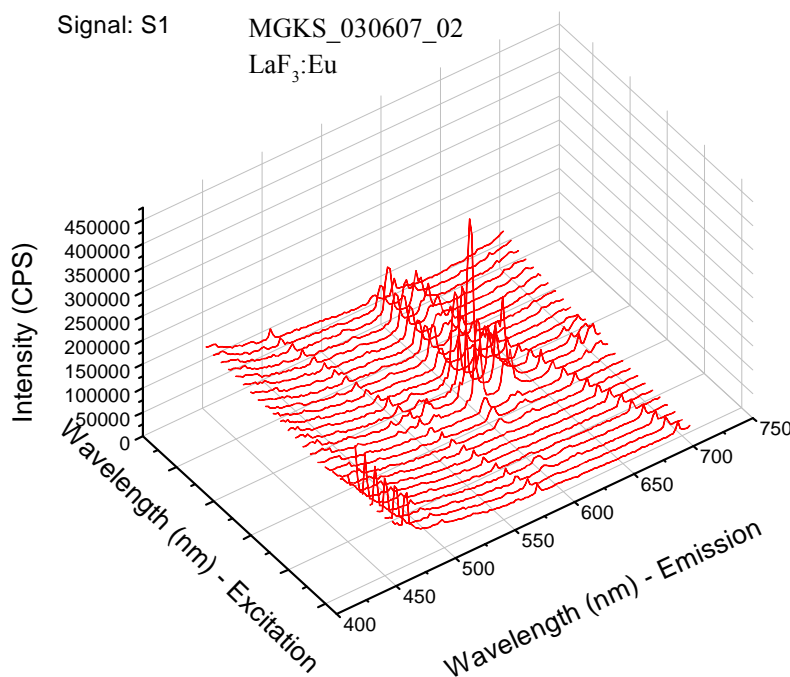


Fig. 7.6. Emission-excitation spectrum of  $\text{LaF}_3\text{:Eu}^{3+}$  NCs.

PL measurements were performed on the europium chloride and cerium chloride stock solutions as well as on the CNCs doped with the respective rare earths to compare the emission intensity levels. The PL spectra and excitation spectroscopy measurements were performed using a Horiba

Jobin Yvon Fluorolog-3 spectrofluorometer, with the excitation and emission monochromators both set at 1 nm.

The Eu-doped  $\text{LaF}_3$  CNCs have been extensively characterized optically, with a series of photoexcitation spectroscopy experiments aimed at establishing the optimal excitation wavelength, at which the observed RT emission reached its maximum intensity. In order to determine the optimal excitation wavelength for  $\text{LaF}_3:\text{Eu}^{3+}$  CNCs, we measured first a PL emission spectrum of CNCs in the 420 nm – 750 nm range using a tentative wavelength of 380 nm for excitation. The intensity of the strongest peak at 591 nm in the emission spectrum was then registered during the PL excitation scan from 320 nm to 500 nm. The resulting excitation spectrum, corrected for spectral nonuniformity of the lamp, showed the main maximum at 396 nm, thus identified as the optimal wavelength for excitation of  $\text{LaF}_3:\text{Eu}^{3+}$  CNCs. An example of a full excitation spectra scan is shown in Fig. 7.6. Fig. 7.7 shows the corresponding spectra observed at the emission wavelength of 590 nm.

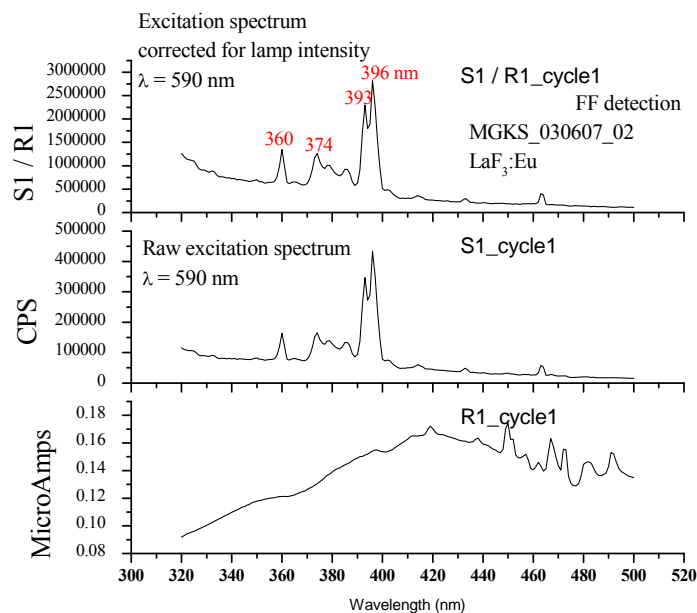


Fig. 7.7. Corrected excitation spectra of  $\text{LaF}_3:\text{Eu}^{3+}$  NCs.

Fig. 7.8(b) shows measured PL spectrum of Eu-doped  $\text{LaF}_3$ , which is to be compared with the spectrum obtained from  $\text{EuCl}_3$  precursor shown in Fig. 7.8(a). The same excitation wavelength of 396 nm was used in both cases. We interpret the changes in the Eu-related emission spectrum as evidence of a successful incorporation of the activator during the synthesis. Additional measurements performed using high resolution TEM, including elemental analysis of single NCs, further confirmed the presence of Eu in the NCs.

The spectra shown in Fig. 7.9 have been normalized to equal molarity of Ce halides in the DI water solutions. They reveal that the intensity of raw PL data from the same amount of Ce contained in the CNCs is over 10 times stronger than from  $\text{CeCl}_3$ . When corrected for system response, the CNC emission enhancement is even more dramatic, approaching 18.5 times. This result provides a very encouraging evidence of high-efficiency emission from activators inserted

in CNCs. We interpret the high efficiency of PL emission associated with Eu and Ce dopants, enhanced by quantum confinement effects, as evidence of successful incorporation of the dopant in the lanthanum fluoride CNCs.

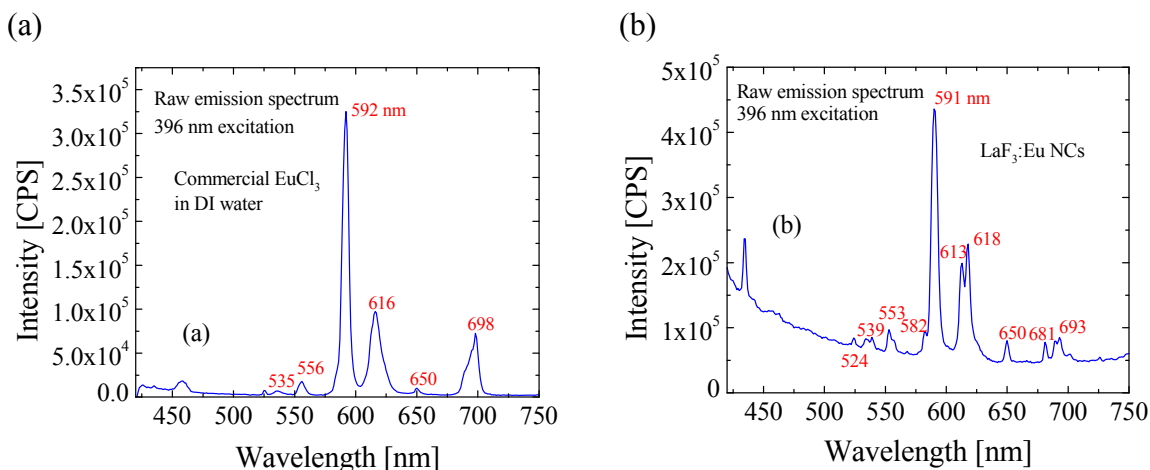


Fig. 7.8. Room-temperature raw PL spectra of (a)  $\text{EuCl}_3$  stock solution and (b) Eu-doped  $\text{LaF}_3$  CNCs. Excitation wavelength of 396 nm was chosen to maximize the NC signal.

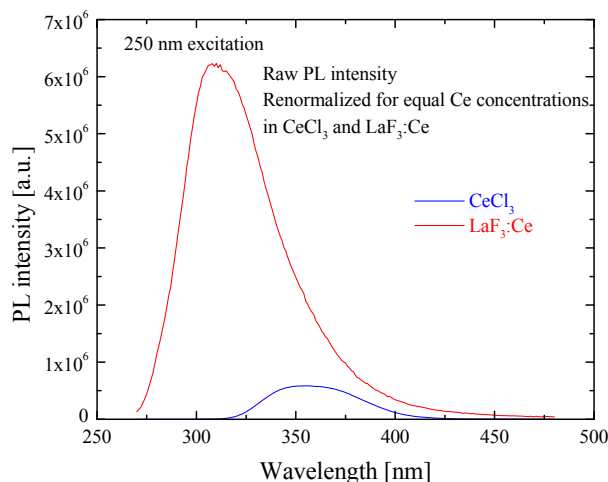


Fig. 7.9. Room-temperature raw PL spectra of  $\text{CeCl}_3$  stock solution (blue line) and  $\text{LaF}_3$  CNCs doped with 5% Ce (red line). The spectra are normalized to the same molarity of Ce halides in the DI water solution.

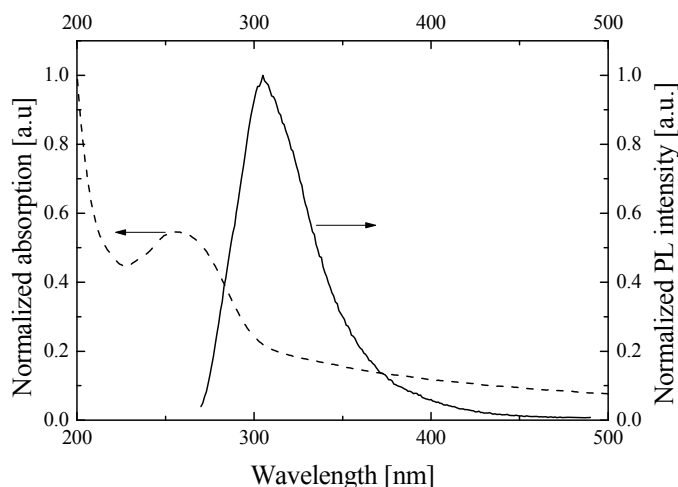
The normalized absorption and PL emission spectra of  $\text{LaF}_3:5\%\text{Ce}^{3+}$  CNCs are shown in Fig. 7.10. A significant Stokes shift of  $\sim 50$  nm can be observed.

The Eu- and Ce-doped CNCs synthesized at 75 °C in a mixture of HCl, ammonia, and water were observed to fluoresce in the visible ( $\sim 590$  nm) and UV ( $\sim 350$  nm) range, respectively, when excited at optimal excitation wavelengths, which is consistent with the standard emission wavelengths reported for similar lanthanum-based nanocrystalline materials doped with the same rare earths [Meiser 2004], [Stouwdam 2004], [Krämer 2006], [McKigney 2007]. Hence, the PL



emission and excitation spectroscopy measurements provide additional evidence that the synthesis of  $\text{LaF}_3:\text{Ce}^{3+}$ /chitosan CNCs was successful.

Fig. 7.10. Room-temperature PL and absorption spectra of  $\text{LaF}_3:5\%\text{Ce}^{3+}$  CNCs. 250 nm excitation was used for PL spectrum measurement.



As shown in Fig. 7.11, the emission spectrum of Ce-doped  $\text{LaF}_3$  matches very well the spectral range of high responsivity of bialkali photomultiplier tubes.

Our results agree well with the 249 nm absorption peak and emission peak in the 286 nm to 300 nm range reported for bulk  $\text{LaF}_3:\text{Ce}^{3+}$  [Moses 1990b], [Dorenbo 2000a], [Dorenbo 2000b]. As expected, no blue shift in emission was detected in  $\text{LaF}_3:\text{Ce}^{3+}$  CNCs as compared to bulk  $\text{LaF}_3:\text{Ce}^{3+}$  emission. While in many other NCs photoluminescence is a result of direct excitonic transitions, the mechanism of emission in  $\text{LaF}_3:\text{Ce}^{3+}$  material involves electronic transitions within  $\text{Ce}^{3+}$  luminescence centers. By affecting excitonic states in  $\text{LaF}_3$  host material, quantum confinement may improve the efficiency of energy conversion in  $\text{LaF}_3:\text{Ce}^{3+}$  scintillators, but energy levels of  $\text{Ce}^{3+}$  luminescence centers remain largely unaffected by it.

Fig. 7.11. Comparison of room-temperature PL emission spectrum of  $\text{LaF}_3:5\%\text{Ce}$  CNCs and quantum efficiency of Hamamatsu R7449 bialkali photomultiplier tube (PMT).

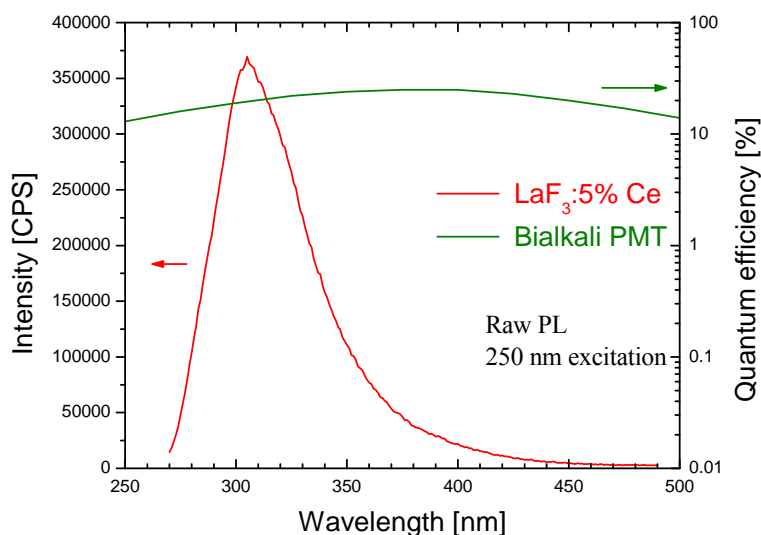


Fig. 7.12 shows the results of fluorescence lifetime measurements obtained for  $\text{Ce}_x\text{La}_{1-x}\text{F}_3$  CNCs with Ce contents of 5 and 10%. Two lifetime components fit the experimental data well for  $\text{LaF}_3:5\%\text{Ce}$  CNCs:  $\tau_1 = 10.0$  ns with the relative weight of 20%, and  $\tau_2 = 27.3$  ns with the relative weight of 80% [Fig. 7.12(a)]. For  $\text{LaF}_3:10\%\text{Ce}$  CNCs, a single lifetime of 28.8 ns provides a good fit to measured data [Fig. 7.12(b)]. These results are comparable to scintillation decay lifetimes observed in bulk  $\text{Ce}_x\text{La}_{1-x}\text{F}_3$  crystals using 511 keV  $^{22}\text{Na}$  source and a fine time bin grid (see Table 4.1), although good fit with a single lifetime of 18 ns was obtained when coarse time bins of more than 2 ns were used to represent the measured data [Moses 1990b]. In addition, a PL decay time of 18.3 ns at the emission wavelength of 303 nm was reported for bulk  $\text{LaF}_3:5\%\text{Ce}^{3+}$ , using the excitation wavelength of 270 nm [Wojtowicz 1994]. Although the energy conversion mechanisms are not the same in PL lifetime and scintillation decay measurements, nonetheless the results of the PL lifetime measurements provide a fairly good estimate of how fast  $\text{LaF}_3:\text{Ce}^{3+}$  nanoscintillators can be.

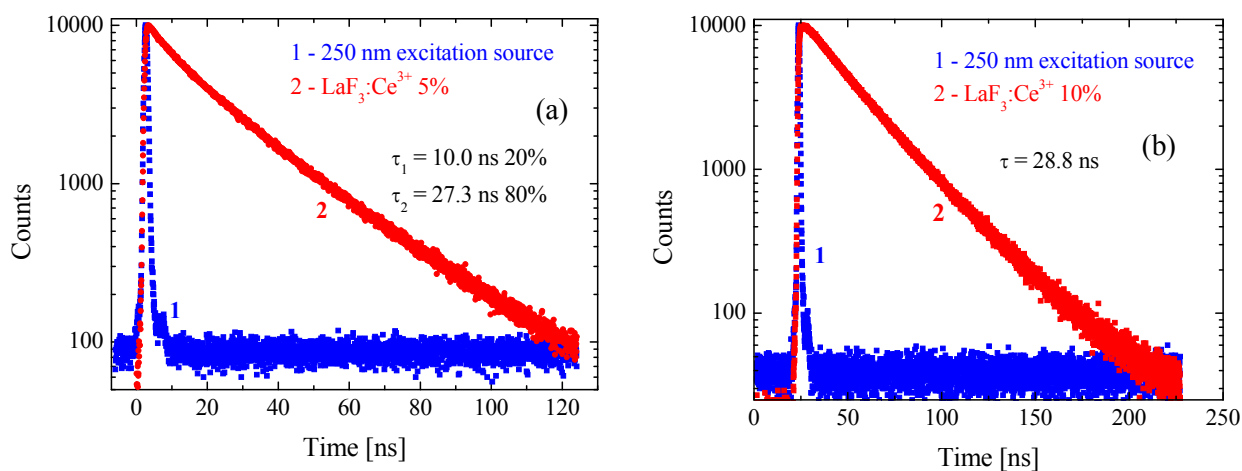


Fig. 7.12. Fluorescence lifetime data for  $\text{Ce}_x\text{La}_{1-x}\text{F}_3$  CNCs synthesized at 75 °C in a mixture of HCl, ammonia, and water: (a)  $x = 5\%$ ; (b)  $x = 10\%$ .

### 7.C. Optimization of Ce Content in $\text{LaF}_3:\text{Ce}$ Colloidal Nanocrystals

Although it may seem natural to expect enhanced PL emission from  $\text{LaF}_3:\text{Ce}^{3+}$  NCs with increased cerium concentration in NCs, there might exist an optimum in cerium concentration due to possibility of emission quenching at high cerium concentrations, which needs to be determined experimentally. Since higher Ce content is expected to lead to increased self-absorption of Ce emission [Moses 1990], an optimal concentration should exist that maximizes quantum efficiency at a fixed CNC concentration.

#### 7.C.a. Optical Characterization of $\text{Ce}_x\text{La}_{1-x}\text{F}_3$ Nanocrystals Synthesized Using Aqueous Route

The absorption measurements of  $\text{Ce}_x\text{La}_{1-x}\text{F}_3$  NCs synthesized using the aqueous approach, illustrated in Fig. 7.13, show four clearly resolved peaks at 206, 218, 234 and 248 nm. These four peaks agree well (see Fig. 4.1) with the internal  $4f \rightarrow 5d$  energy level configuration of  $\text{Ce}^{3+}$  ions doped into a  $\text{LaF}_3$  host matrix [Dorenbos 2000c].

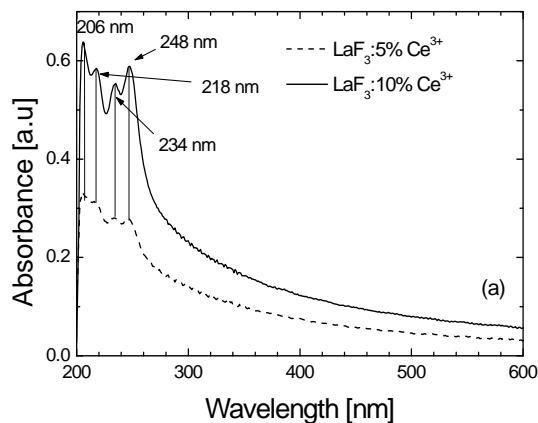


Fig. 7.13. Absorption spectra of  $\text{Ce}_{0.05}\text{La}_{0.95}\text{F}_3$  and  $\text{Ce}_{0.1}\text{La}_{0.9}\text{F}_3$  CNCs synthesized at 75 °C in a mixture of HCl, ammonia, and water.

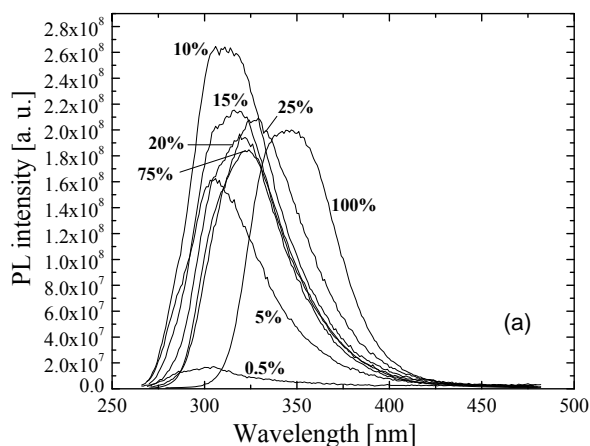


Fig. 7.14. PL emission spectra of aqueously synthesized  $\text{Ce}_x\text{La}_{1-x}\text{F}_3$  CNCs at various Ce contents. The molarity of each sample was kept constant at 0.1 M.

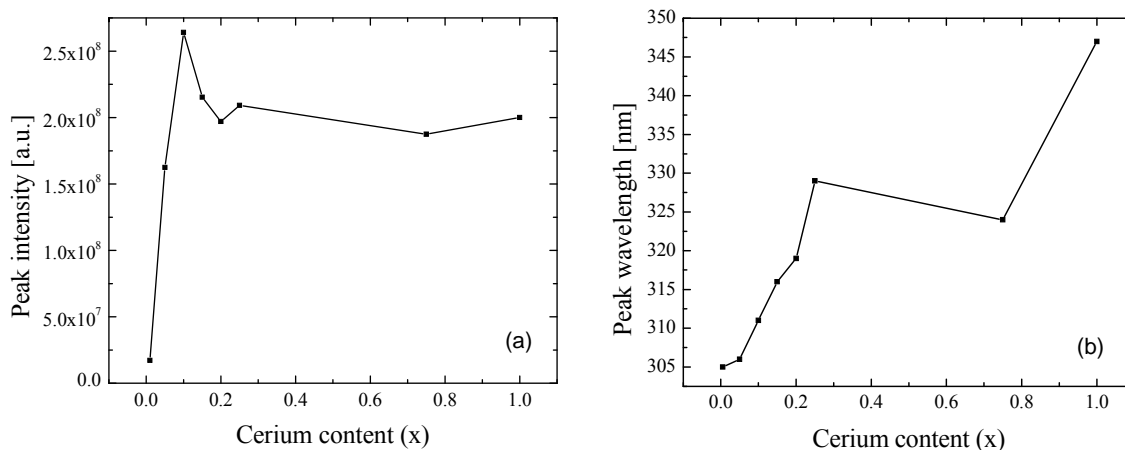


Fig. 7.15. Variation of (a) PL peak intensity and (b) PL peak position with increasing Ce content of  $\text{Ce}_x\text{La}_{1-x}\text{F}_3$  CNCs synthesized using aqueous route.

Fig. 7.14 shows the dependence of PL spectra on cerium content. The peak emission intensity and wavelength are plotted for increasing cerium content  $x$  in Fig. 7.15. An optimum is observed at  $x = 10\%$ . A sharp fall off in intensity is observed for the samples with 5% and 1% cerium concentration, whereas the emission intensity for higher concentration samples decreased only slightly. The peak emission wavelength red shifted with increasing cerium concentration, while an almost constant optimal excitation wavelength of  $\sim 250$  nm was observed in the PL excitation spectra for all the samples.

PL lifetime measurements showed a dominant decay component from 27.3 to 28.8 ns for 5% and 10% Ce content (see Fig. 7.12). This value is in good agreement with the dominant scintillation decay component for bulk  $\text{Ce}_x\text{La}_{1-x}\text{F}_3$  [Moses 1990b]. Although the energy conversion mechanisms are not the same in PL lifetime and scintillation decay measurements, nonetheless the results of the PL lifetime measurements provide a fairly good estimate of how fast  $\text{Ce}_x\text{La}_{1-x}\text{F}_3$  nanoscintillators can be by probing Ce intrinsic lifetime in  $\text{LaF}_3$ .

#### **7.D. Characterization of PEG-Capped $\text{LaF}_3$ Colloidal Nanocrystals Synthesized in Water**

##### **7.D.a. Structural Characterization of PEG-Capped $\text{LaF}_3$ Nanocrystals Synthesized in Water**

The PEG-capped  $\text{LaF}_3$  NCs were structurally characterized with TEM and HRTEM, subjected to elemental analysis with EDS, and the size distribution of the aqueous sample was measured with DLS.

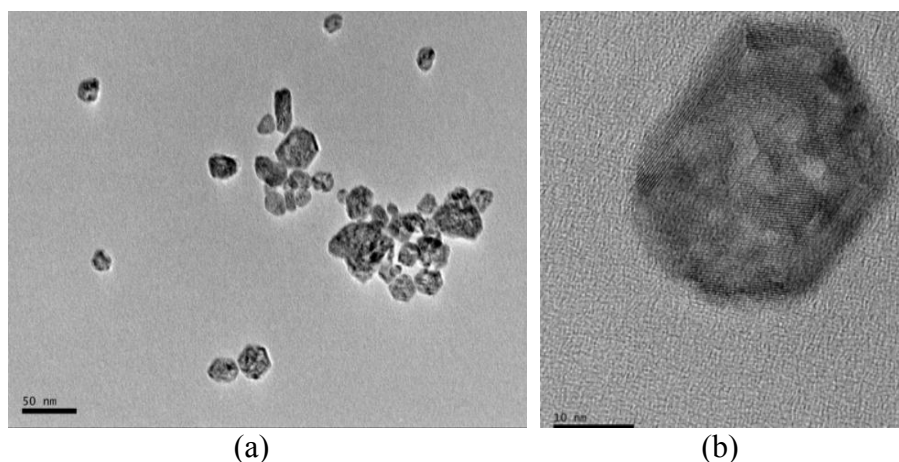


Fig. 7.16. (a) and (b): Bright-field TEM images of PEG-capped  $\text{LaF}_3\text{:Ce}^{3+}$  NCs. The scale bars are 50 nm and 10 nm, respectively.

Fig 7.16 contains the images obtained via TEM analysis, in which the PEG-capped Ce-doped  $\text{LaF}_3$  NCs appear as crystalline hexagonal platelets. The EDS spectrum for the PEG-capped  $\text{LaF}_3\text{:}10\%\text{Ce}^{3+}$  NCs is shown in Fig. 7.17. The presence of La and Ce can be confirmed; however the F line overlaps one of the La signals and therefore F cannot be unambiguously discerned. Fig 7.18 shows the size distribution histogram for the PEG-capped Ce-doped  $\text{LaF}_3$  CNCs, indicating the CNCs to have an average hydrodynamic diameter of 43.2 nm.

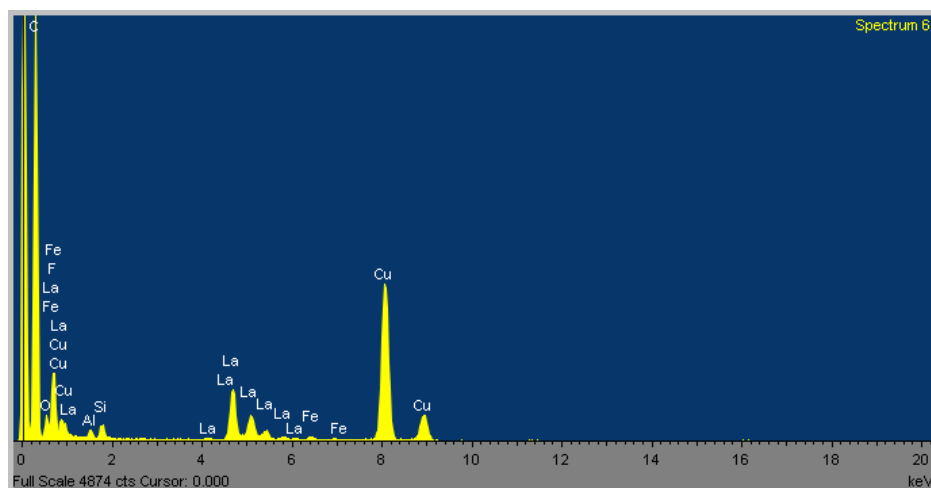


Fig. 7.17. EDS spectrum of PEG-capped  $\text{LaF}_3:10\%\text{Ce}^{3+}$  NCs, confirming the presence of La and Ce.

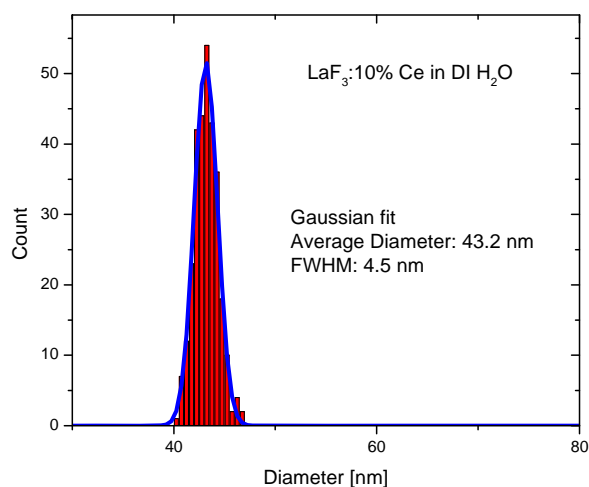


Fig. 7.18. DLS spectrum of PEG-capped  $\text{LaF}_3:10\%\text{Ce}^{3+}$  NCs, indicating a size distribution ranging between 41 to 45 nm diameters, with an average diameter of 43.2 nm.

#### **7.D.b. Optical Characterization of PEG-Capped $\text{LaF}_3$ Nanocrystals Synthesized in Water**

The PEG-capped Ce-doped  $\text{LaF}_3$  NCs were optically characterized with a spectrofluorometer and a spectrophotometer to determine the emission and absorption properties of the CNCs in water.

Fig. 7.19 shows the PL spectrum of the PEG-capped Ce-doped  $\text{LaF}_3$  NCs, with 250-nm excitation wavelength and an emission peak at 308 nm. Fig. 7.20 shows the absorption spectra of the PEG-capped Ce-doped  $\text{LaF}_3$  NCs dispersed in deionized water at various concentrations. Absorption measurements of the NCs were taken at four different dilutions. Following the measurements, specific volumes of the samples were dried and calcinated in order to determine the NC density in the samples.

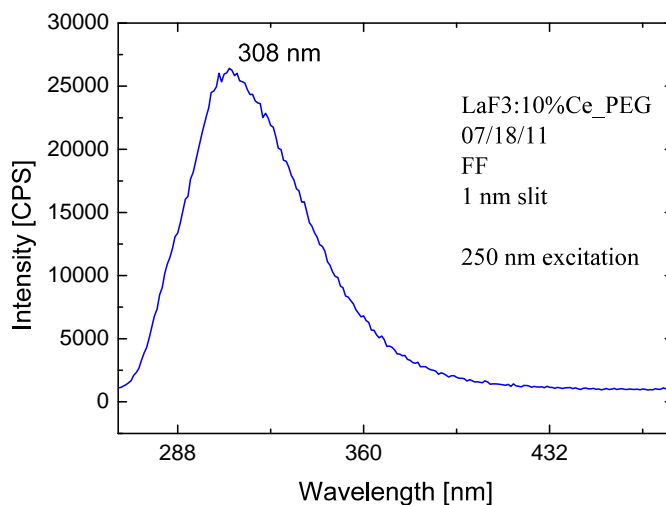


Fig. 7.19. PL spectrum of PEG-capped Ce-doped  $\text{LaF}_3$  NCs dispersed in water, using 250-nm excitation wavelength resulting in an optimal emission at 308 nm wavelength.

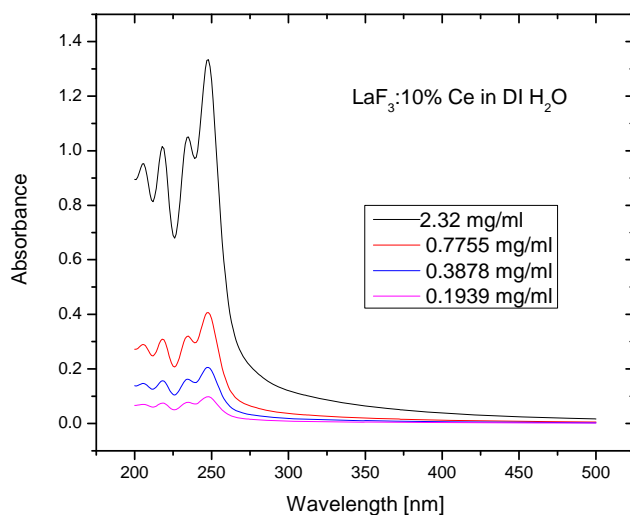


Fig. 7.20. Absorption spectra of PEG-capped Ce-doped  $\text{LaF}_3$  NCs dispersed in water at various concentrations.

## 8. CHARACTERIZATION OF LEAD-BASED SCINTILLATING NANOCRYSTALS (TASK 3, PART 2)

This section reports main accomplishments and new findings obtained under part of Task 3 devoted to structural and optical characterization of lead-based scintillating NCs.

## **8.A. Structural Characterization of Time-Evolving PbI<sub>2</sub>-Based Crystals**

### **8.A.a. Transmission Electron Microscopy and Corresponding Energy-Dispersive Spectroscopy Analysis of Time-Evolving PbI<sub>2</sub> NCs**

For initial structural characterization of PbI<sub>2</sub>-based NCs, TEM samples were prepared 9 days after synthesis by placing a drop of the colloidal solution onto a 200-mesh carbon-coated copper grid and allowing the solvent to dry, thus fixing the NCs on the grid. High-resolution transmission electron microscope, JEOL-2010 operating at 200 kV, was used with the OXFORD Link ISIS EDS apparatus.

Bright-field TEM images [Fig. 8.1(a)] show relatively monodisperse nanoparticles of about 7 to 15 nm in size. The high-resolution TEM images [Fig. 8.1(b)] indicate particles appearing to have a hexagonal crystalline structure. While the TEM images confirm presence of nanoparticles and their crystalline nature, the EDS analysis performed at the TEM facility confirms presence of both lead and iodine in the NCs (Fig. 8.2).

As described in Section 10, our studies of radiation hardness under gamma irradiation have led to discovery of continuous increase in the light intensity of both control and irradiated samples. In order to better understand possible origin of that phenomenon, we have performed another TEM study, which revealed formation of much larger crystals, illustrated in Fig. 8.3. Their elemental analysis using EDS setup on TEM was not possible, as they were too thick to provide data in the transmission mode. We have therefore used SEM for further analysis, as described in the next section.

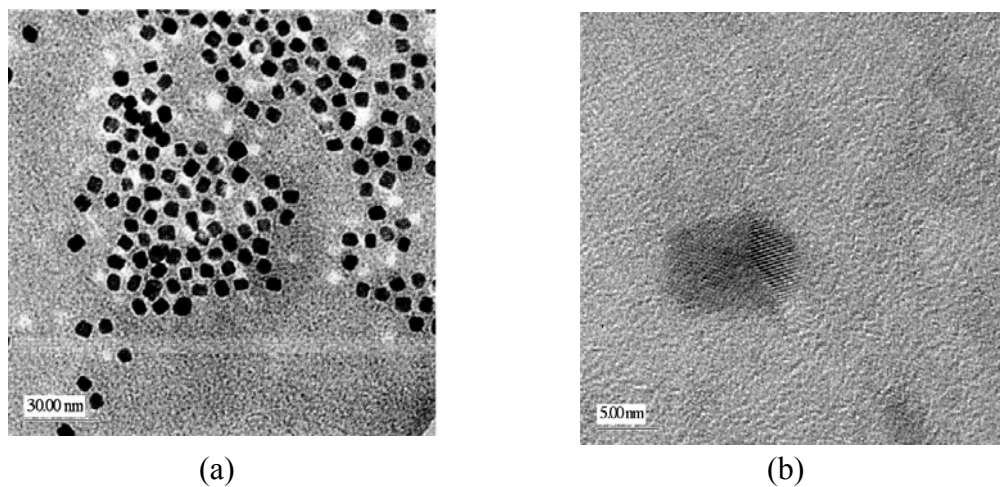


Fig. 8.1. (a) Bright-field TEM image and (b) high-resolution TEM image of PbI<sub>2</sub>-based NCs taken 9 days after synthesis.

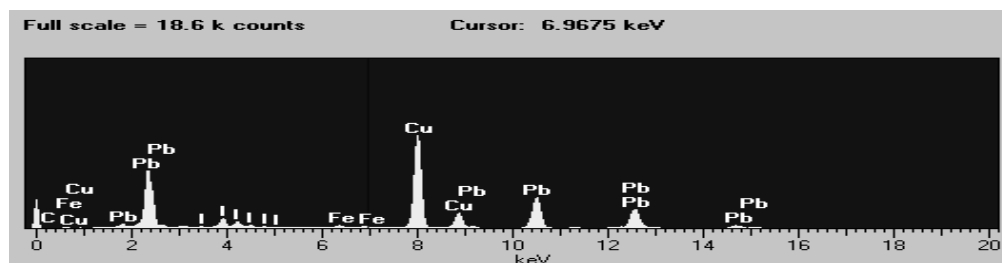


Fig. 8.2. EDS analysis of the  $\text{PbI}_2$ -based NCs obtained 9 days after synthesis, used in conjunction with the transmission electron microscope, shows multiple lead and iodine lines.

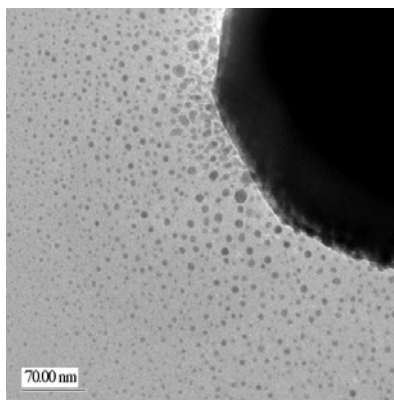


Fig. 8.3. Bright-field TEM image of lead-iodide-based NC sample 62 days after synthesis (magnification 40,000 $\times$ ). The electron beam current was 108  $\mu\text{A}$ . The scale bar is 70 nm.

#### **8.A.b. Scanning Electron Microscopy and Corresponding Energy-Dispersive Spectroscopy Analysis of Time-Evolving $\text{PbI}_2$ -Based Crystals**

For SEM imaging, a Hitachi S-5200 Nano SEM apparatus was used with a PGT Spirit software installed for EDS analysis.

Figs. 8.4(a),(b) show three-dimensional morphology of the  $\text{PbI}_2$ -based material as observed by SEM 105 days after synthesis. The SEM images revealed crystals of  $\sim 2 \mu\text{m}$  in size. A ditrigonal pyramidal class structure was inferred from these images.

The SEM EDS analysis [Figs. 8.4(c),(d)] confirmed the presence of lead and iodine in the crystals. Furthermore, the elemental analysis of the sample revealed that there was an equal percentage of oxygen along with lead and iodine.

The original procedure of [Finlayson 2006] was intended for synthesis of  $\text{PbI}_2$  NCs. Addition of DDA was supposed to stop growth by capping the NCs. We found this quenching procedure to be inefficient, as synthesized NCs left in THF/methanol/DDA solvent kept growing over time, reaching a micrometer size in about 3-month period.

Lead iodide is known to have hexagonal unit cell, on which, in principle, ditrigonal pyramidal class of crystals can be formed. Although over 40 polytypes of  $\text{PbI}_2$  have been reported in the literature [Chand 1975], we were unable to identify the microcrystals as belonging to any



polytype of  $\text{PbI}_2$ . Attempts to measure powder X-ray diffraction have not produced signals strong enough to interpret. Another possibility, strongly suggested by the SEM analysis of micro-scale crystals, was  $\text{PbIOH}$  (iodolaurionite). Its composition is consistent with the results of our SEM EDS elemental analysis (hydrogen does not show up on EDS spectra), and it belongs to orthorhombic crystalline system. We were also considering  $\text{Pb}_3\text{O}_2\text{I}_2$  (iodomendipite) of the lead oxyhalide family as a candidate material for the spontaneously formed optically active microcrystals that evolved from the original  $\text{PbI}_2$  synthesis. In order to verify these hypotheses, we have synthesized and characterized NCs made of these materials (see Sections 6.B-D and 8.C-E).

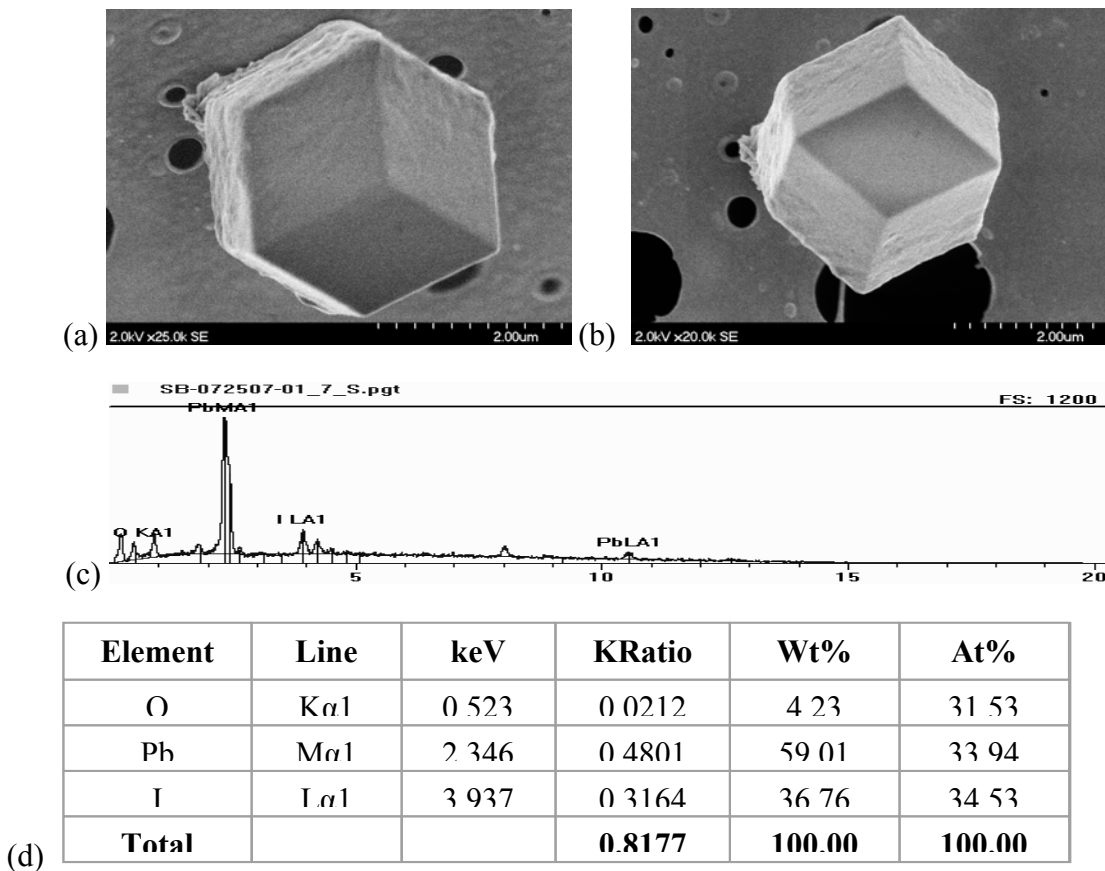


Fig. 8.4. (a) and (b) SEM images of micro-scale lead-iodide-based crystals showing ditrigonal pyramidal class structure; (c) EDS spectrum showing presence of lead, iodine, and oxygen, (d) elemental analysis table showing percentage composition of elements.

### 8.B. Optical Characterization of Time-Evolving $\text{PbI}_2$ -Based Crystals

PL spectra were collected using a Horiba Jobin Yvon Fluorolog-3 spectrofluorometer. PL was measured for the CNC solution as well as for the THF/methanol/DDA mixture of solvents. Using an excitation wavelength of 360 nm, we observed a blue PL with the peak centered at 437 nm [Fig. 8.5(a)]. The THF/methanol/DDA mixture of solvents emits in the UV, when excited at 270 nm [Fig. 8.5(b)].

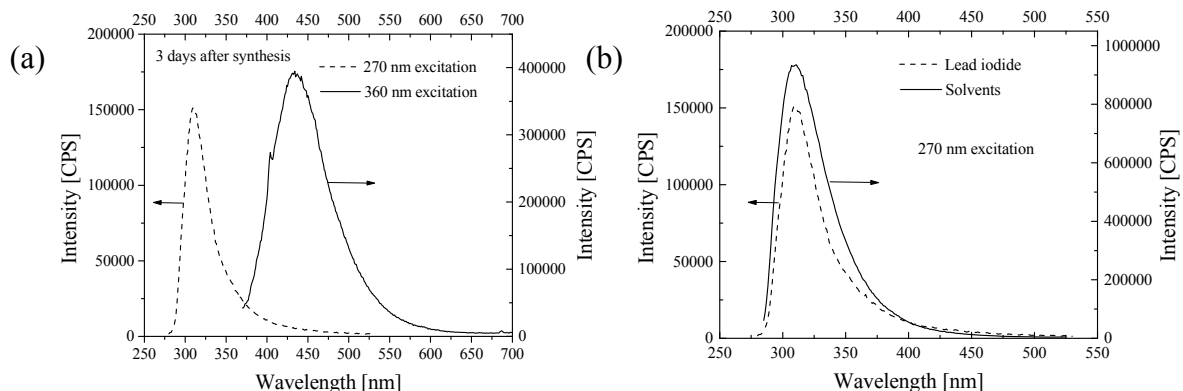


Fig. 8.5. Room-temperature PL emission spectra for the (a) CNC solution (b) solvent mixture: THF, anhydrous methanol, and DDA.

Absorption measurements were conducted using a CARY 400 UV-VIS spectrophotometer. The sample was prepared by adding three drops of the CNC solution to a 3:2 ratio mixture of THF and methanol. Another sample was prepared using only the THF/methanol/DDA mixture and was placed in the reference compartment of the spectrophotometer.

The absorption spectrum measured 2 days after synthesis (Fig. 8.6) clearly shows three discrete ultraviolet absorption peaks. The longest-wavelength peak around 360 nm corresponds to direct band-to-band transitions in the material (bandgap energy of 2.55 eV was reported for bulk  $\text{PbI}_2$  [Artemyev 1997]). When used for the excitation of the sample, it produces blue photoluminescence with the peak centered at 437 nm [Fig. 8.5(a)]. The middle peak in the absorption spectrum was identified as originating from the THF/methanol/DDA mixture of solvents [Fig. 8.5(b)]. The origin of the shortest wavelength peak in the absorption spectrum remains undetermined at present.

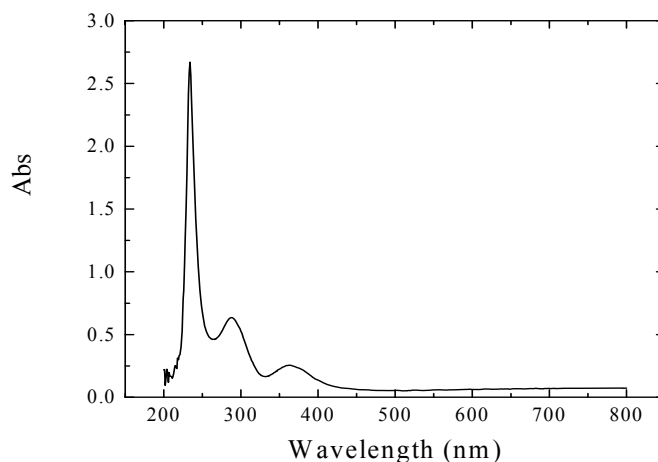


Fig. 8.6. Absorption spectrum of the lead-iodide-based NCs measured 2 days after synthesis.

In the process of conducting regular PL measurements at weekly intervals, associated with the radiation hardness testing (see Section 11), we have observed a steady increase in PL intensity from NC solutions in both control and irradiated samples. Fig. 8.7(a) shows about fourfold

increase in PL intensity over a period of 188 days after synthesis. No shift in spectral position of the peak was observed during that time [Fig. 8.7(b)]. The increase in PL intensity correlated with formation of larger-size crystals, as discussed in Section 8.A.

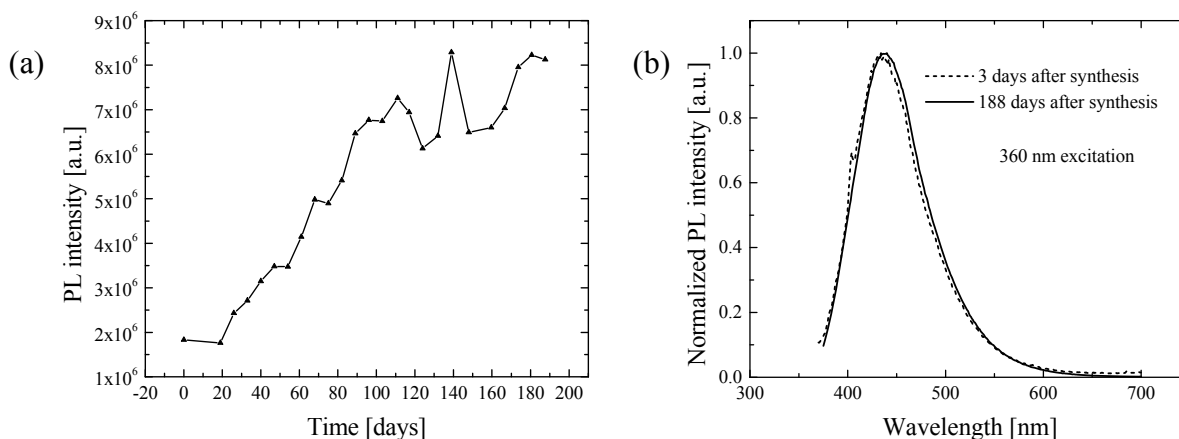


Fig. 8.7. (a) Observed increase in PL intensity for a control sample of lead-iodide-based NCs over 188 days after synthesis; (b) Spectral change in PL peak over that period of time.

### **8.B.a. Quantum Efficiency and PL Lifetime Measurements of Time-Evolving $\text{PbI}_2$ -Based Crystals**

According to the procedure established by Horiba Jobin Yvon [Porres 2006] and based on the method of deMello *et al.* [deMello 1997], quantum efficiency of the  $\text{PbI}_2$ -based material was measured in a dilute solution of the sample using the integrating sphere capability on the Horiba Jobin Yvon Fluorolog-3 spectrofluorometer. As distinct from comparative methods of measuring quantum efficiency, integrating sphere approach allows for absolute measurement of quantum efficiency over a wide spectral range.

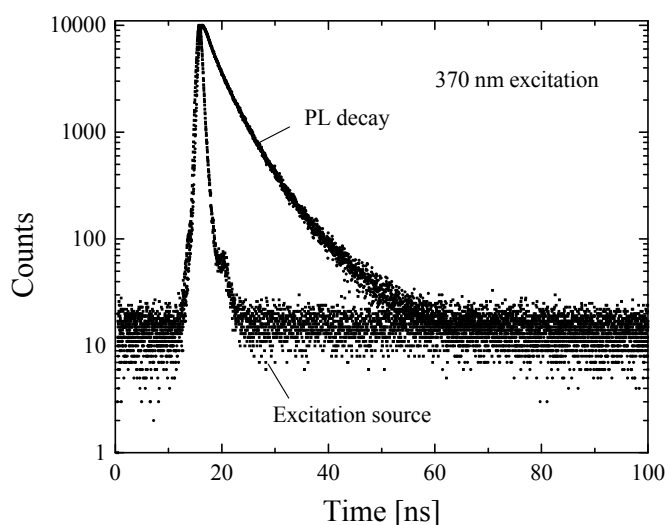


Fig. 8.8. Results of PL lifetime measurements for  $\text{PbI}_2$ -based NCs.

Quantum efficiency for the blue PL of the  $\text{PbI}_2$ -based material was measured at two different times after synthesis. Quantum efficiencies of 6.7% and 15.6% were recorded after 115 and 197 days after synthesis, respectively, which is consistent with the PL intensity increasing over time [Fig. 8.7(a)].

For emission associated with band-to-band transitions, the PL lifetime of NCs is expected to be shorter than that of bulk material. PL lifetime measurements for the  $\text{PbI}_2$ -based material, illustrated in Fig. 8.8, were taken on the Horiba Jobin Yvon Fluorolog-3 spectrofluorometer in a configuration allowing for time-correlated single photon counting. Very short PL lifetimes of  $\sim 4$  ns and  $\sim 4.2$  ns were obtained from the measurements taken, respectively, 148 and 190 days after synthesis. This is again consistent with the observed increase in PL intensity over time, and can be explained by a diminishing with time contribution of nonradiative recombination into carrier lifetime.

In comparison with other inorganic high-speed scintillators (Table 8.1), the synthesized  $\text{PbI}_2$ -based NCs possess the best combination of speed and efficiency.

Table 8.1. List of high-speed inorganic scintillators with their respective decay times and quantum efficiencies

- |  |
|--|
| <ul style="list-style-type: none"> <li>• <math>\text{YAlO}_3\text{:Ce}</math> <math>\tau = 25</math> ns, 21,000 phot/MeV, QE <math>\sim 7\%</math></li> <li>• <math>\text{LaBr}_3\text{:Ce}</math> <math>\tau = 35</math> ns, 61,000 phot/MeV, QE <math>\sim 21\%</math></li> <li>• <math>\text{LuAlO}_3\text{:Ce}</math> <math>\tau = 18</math> ns, 12,000 phot/MeV, QE <math>\sim 4\%</math></li> <li>• <math>\text{PbWO}_4</math> <math>\tau = 3</math> ns, 300 phot/MeV, QE <math>\sim 0.09\%</math></li> <li>• ZnO (fast component) <math>&lt; 0.8</math> ns, <math>&lt; 860</math> phot/MeV, QE <math>&lt; 0.2\%</math></li> </ul> |
|--|

### **8.C. Characterization of PbIOH Nanocrystals**

For structural characterization, TEM samples were prepared by placing a drop of the colloidal solution in a 200-mesh carbon coated copper grid and the solvent was allowed to dry, fixing the NCs on the grid. High-resolution transmission electron microscope, JEOL-2010 operating at 200 kV, was used with the OXFORD Link ISIS EDS apparatus.

Bright-field TEM images [Figs. 8.9(a) and 8.9(b)] show preferential ordering into wire-like structures. The high-resolution TEM image [Fig. 8.9(c)] indicates the presence of nanoparticles and confirms their crystalline nature. The EDS analysis (Fig. 8.10) confirms the presence of Pb, O, and I in the NCs.

The absorption spectrum measured for PbIOH NCs suspended in ethanol (Fig. 8.11) was similar to that of the  $\text{PbI}_2$ -based NCs (Fig. 3), and showed three absorption peaks at 220 nm, 270 nm, and 330 nm. However, as distinct from the  $\text{PbI}_2$ -based NCs, no room-temperature PL was observed from PbIOH NCs.

Cryogenic PL spectra were recorded on a custom made PL setup equipped with a closed-circuit helium cryostat. PL spectra were measured using the 325 nm line of a He-Cd laser (5 mW output

power) for excitation. The emission was collected at a right angle configuration, dispersed in a CVI 0.5 m Digikrom DK 480 monochromator, and detected using a cooled Hamamatsu R943-02 PMT detector with lock-in amplification. Samples were dried and affixed to a cold finger of a Model 22 CTI-Cryogenics Cryodyne Refrigeration System from Helix Technology.

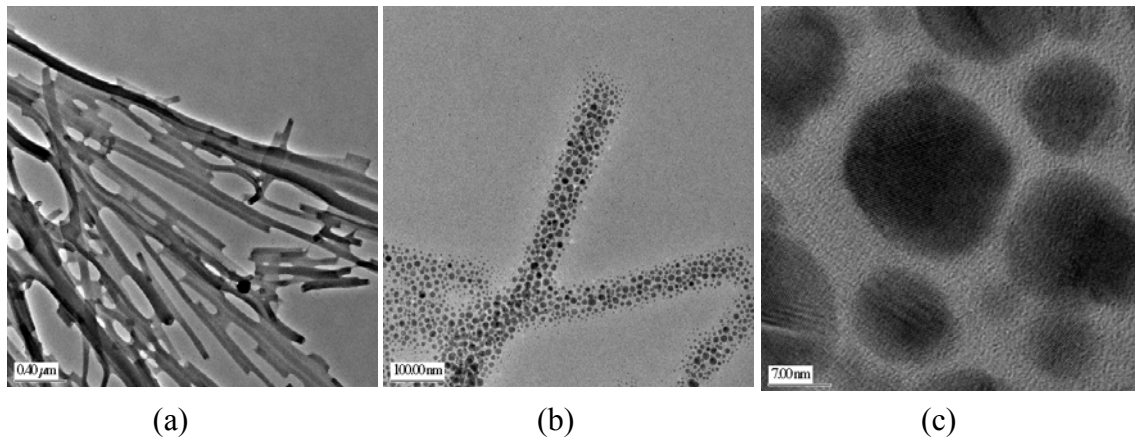


Fig. 8.9. TEM characterization of PbIOH CNCs: (a) Bright-field TEM image, scale bar 0.4  $\mu\text{m}$ ; (b) Bright-field TEM image, scale bar 100 nm; (c) High-resolution TEM image, scale bar 7 nm.

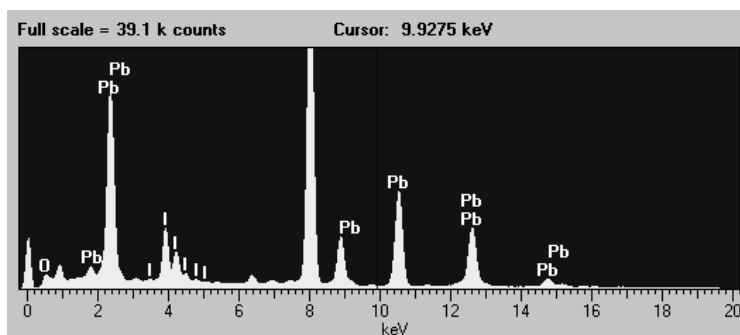


Fig. 8.10. EDS spectrum of PbIOH NCs.

PL spectra were measured at temperatures from 10 K up to 160 K, at which point the PL was completely thermally quenched. Below  $\sim 100$  K, PL was extremely bright with a broad emission spectrum peaked around 560 nm [Fig. 8.12(a)]. An Arrhenius plot [Fig. 8.12(b), based on the measured PL spectra, demonstrates the thermal quenching energy of  $\sim 0.45$  eV. In general, the observed results agree well with the previously reported results for bulk PbIOH crystals [Schwartz 1973].

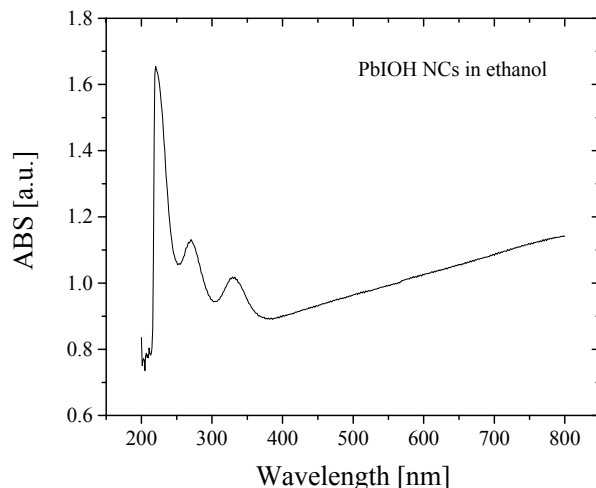


Fig. 8.11. Absorption spectrum of PbIOH NCs suspended in ethanol.

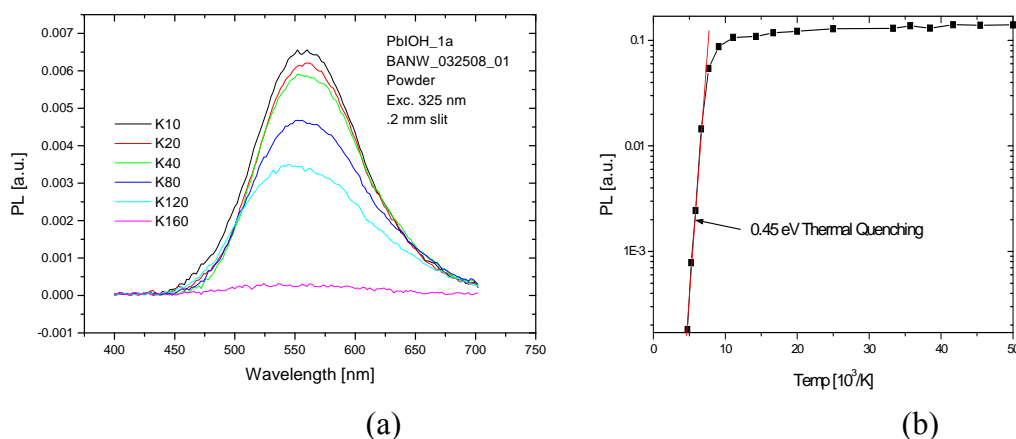


Fig. 8.12. PL characterizations of PbIOH CNCs: (a) PL spectra in the temperature range from 10 to 160 K; (b) Arrhenius plot.

#### **8.D. Characterization of Water-Soluble Pb<sub>3</sub>O<sub>2</sub>I<sub>2</sub> Nanocrystals**

Fig. 8.13(a) shows a bright-field TEM image of Pb<sub>3</sub>O<sub>2</sub>I<sub>2</sub> NCs synthesized using the method described in Section 6.C. The NCs have an average size of 10 nm, with a rather wide size distribution from ~2 nm to ~20 nm. Fig. 8.13(b) shows the result of EDS analysis of the Pb<sub>3</sub>O<sub>2</sub>I<sub>2</sub> CNCs, confirming the presence of lead, oxygen, and iodine.

DLS measurements were performed on diluted samples using a Wyatt DynaPro Titan DLS system. The DLS data show a broad size distribution of CNCs that peak at an average size of 5 nm (Fig. 8.14).

To optically characterize the CNCs, photoluminescence measurements were acquired using a Horiba Jobin Yvon Fluorolog 3 spectrofluorometer and absorption measurements were performed on a Cary 400 spectrophotometer.

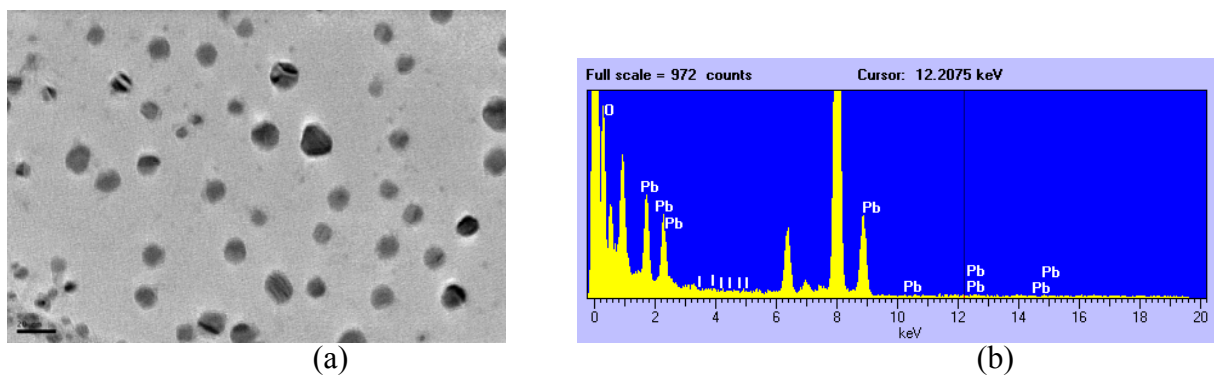


Fig. 8.13. TEM characterization of  $\text{Pb}_3\text{O}_2\text{I}_2$  NCs: (a) Bright field TEM image, scale bar 20 nm; (b) Results of EDS analysis.

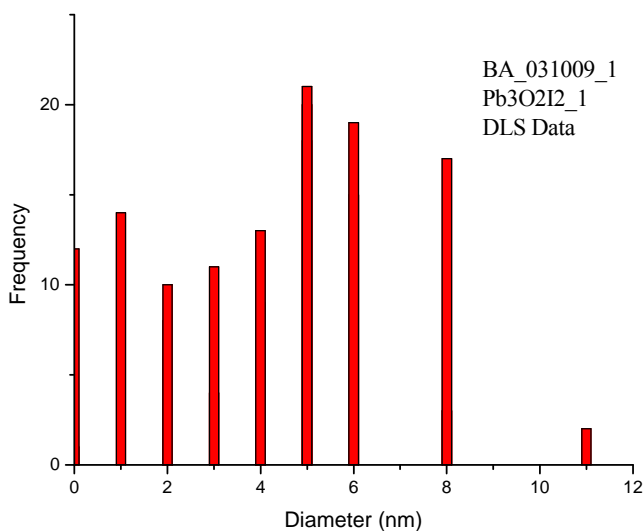


Fig. 8.14.  $\text{Pb}_3\text{O}_2\text{I}_2$  CNCs DLS measurement data.

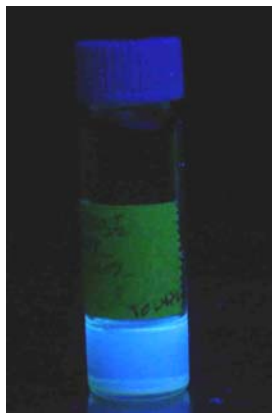


Fig. 8.15. Visible luminescence from  $\text{Pb}_3\text{O}_2\text{I}_2$  under UV lamp excitation.

The synthesized CNCs were optically very active and demonstrated very bright luminescence even under UV lamp excitation at room temperature (Fig. 8.15). Fig. 8.16 shows absorption,

photoluminescence excitation (PLE), and PL spectra of  $\text{Pb}_3\text{O}_2\text{I}_2$  NCs. According to the measured PLE spectrum [Fig. 8.16(b)], the optimum wavelength for excitation of the  $\text{Pb}_3\text{O}_2\text{I}_2$  NCs was 366 nm. Excitation of the NCs at that wavelength produced PL emission peak at 426 nm. We note here that both the optimal excitation wavelength and the PL emission peak position matched very closely those measured for the previously unidentified  $\text{PbI}_2$ -based NCs described in Section 8.B. For quantum efficiency measurements, a diluted sample was prepared and excited at 366 nm. The measured quantum efficiency for  $\text{Pb}_3\text{O}_2\text{I}_2$  NCs was  $\sim 30\%$ .

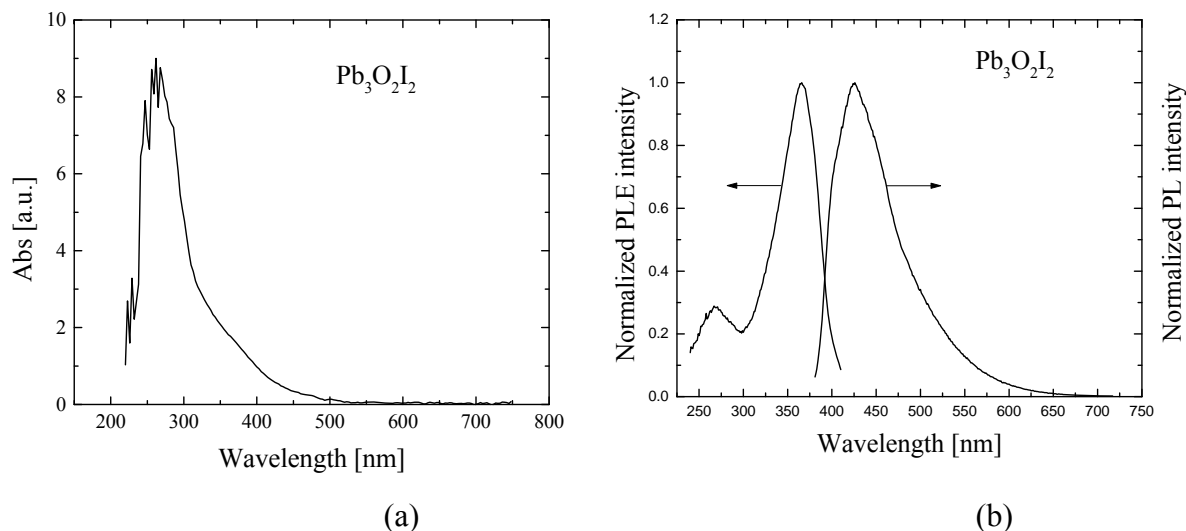


Fig. 8.16. Optical characteristics of  $\text{Pb}_3\text{O}_2\text{I}_2$  NCs: (a) Absorption spectrum; (b) PLE and PL spectra.

PL lifetime and quantum efficiency measurements were performed using a Horiba Jobin Yvon Fluorolog 3 spectrofluorometer. Three very fast PL decay components were extracted from the PL lifetime measurements performed on  $\text{Pb}_3\text{O}_2\text{I}_2$  NCs using a 370-nm pulsed LED source. The results of the PL lifetime measurements are summarized in Table 8.1, which shows the PL decay components and their relative weights.

Table 8.1. Summary of  $\text{Pb}_3\text{O}_2\text{I}_2$  NC lifetime measurements

Lifetime [ns]	Relative weight
1.167	19.98 %
3.573	54.80 %
7.147	25.22 %

## **8.E. Characterization of $\text{Pb}_3\text{O}_2\text{I}_2$ Nanocrystals Synthesized in TOPO**

### **8.E.a. Structural Characterization of $\text{Pb}_3\text{O}_2\text{I}_2$ Nanocrystals Synthesized in TOPO**

The  $\text{Pb}_3\text{O}_2\text{I}_2$  NCs synthesized in TOPO were structurally characterized by using bright-field TEM, as shown in Fig. 8.17.



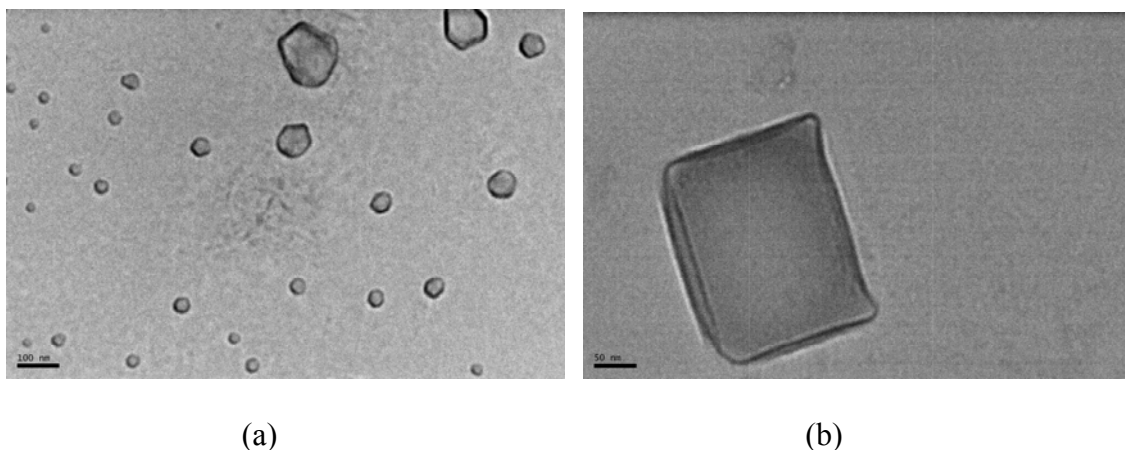


Fig. 8.17. (a) and (b): Bright-field TEM images of  $\text{Pb}_3\text{O}_2\text{I}_2$  NCs synthesized in TOPO. The scale bars are 100 nm and 50 nm, respectively.

#### **8.E.b. Optical Characterization of $\text{Pb}_3\text{O}_2\text{I}_2$ Nanocrystals Synthesized in TOPO**

The  $\text{Pb}_3\text{O}_2\text{I}_2$  NCs were optically characterized by using a spectrofluorometer and spectrophotometer to graphically visualize the sample's emission and absorption properties. The emission and absorption spectra obtained from the  $\text{Pb}_3\text{O}_2\text{I}_2$  NCs synthesized in TOPO are shown in Fig. 8.18.

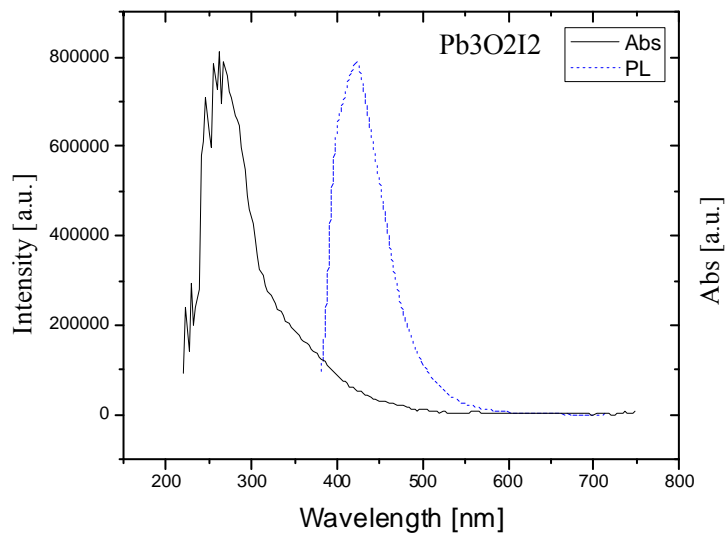


Fig. 8.18. Absorption and room-temperature PL spectra of  $\text{Pb}_3\text{O}_2\text{I}_2$  NCs synthesized in TOPO.

### **9. CHARACTERIZATION OF SCINTILLATING NANOCRYSTALS EMBEDDED IN POLYMERS (TASK 3, PART 3)**

Synthesized  $\text{LaBr}_3$  and  $\text{Pb}_3\text{O}_2\text{I}_2$  NCs were encapsulated in polyvinyl toluene (PVT) in order to produce nanoscintillators of much higher durability than conventional bulk crystal scintillators. Fig. 9.1 is an example of  $\text{Pb}_3\text{O}_2\text{I}_2$  NCs encapsulated in PVT.

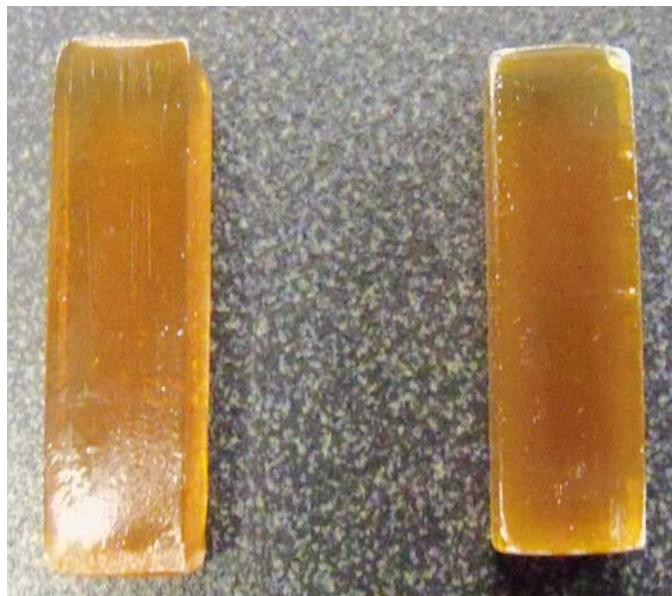


Fig. 9.1. Photograph of  $\text{Pb}_3\text{O}_2\text{I}_2$ /PVT nanocomposite samples.

The procedure for the suspension of nanoparticles in a PVT polymer matrix consists of running the vinyl toluene monomer liquid through an inhibitor removal column before transferring the solution into the glovebox and adding ~3% weight/volume (g/L) of 2,2'-azobisisobutyro-nitrile to the treated monomer. Afterwards, the solution is added and mixed with a dried sample of NCs and transferred to a 7 mL vial. In order to prevent the formation of bubbles during polymerization, the NC/monomer/initiator solution is subjected to a pre-polymerization step by placing the vial into a hot water bath at 60 °C for an hour. After pre-polymerization, the vial is kept in an oven overnight at 90 °C, completing the polymerization process and therefore encapsulating the NCs with PVT. After the polymer has hardened, the glass is broken off and the polymer is machined down to desired size.

### **10. DEMONSTRATION OF NANOCRYSTALLINE DETECTORS OF GAMMA RADIATION (TASK 4)**

There are several methods of detecting alpha, beta, and gamma radiation, but scintillation detection is often preferable due to its relatively low cost. Scintillation measurements basically involve two major components: a scintillation medium and a photodetector. The scintillation medium absorbs ionizing radiation and converts it into flashes of light. These flashes of light can be counted to provide information about the total flux of ionizing radiation passing through the scintillation medium for survey and dosimetry. For gamma radiation, the number of photons in each burst of flashes is directly related to the energy of the original gamma photon. Gamma ray

spectroscopy relies on sorting the individual flashes by the pulse height at the photodetector. This technique is called pulse height counting, and a schematic for how this is achieved is shown in Fig. 10.1.

The initial setup used for scintillation experiments employed a cooled GaAs PMT with precautions taken to remove light leaks and to increase the signal to noise ratio. This was accomplished through the construction of an improvised light blocking box using cardboard, aluminum foil, and black masking tape. This system was improved further by the addition of black metal foil purchased from Thorlabs.

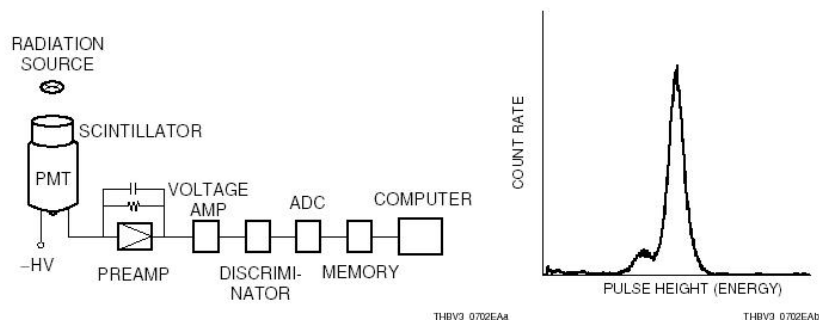


Fig. 10.1. Pulse height counting schematic [Hamamatsu 2008].

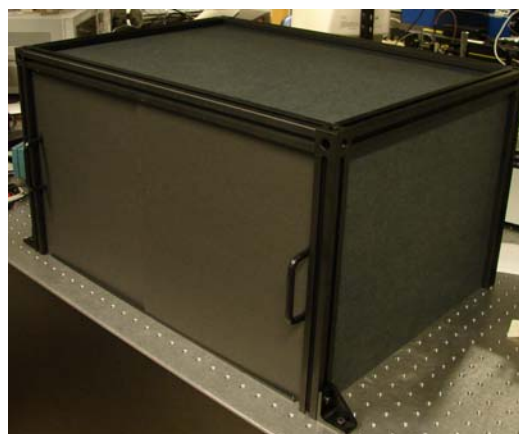


Fig. 10.2. Thorlabs light enclosure.

Another, more recent setup employs a Hamamatsu R7449 bi-alkali low noise PMT, designed specifically for scintillation counting, as well as an E7718 mu-metal housing, a C9028-01 high voltage supply/voltage divider circuit and a C6438 pre-amplifier. All these components are placed inside a Thorlabs light enclosure shown in Fig. 10.2. Further modification of the light enclosure with bulkhead electrical mounts and light sealing of the edges was performed.

### **10.A. Scintillation Response of LaF<sub>3</sub>:Ce Nanocrystals to Autunite**

In order to evaluate the potential of lanthanide halide NCs as nuclear radiation detectors, we have investigated [Fig. 10.3(a)] their response to background radiation levels and to closely placed piece of uranium ore, autunite. This natural ore of uranium, with the chemical formula of hydrated calcium uranyl phosphate  $\text{Ca}(\text{UO}_2)_2(\text{PO}_4)_2 \cdot 10\text{-}12\text{H}_2\text{O}$  [Locock 2003], was measured to have an activity of .14  $\mu\text{Ci}$ , and emitted multiple gamma rays from 100 keV to 1 MeV. For

comparison, a NaI:Tl bulk crystal was also used [Fig. 10.3(b)]. The data from a cooled GaAs PMT collected during experiments were analyzed using Maestro-32 Ortec pulse height discriminator for  $\gamma$ -ray spectroscopy. The hardware includes an MCA emulator with TRUMP-PCI card for multichannel pulse-height analysis. In order to allow the multichannel analyzer to accurately measure the peak height, all tests were performed with the  $RC$  time constants of the differentiating and integrating networks set to 10  $\mu$ s, resulting in the pulse width of  $\sim 25$   $\mu$ s. The pulses were also amplified 1000.89 times (V/V), which provided sufficient resolution to detect a single-photon peak. In cases, integration time was 100,000 s. In order to eliminate the possibility that the measured signal was due to causes other than the nanoscintillators, a series of additional measurements were taken, as explained in Fig. 10.3.

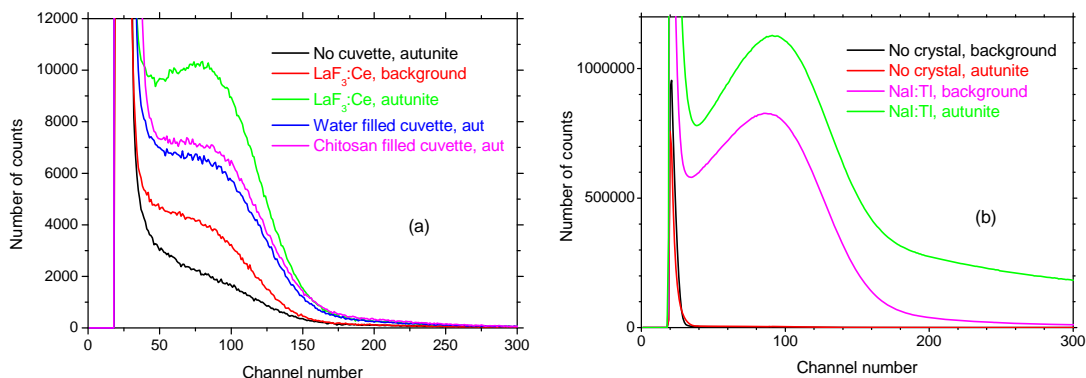


Fig. 10.3. Results of background radiation detection and autunite irradiation measurements using (a) Chitosan-coated LaF<sub>3</sub>:Ce NCs in a Suprasil cuvette filled with water, and (b) NaI:Tl bulk crystal.

Note that although the signal from the NCs was  $\sim 100$  times weaker than from NaI:Tl, their total mass was at least  $\sim 700$  times smaller than the mass of the bulk crystal. Taking this into account, the conversion efficiency of gamma energy into light appears to be much higher for the NCs than for the NaI:Tl bulk crystal.

The measurements of Fig. 10.3 clearly demonstrate that LaF<sub>3</sub>:Ce CNCs do produce a measurable signal even at the background radiation level. It should be noted that the 662 keV energy of  $^{137}\text{Cs}$   $\gamma$  photons is significantly greater than the 59 keV line of  $^{241}\text{Am}$  used in the experiments of Létant and Wang [Létant 2006b]. Thus, nanoscintillators are not limited to photon energies below 100 keV, as cautiously asserted in [Létant 2006b].

### **10.B. Scintillation Response of LaF<sub>3</sub>:Ce Nanocrystals to Monoenergetic Gamma Sources**

To further test LaF<sub>3</sub>:Ce<sup>3+</sup> CNCs for scintillation, two low-activity monoenergetic gamma sources were used, purchased from Spectrum Technologies. The first source, with the activity of 0.94  $\mu$ Ci at the time of measurement, was a  $^{57}\text{Co}$  disk with the gamma energies of 122.07 keV and 136.48 keV. Both of these energies are too low to cause Cherenkov radiation in water. The second source, with the activity of 0.67  $\mu$ Ci at the time of measurement, was a monoenergetic  $^{54}\text{Mn}$  disk with the gamma energy of 834.8 keV, exceeding the 800 keV threshold for generation of Cherenkov radiation in water. Scintillation events were detected using a custom system with a Hamamatsu R7449 quartz-window bi-alkali photomultiplier tube (PMT) at a bias of 910 V. The

electronic signal from the PMT was processed using Ortec 113 preamplifier, Ortec 570 amplifier and pulse shaper, and Ortec Illusion 25 multichannel analyzer. Data were analyzed using Ortec Maestro-32 for Windows software. The parameters of the Ortec 570 amplifier were: gain of 200 and a shaping time of 2  $\mu$ s. The cuvette that contained the  $\text{Ce}_x\text{La}_{1-x}\text{F}_3$  CNC solution was a Starna Cells 32/Q/20 flat cylindrical Spectrosil cuvette with an interior diameter of 19 mm and path-length of 20 mm, giving a volume of 5.6 ml. All surfaces of the cuvette, except for the front window, were coated with teflon tape to improve light collection. The radioactive source was placed 0.5 in from the back face of the cuvette. All measurements were taken over a live time of 5,000 s. The results are shown in Fig. 10.4.

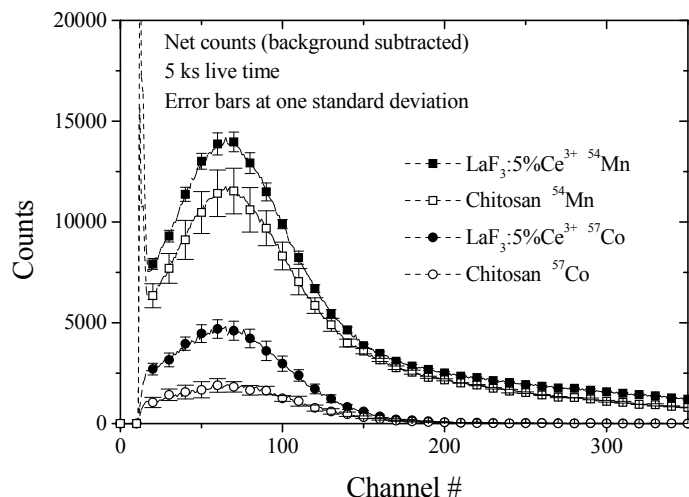


Fig. 10.4. Detection of scintillation from  $\text{LaF}_3:5\%\text{Ce}^{3+}$  CNCs under  $^{57}\text{Co}$  and  $^{54}\text{Mn}$  exposure.

To avoid false positives due to cosmic ray events and scintillation in the quartz, water, and chitosan coating, scintillation tests were carried out separately on 11.6 mg/ml chitosan blanks and the  $\text{LaF}_3:5\%\text{Ce}^{3+}$  CNC sample with a loading of 2.7 mg/ml. Fig. 10.4 shows a clear increase in counts for the  $\text{LaF}_3:5\%\text{Ce}^{3+}$  CNCs exposed to  $^{57}\text{Co}$ . Because of the low NC material content in the solution, the gamma spectra were not resolved in our experiments, which made it impossible to determine the light yield of the material. The future work on the development of this NC scintillating material will include its incorporation into a composite matrix, with an increased NC material loading to enable experimental determination of the light yield.

### **10.C. Scintillation Response of $\text{PbI}_2$ -Based Nanocrystals to Autunite**

To test the lead-iodide-based material for scintillation, the same 0.14  $\mu\text{Ci}$  autunite source was used as in Section 10.A. A Hamamatsu R943-02 PMT was used to detect scintillation events, and an Ortec multi-channel analyzer recorded the pulses. Four tests were performed to rule out possible false positives due to light leaks, scintillation of the glass cuvette, and scintillation of the solvent. All tests shown in Fig. 10.5 were taken over a period of 100,000 s.

Fig. 10.5 clearly demonstrates that the lead-iodide-based crystals do scintillate under gamma irradiation. While some background scintillation was observed from the quartz cuvette and the

solvent, the signal from lead-iodide-based material is much stronger, in spite of the minuscule quantity of the material.

Using Eqs. (4.1)-(4.6), we have calculated the thickness of material required to absorb half of the incident radiation at 511 keV for lead iodide, iodolaurionite ( $\text{PbIOH}$ ), iodomendipite ( $\text{Pb}_3\text{I}_2\text{O}_2$ ), and LYSO of the same composition as used in the GEMINI TOF PET [Surti 2007]. The radiation losses of secondary electrons are insignificant at the gamma photon energy of 511 keV [Attix 1986], [Gurler 2009], therefore  $\mu_{\text{en}} \approx \mu_{\text{tr}}$ , and for a compound material  $\mu_{\text{en}}$  can be estimated using a formula similar to Eq. (4.8). The results are summarized in Table 10.1.

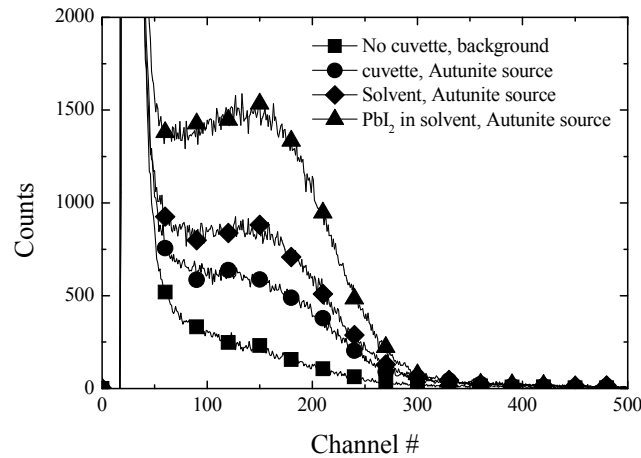


Fig. 10.5. Scintillation of lead-iodide-based crystals and test measurements in absence of lead-iodide-based crystals.

Table 10.1. Calculated material constants for  $\text{PbI}_2$ ,  $\text{Lu}_{1.8}\text{Y}_{0.2}\text{SiO}_5$ ,  $\text{PbIOH}$ , and  $\text{Pb}_3\text{I}_2\text{O}_2$  at 511 keV

Material	$\mu_{\text{en}}/\rho$ [ $\text{cm}^2/\text{g}$ ]	$\mu/\rho$ [ $\text{cm}^2/\text{g}$ ]	Density $\rho$ [ $\text{g}/\text{cm}^3$ ]	HVL thickness [cm]
$\text{PbI}_2$	0.0630	0.1233	6.16 <sup>(a)</sup>	0.91
$\text{Lu}_{1.8}\text{Y}_{0.2}\text{SiO}_5$	0.0566	0.1159	7.1 <sup>(b)</sup>	0.84
$\text{PbIOH}$	0.0691	0.1318	6.85 <sup>(c)</sup>	0.77
$\text{Pb}_3\text{I}_2\text{O}_2$	0.0736	0.1376	7.57 <sup>(d)</sup>	0.67

<sup>(a)</sup>[Klintenberg 2003]; <sup>(b)</sup>[McCallum 2005]; <sup>(c)</sup>[Dennis 1965]; <sup>(d)</sup>[Kramer 1985].

Table 10.1 shows that  $\text{PbI}_2$  has a higher mass energy-absorption coefficient than LYSO, but due to the material's lower density, lead iodide requires a larger thickness to absorb half of an incoming 511 keV gamma flux.  $\text{PbIOH}$ , on the other hand, has a larger mass energy-absorption coefficient, and, with its higher density, has a smaller half value layer thickness than LYSO.  $\text{Pb}_3\text{I}_2\text{O}_2$  has the largest mass energy-absorption coefficient of the four materials, and the highest density, resulting in the smallest half value layer thickness.

A decay time of 41 ns at room temperature was reported for LYSO scintillators [Pidol 2004], which is an order of magnitude longer than the room-temperature PL lifetime of  $\sim 4$  ns measured for our lead-iodide-based material.

### **10.D. Scintillation Response of $\text{Pb}_3\text{O}_2\text{I}_2$ Nanocrystals to Monoenergetic Gamma Sources**

To test  $\text{Pb}_3\text{O}_2\text{I}_2$  NCs for scintillation, two low-activity monoenergetic gamma sources were used, purchased from Spectrum Technologies. The first source was a bi-energetic  $^{57}\text{Co}$  disk source with the activity of  $0.87\ \mu\text{Ci}$  at the time of measurement, emitting gamma photons with energies of 122.07 keV and 136.48 keV, significantly below the Cherenkov radiation threshold of 707 keV in chloroform. The second source was a monoenergetic  $^{54}\text{Mn}$  disk source with the activity of  $0.63\ \mu\text{Ci}$  at the time of measurement, emitting gamma photons with energy of 834.8 keV. Scintillation events were detected with a Hamamatsu R7449 quartz window bi-alkali photomultiplier tube (PMT) biased at 910 V. The electronic signal from the PMT was processed using Ortec 113 preamplifier, Ortec 570 amplifier and pulse shaper, and Ortec Illusion 25 multichannel analyzer. Data were analyzed using Ortec Maestro-32 for Windows software. The parameters of the Ortec 570 amplifier were: gain of 200 and a shaping time of  $2\ \mu\text{s}$ . All measurements were taken over a live time of 5,000 s. Scintillation tests were performed on the as-synthesized  $\text{Pb}_3\text{O}_2\text{I}_2$  NC solution put into a cylindrical quartz cuvette. The interior dimensions of the cuvette were 19 mm diameter and 20 mm path length. Teflon tape was applied to all surfaces except for the front face of the cuvette [Fig. 10.6(a)]. The cuvette was placed with its uncovered face right in front of the PMT photocathode [Fig. 10.6(b)]. The 1-inch diameter disk sources were placed at the center of the cuvette, touching the back face of the cuvette.

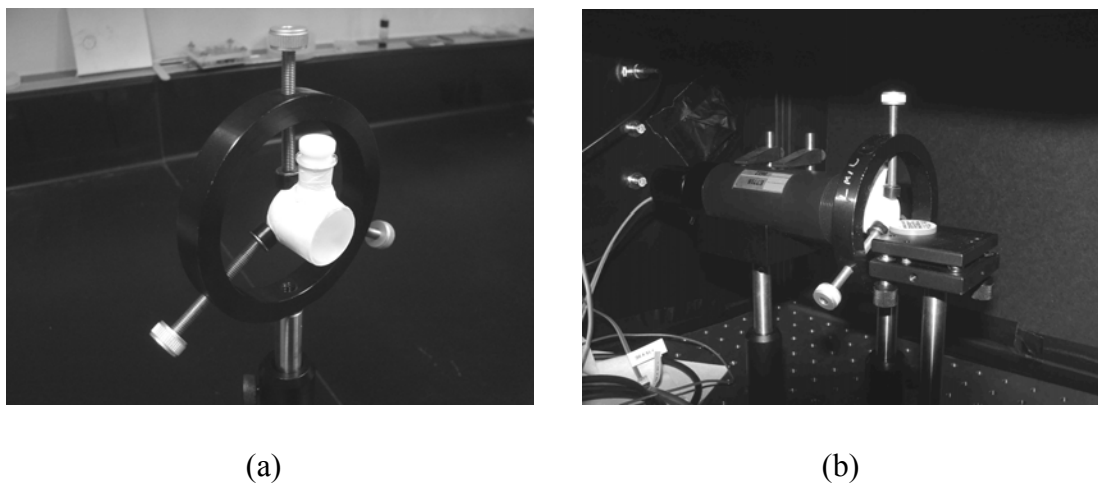


Fig. 10.6. (a) NC sample in a teflon-wrapped cylindrical cuvette, and (b) experimental setup used for the scintillation tests.

To avoid false positives due to cosmic ray events and scintillation in quartz or chloroform, additional scintillation tests were carried out separately on the cuvette filled with chloroform. As shown in Fig. 10.7, no increase in counts was observed for the NC sample as compared to the blank sample of chloroform-filled cuvette. On the contrary, we observed a higher number of counts from the blank sample in case of exposure to  $^{54}\text{Mn}$  source that was energetic enough to produce Cherenkov radiation in chloroform. We explain this result by assuming that the main scintillation component was Cherenkov radiation that was efficiently absorbed by the NC solution. No Cherenkov radiation was expected in case of exposure to  $^{57}\text{Co}$  source that produced



roughly equal number of counts from the NC and blank samples. We conclude that the concentration of NCs in this experiment was too small to observe their scintillation.

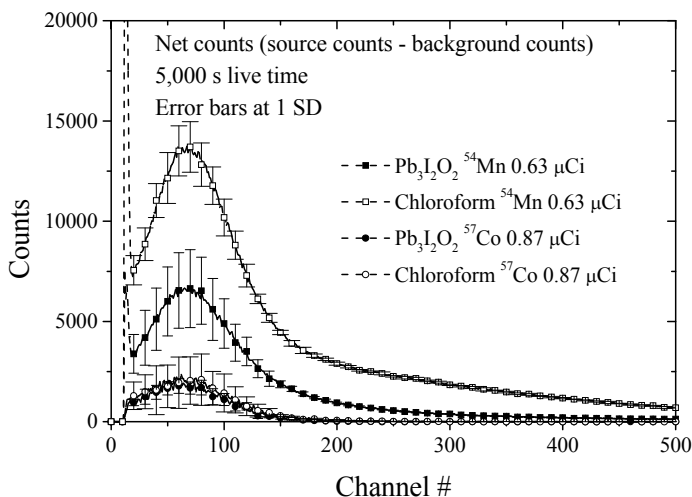


Fig. 10.7. Results of scintillation tests on  $\text{Pb}_3\text{O}_2\text{I}_2$  NCs exposed to  $^{57}\text{Co}$  and  $^{54}\text{Mn}$  sources.

## **11. STUDY OF NANOCRYSTAL RELIABILITY UNDER GAMMA IRRADIATION (TASK 5)**

For applications that involve exposure of CNCs to ionizing radiation, it is important to know the levels of irradiation that would degrade their optical properties. Except for our studies, no published data exist on the degradation effects of CNCs exposed to nuclear radiation

### **11.A. Eberline Source Calibration**



Fig. 11.1. Eberline 1000B multi-source gamma calibrator used in irradiation testing.

The equipment used in radiation hardness testing was a 1000B Eberline multi-source gamma calibrator (Fig. 11.1), located at the University of New Mexico Safety and Risk Services. The original  $^{137}\text{Cs}$  1sources have partially decayed since the manufacture of the device, and the



original activity documents have been lost, necessitating a re-calibration. This was accomplished with a Canberra Radiacmeter, a Geiger-Müller counter capable of measuring gamma flux up to 999 R/h. The detector itself was calibrated using Canberra Albuquerque's NIST-traceable gamma source. However, after calibration, there was a small linear mismatch between the measured values and the actual values, shown in Fig. 11.2.

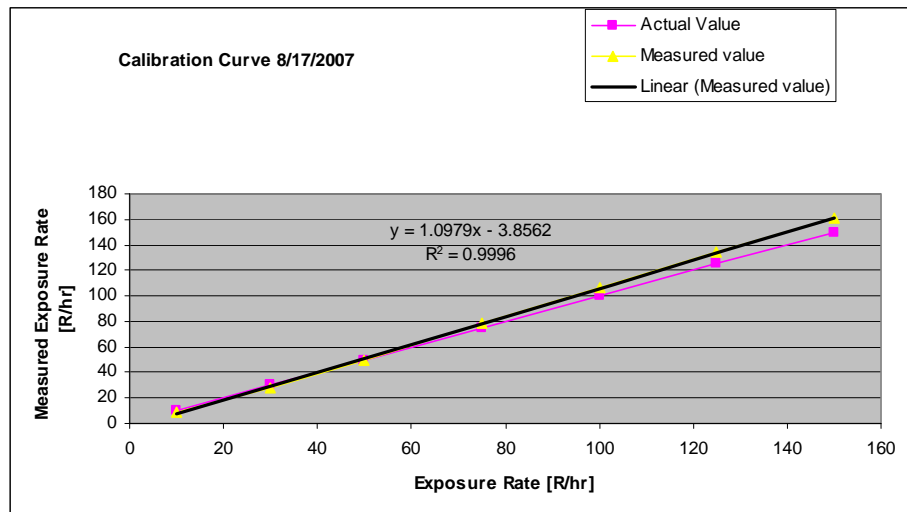


Fig. .11.2. Linear mismatch in calibration of Radiacmeter detector.

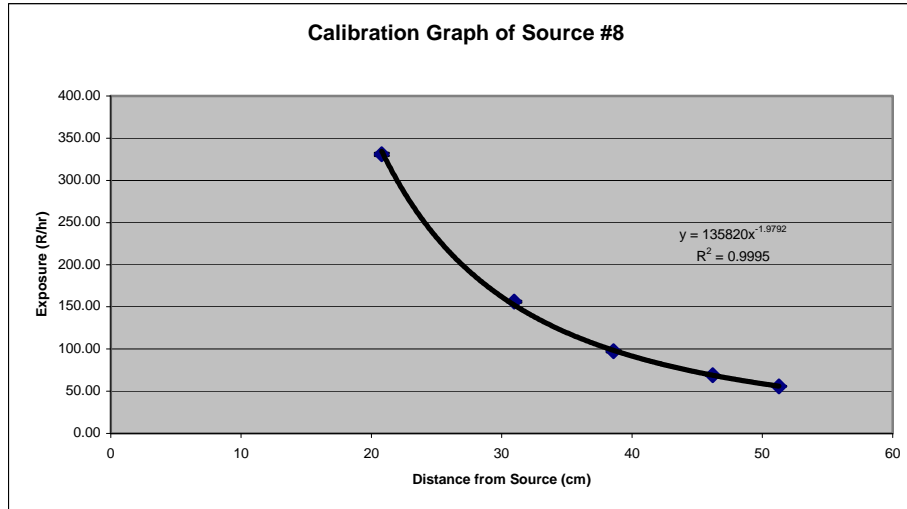


Fig. 11.3. Exposure rate vs distance for the strongest of Eberline 1000B sources.

This mismatch was removed through a linear transformation, thus reducing the error. The correction transformation is

$$\text{Corrected Value} = (\text{Measured Value} + 2.8562)/1.0979. \quad (11.1)$$

Measurements were taken at five distances from the source in the Eberline 1000B calibrator. These distances were 51 cm, 46 cm, 38 cm, 30 cm, and 20 cm, and were taken as an average of five readings that were each 2 min long, integrated over the measurement time internally. After correcting the values with Eq. (11.1), the data were plotted as shown in Fig. 11.3.

From this information, several parameters have been extracted. First, the original rate of exposure, to which CNCs were subjected in our early irradiation experiments, was at a rate of 97.3 R/h. Second, a maximum rate of exposure at the bottom of the exposure chamber was determined to be 330.3 R/h. Finally, the activity of the source was calculated as 39.7 Ci on the date of calibration, namely August 23, 2007.

### **11.B. Exposure to Dose Conversion**

When dealing with a radioactive source, we are able to indirectly measure the radiant gamma flux with various instruments in units of exposure (roentgens). This exposure has to be converted to an absorbed dose in rads. For a monoenergetic source, converting from roentgens to rads for a specific material can be calculated from the mass energy absorption coefficients using the equation [Cattaneo 1991]

$$D = 0.88[\mu_{\text{en}}(h\nu)/\rho]_{\text{X}}/(\mu_{\text{en}}(h\nu)/\rho)_{\text{air}}E, \quad (11.2)$$

where  $D$  is the absorbed dose in rads for material X,  $E$  is the exposure in roentgens, and  $[\mu_{\text{en}}(h\nu)/\rho]_{\text{X}}$  is the mass energy absorption coefficient for the subscripted material X.

Table 11.1. Absorbed dose conversion factors for selected CNCs at 662 keV

Nanocrystal material	$\mu_{\text{en}}(h\nu)/\rho$ [cm <sup>2</sup> /g]	rads/roentgen
CdSe	0.0300	0.90
PbI <sub>2</sub>	0.0463	1.39
LaF <sub>3</sub> :Eu 5%	0.0339	1.02
LaF <sub>3</sub> :Ce 5%	0.0337	1.01
ZnO	0.0284	0.85

The energy absorption coefficient at 662 keV for air is known as 0.0293 cm<sup>2</sup>/g [Hubbel 2004]. However, its values need to be calculated for compound CNCs from the elemental properties. Table 11.1 shows the calculated values of the mass energy coefficients and absorbed dose conversion factors for the materials of interest.

### **11.C. Effects of Gamma Irradiation on Colloidal Nanocrystals**

As no published data exist on the degradation effects of CNCs exposed to nuclear radiation, it is important to evaluate their radiation hardness. We are in the process of conducting gamma irradiation testing of various CNCs. Optical degradation of CNCs was evaluated based on the measured dependence of their room-temperature PL intensity on the irradiation dose. An Eberline 1000B multiple source gamma calibrator described in Section 11.A, with a 39.7 curie <sup>137</sup>Cs source emitting 662-keV gamma radiation, was used to study the effects of irradiation. In

order to accelerate the degradation process, the strongest of the available sources was used. The exposure rate was initially maintained at 97.3 R/h, and was later increased to 330.3 R/h when it became evident that the CNCs can sustain much higher exposures.

Optical degradation of the NCs was evaluated based on the measured dependence of their PL intensity on the irradiation dose. PL measurements were performed after weekly periods of irradiation to check if the NCs exhibited any signs of degradation in their optical characteristics. In order to exclude the effects of natural degradation, for example due to oxidative processes, on PL properties of the NCs, we prepared two identical samples of each material and measured their PL spectra prior to irradiation experiments, thus establishing the base line for monitoring PL dynamics under irradiation. One of the samples was then to be irradiated, while the other one, a “control” sample, was to be stored under RT conditions and to be used for comparison purposes. Assuming that both irradiated and control samples undergo the same aging process and react to environmental changes in the same way, we corrected the results of PL degradation measurement of irradiated sample for any changes in PL intensity of corresponding control sample with respect to its base line measurement.

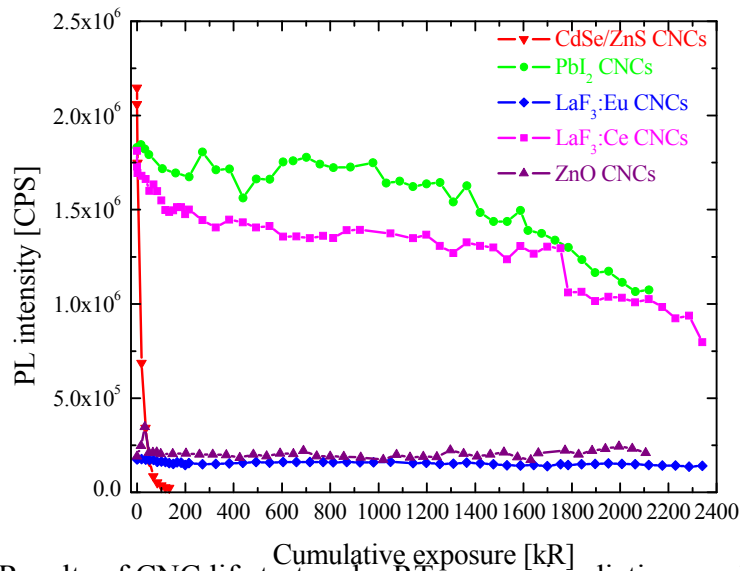


Fig. 11.4. Results of CNC life test under RT gamma irradiation conditions. Note rapid degradation of the CdSe/ZnS NCs, and very good performance of LaF<sub>3</sub>:Ce NCs.

A summary of testing results is shown in Fig. 11.4. The PL output in Fig. 11.4 is normalized to its original level by comparing with the control sample, and shown as a function of cumulative exposure in roentgens. The measured values of PL intensity were taken at the peak of PL emission.

The CNCs under test showed a wide range of radiation hardness. The CdSe/ZnS quantum dots (QDs) turned out to be most sensitive, having lost 50% of their light output after ~11.5 krad of absorbed dose. The other four materials demonstrated much better radiation hardness. The LaF<sub>3</sub>:Ce CNCs lost 20.5% of their light output after 722 krad of absorbed dose. Changing the dopant to europium increased the radiation hardness, with only 9.1% of light output having been lost in LaF<sub>3</sub>:Eu CNCs after 739 krad of dose. The absolute luminescence of LaF<sub>3</sub>:Eu CNCs,

however, is an order of magnitude lower than that of the  $\text{LaF}_3\text{:Ce}$  CNCs. The  $\text{ZnO}$  CNCs displayed no degradation in light output up to an absorbed dose of 505 krad. This excellent radiation hardness is compromised, however, by a very low light output of  $\text{ZnO}$  CNCs, comparable to that of  $\text{LaF}_3\text{:Eu}$  CNCs. Little radiation damage was observed in the  $\text{PbI}_2$ -based CNCs, which preserved a high level of luminescence up to 747 krad of absorbed dose, with a 9.1% decrease in PL intensity.

As described in Section 8.B, surprisingly, the PL output of both the control and irradiated  $\text{PbI}_2$ -based samples not only has not degraded with time, but it kept improving [see Fig. 8.7(a)].

It is clear from Fig. 11.4 that  $\text{CdSe/ZnSe}$  QDs degrade rapidly under gamma irradiation, while lanthanide halide and lead halide NCs display a remarkable stability. We attribute the loss of luminescence from  $\text{CdSe/ZnSe}$  QDs to low threshold energy for generation of defects in II-VI materials, the problem that plagued the development of II-VI-based diode lasers [Chuang 1998].

#### **11.D. Rapid Degradation of CdSe/ZnS Colloidal QDs Exposed to Gamma Irradiation**

$\text{CdSe/ZnS}$  QDs have been suggested as scintillators for detection of alpha particles and gamma rays [Dai 2002], [Létant 2006a], [Létant 2006b].

##### **11.D.a. Synthesis of CdSe/ZnS Colloidal QDs**

$\text{CdSe}$  cores were synthesized according to a modified procedure of Aldana *et al.* [Aldana 2001]. First, the cadmium precursor (cadmium acetate) was dissolved in a coordinating solvent, trioctylphosphine oxide (TOPO). The solution was heated in a flask under controlled argon atmosphere to 325 °C, while a solution of selenium in trioctylphosphine (TOP) and toluene was prepared in an argon-filled glovebox with < 0.1 ppm of water vapor and oxygen. When the temperature of the solution in the flask reached 325 °C, the selenium precursor solution was rapidly injected into the flask. When the contents of the flask reached red color, the solution was cooled to room temperature by removing the heat source.  $\text{CdSe}$  cores were precipitated in a centrifuge using acetone and methanol, and collected in hexanes. For  $\text{ZnS}$  coating, the zinc precursor was prepared by dissolving the zinc alkyl alkoxide ( $\text{ZnONEP}$ ) with oleic acid and octadecene, while the sulfur precursor was prepared by dissolving sulfur in octadecene. Both precursors were heated to 200-250 °C and the zinc precursor was cooled to 60-80 °C, while the sulfur precursor was cooled to room temperature. The  $\text{CdSe}$  NCs in hexanes were mixed with octadecene and octadecylamine in a flask and heated to 100 °C under vacuum for 30 minutes and then under argon to 240 °C. At that point, three alternating injections of calculated amounts of zinc and sulfur precursors were made at 10-minute intervals. Finally the solution was cooled to room temperature, QDs were precipitated with acetone and methanol, and collected in hexanes.

##### **11.D.b. Gamma Irradiation Testing**

An Eberline 1000B multiple-source gamma calibrator was used to study the effects of irradiation on  $\text{CdSe/ZnS}$  QDs. In order to accelerate the degradation process, the strongest of the available sources was used, namely a  $^{137}\text{Cs}$  source with the activity of 39.7 Ci, emitting 662 keV  $\gamma$  rays.

Optical degradation was evaluated based on the measured dependence of RT PL intensity on the irradiation dose. Using a Horiba Jobin Yvon Fluorolog-3 spectrofluorometer, PL measurements were performed after regular weekly periods of irradiation to check if the QDs exhibited any signs of degradation in their optical characteristics. In order to separate irradiation-induced phenomena from possible effects of natural degradation due, for example, to oxidative processes, the irradiated sample had a control counterpart from the same synthesis batch that was not subjected to irradiation. Assuming that both the irradiated and control samples stored at RT underwent the same natural aging processes and reacted to environmental changes in the same way, we corrected the results of PL degradation measurements of the irradiated sample for any changes in PL intensity of the control sample with respect to its baseline measurement performed prior to irradiation.

PL lifetime measurements were taken on the same spectrofluorometer in a different configuration, allowing for time-correlated single photon counting. Using a 375-nm pulsed diode laser source, the resolution of lifetime measurements was  $\sim 100$  ps. An integrating sphere accessory on the spectrofluorometer was used to measure quantum efficiency of the sample prior to and after irradiation.

Fig. 11.5(a) summarizes the results of the irradiation testing of CdSe/ZnS QDs. The PL intensity was taken at the peak of PL emission, which shifted slightly towards shorter wavelengths with increasing dose. CdSe/ZnS QDs, initially very bright, showed a rapid loss of light output when exposed to 662 keV  $\gamma$  rays, and were removed from the experiment after 133.2 kR cumulative exposure. An examination of PL spectra of these QDs revealed an irradiation-induced blue shift of the PL emission peak from the original 579 nm to 570 nm [Fig. 11.5(b)]. The CdSe/ZnS material system is known to be 12% lattice-mismatched [Xie 2005], which causes the bandgap of CdSe to reduce under strain. We tentatively explain the observed blue shift in the PL emission peak by irradiation-induced defects of the QD crystalline structure that lead to partial strain relaxation.

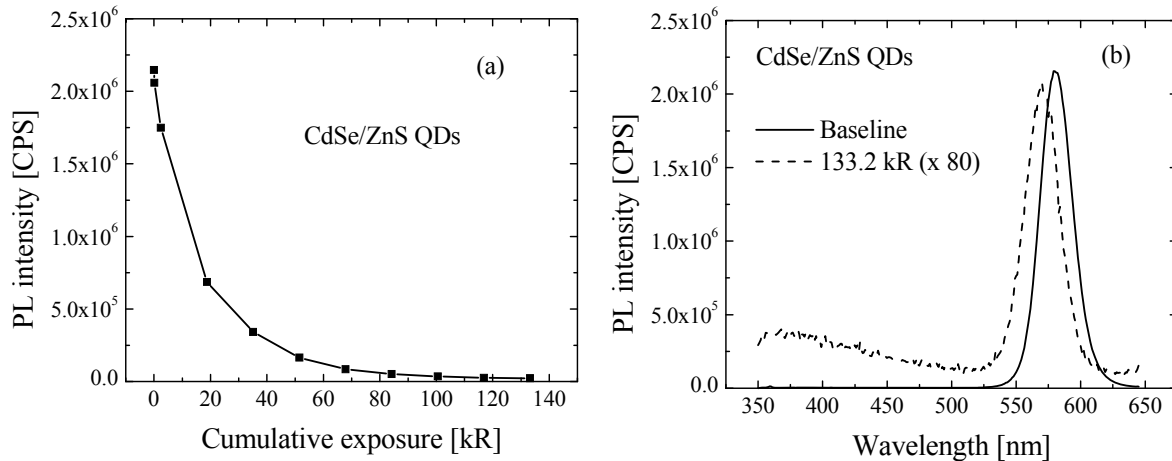


Fig. 11.5. (a) Peak PL intensity in counts per second for CdSe/ZnS QDs as a function of cumulative exposure  $E$  in kR. (b) Spectral changes in PL response of CdSe/ZnS QDs induced by 662 keV  $\gamma$ -ray irradiation.

In order to enable a comparison of radiation hardness of CdSe/ZnS QDs with that of other materials, the exposure in roentgens  $E$  has to be converted to an absorbed dose in rads  $D$  using Eq. (5.2). While the mass energy absorption coefficient for air at 662 keV is known to be  $0.0293 \text{ cm}^2/\text{g}$  [Eckerman 2003], its value for CdSe needs to be estimated using the constituent element data according to Eqs. (2.3)-(2.6). The calculated absorbed dose conversion factor for CdSe at 662 keV was found to be  $0.899 \text{ rad/roentgen}$ .

In terms of the absorbed dose, the CdSe/ZnS QDs turned out to be of very poor radiation hardness, having lost 50% of their light output after only  $\sim 11.5 \text{ krad}$  of absorbed dose [equivalent to  $\sim 11.3 \text{ krad(Si)}$ ], rendering them unsuitable for aerospace and terrestrial applications where radiation hardness up to total  $\gamma$ -ray doses of  $250 \text{ Mrad}$  is a prerequisite. This should be contrasted with excellent radiation hardness of GaN/InGaN multiple-quantum-well LEDs, which can sustain  $250 \text{ Mrad(Si)}$  from  $^{60}\text{Co}$  source with  $\sim 45\%$  loss in their PL intensity [Khanna 2005]. It should be pointed out, however, that CdSe/ZnS QDs still outperform the standard NaI:Tl scintillating crystals, which according to Normand *et al.* rapidly lose the light output after exposure to merely  $500 \text{ rad}$  of absorbed dose from  $^{60}\text{Co}$  source [Normand 2007].

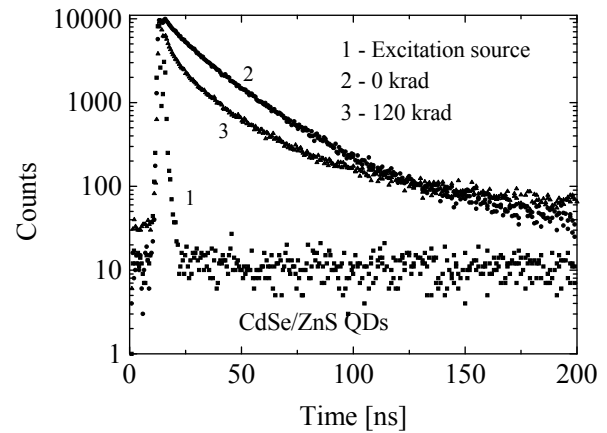


Fig. 11.6. Effects of  $\gamma$  irradiation on PL lifetimes for CdSe/ZnS QDs.

Fig. 11.6 shows PL decay data for the CdSe/ZnS QDs, obtained prior to irradiation and after  $120 \text{ krad}$  of absorbed dose. The observed changes in PL lifetime were accompanied by a reduction in quantum yield from  $23.4\%$  to  $0.2\%$ . A triple-exponential fit was used to achieve good agreement with each of the measured PL decay curves in Fig. 11.6. The decay time constants and the relative percentage weights of the decay components are summarized in Table 11.2.

Table 11.2. Results of a multiexponential fit to the data shown in Fig. 11.6

Sample	$A_1$	$\tau_1 \text{ (ns)}$	$A_2$	$\tau_2 \text{ (ns)}$	$A_3$	$\tau_3 \text{ (ns)}$
Control	6.31	1.3	67.46	16.24	26.23	41.5
Irradiated	14.78	0.73	39.17	9.08	46.05	32.6

#### **11.D.c. Mechanisms of Rapid Degradation under Gamma Irradiation**

The current understanding of the exciton decay dynamics in CNCs is still very fragmentary, even for the most thoroughly investigated CdSe QDs. Initial studies of the band-edge luminescence lifetimes revealed that the low-temperature exciton lifetime of CdSe QDs was orders of

magnitude longer (microseconds versus  $\sim 1$  ns) than that in the bulk CdSe [Bawendi 1992], [Nirmal 1994]. These observations were initially ascribed to surface localization of the photogenerated hole. However, further experiments using fluorescence line-narrowing (FLN) spectroscopy on surface-modified CdSe and CdSe/ZnS QDs [Kuno 1997] combined with theoretical analysis [Efros 1996] established that the energetics and dynamics of the excitonic PL could be understood in terms of the intrinsic band-edge exciton fine structure, with surface effects being responsible solely for the nonradiative relaxation pathways.

Crystal shape anisotropy and confinement-enhanced electron-hole exchange interaction lift the spin degeneracy of the band-edge exciton such that the ground state with net spin projection  $J = 2$  is electric-dipole forbidden from direct radiative recombination and therefore optically inactive. This “dark” ground exciton state is separated from the nearest optically active “bright” ( $J = 1$ ) exciton state by the energy gap  $\Delta = 1 - 15$  meV that scales inversely with the QD size [Efros 1996]. This model is strongly supported by the observed insensitivity of the absorption, band-edge PL, and FLN spectra to the properties of the QD surface [Kuno 1997]. Temperature and size-dependence of radiative exciton lifetimes and, in particular, the anomalously long low-temperature exciton lifetimes are well explained by thermal mixing of “dark” and “bright” exciton states separated by the size-dependent energy gap [Crooker 2003], [Labeau 2003], [Donega 2006].

The dynamics of band-edge PL decay is typically multi-exponential at short times, while at longer times, after the excitons have thermalized, the radiative decay closely follows a single exponential. It is this, longer, single-exponential decay component, demonstrating strong temperature and size-dependence and largely insensitive to surface nonradiative effects, that is identified as exciton radiative lifetime [Crooker 2003]. The faster decay dynamics at short times, on the other hand, is clearly affected by nonradiative defect-related pathways. Previous work has shown that the quality of the QD synthesis determines the shape of the time-resolved emission decay [Donega 2003]. As the surface and lattice structure of CdSe core is improved and the quantum yield increases to as high as 80%, the faster multi-exponential dynamics at short times effectively disappears, and the decay becomes single exponential in character, with the lifetime of  $\sim 30$  ns.

We have observed the drop in quantum yield from 23.4% to 0.2% after 120 krad of absorbed dose, which results from gamma-irradiation-induced nonradiative recombination channels and, within the framework of the “dark” exciton model, is expected to affect the short lifetime component in the PL decay data of Fig. 10.6. Using the fastest decay component from Table 10.2, and assuming that it originates from both radiative and nonradiative decay of the “bright” exciton state, we can estimate the irradiation-induced nonradiative exciton lifetime as follows. Prior to irradiation,  $1/\tau_1 = 1/\tau_r + 1/\tau_{nr}$ , while after irradiation  $1/\tau_1^* = 1/\tau_r + 1/\tau_{nr} + 1/\tau_{nr}^\gamma = 1/\tau_1 + 1/\tau_{nr}^\gamma$ , where  $\tau_{nr}^\gamma$  is the irradiation-induced nonradiative exciton lifetime. With  $\tau_1 = 1.3$  ns and  $\tau_1^* = 0.73$  ns, we arrive at  $\tau_{nr}^\gamma \sim 1.66$  ns. We note, however, that this mechanism alone cannot account for the dramatic reduction in the quantum yield. Indeed, if the nonradiative decay of the “bright” exciton were the only nonradiative recombination pathway, the value of  $\tau_1^*$  would have to be  $\sim 65$  times shorter than that given in Table 11.2. We explain the observed quantum yield drop by a very strong irradiation-induced nonradiative pathway that involves direct trapping of excited carriers by irradiation-induced defects, without formation of the excitons.

## **12. NUMERICAL SIMULATION OF GAMMA DETECTION IN NANOCRYSTALS (TASK 6)**

The results of MCNPX simulations of gamma detection are described in Section 15.A, as they were carried out to interpret simultaneous detection of gamma and thermal neutron radiation from a  $^{252}\text{Cf}$  source.

## **13. COLLOIDAL SYNTHESIS OF LANTHANIDE HALIDE NANOCRYSTALS WITH NEUTRON CAPTORS (TASK 7)**

As a continuation of our work on nanocrystalline materials for nuclear radiation detection, we have developed protocols for colloidal synthesis of  $\text{GdF}_3$  NCs,  $\text{GdF}_3$  NCs doped with Ce, and  $\text{LaF}_3$  NCs doped with Gd for neutron detection applications.  $\text{GdF}_3$ ,  $\text{GdF}_3\text{:Ce}$ , and  $\text{LaF}_3\text{:Gd}$  NCs were characterized by TEM, energy-dispersive X-ray spectroscopy (EDS), dynamic light scattering (DLS) analysis, and steady state UV-VIS optical absorption and photoluminescence (PL) spectroscopy. Scintillation was observed from Gd-containing NC material in experiments on neutron detection.

### **13.A. Gadolinium as a Neutron Detector**

Standard detectors of slow neutrons rely on the  $^{10}\text{B}(\text{n},\alpha)$ ,  $^6\text{Li}(\text{n},\alpha)$ , or  $^3\text{He}(\text{n},\text{p})$  reactions. The thermal neutron cross section for the  $^{10}\text{B}(\text{n},\alpha)$  reaction is 3840 barns, and the natural abundance of  $^{10}\text{B}$  is 19.8%. The most common detector based on the boron reaction is a  $\text{BF}_3$  gas tube. Boron-loaded scintillators are also used, although they encounter the challenge of discriminating between gamma rays backgrounds and gamma rays due to neutrons. The thermal neutron cross section for the  $^6\text{Li}(\text{n},\alpha)$  reaction is 940 barns, and the natural abundance of  $^6\text{Li}$  is only 7.4%. This requires enrichment of  $^6\text{Li}$  isotope, and increases the cost of the scintillators in which  $^6\text{Li}$  is embedded. The thermal neutron cross section for the  $^3\text{He}(\text{n},\text{p})$  reaction is 5330 barns, but its natural abundance of only 0.0001% results in even higher cost than  $^6\text{Li}$ .

A dramatic illustration of the burning need for novel concepts in neutron detection is the recent crisis with the interrupted deployment of 1,300-1,400  $^3\text{He}$  neutron detectors (each costing ~\$800,000) by the Department of Homeland Security (DHS) [Wald 2009]. After spending \$230 million to develop those detectors, with the intent of installing them in ports around the world to monitor possible attempts to smuggle radioactive materials, DHS was forced to stop the deployment due to the shortage of  $^3\text{He}$ , with the demand exceeding the supply by a factor of 10.

Gadolinium has the highest thermal neutron absorption cross-section of any naturally occurring element. Two isotopes of Gd with very high thermal neutron absorption cross-sections are  $^{157}\text{Gd}$  ( $\sigma_n = 253,000$  barns with 24.8% natural abundance) and  $^{155}\text{Gd}$  ( $\sigma_n = 60,700$  barns with 14.8% natural abundance) [Sonzongi 2009]. Even without any isotopic enrichment, naturally occurring Gd has an average value of  $\sigma_n = 49,000$  barns [Barbalace 2009]. Gadolinium emits low-energy conversion electrons and atomic X-rays in over 50% of the neutron captures, which makes it a very attractive dopant for a variety of neutron detectors. In addition to low-energy (up to 80 keV) conversion electrons, capture of a thermal neutron produces a cascade of associated Auger electrons, X-rays, and gamma rays ranging in energy from few eV to several MeV. All these



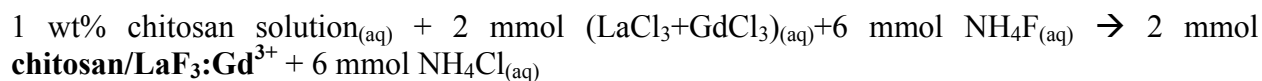
radiations are available to produce significant light output in a suitable efficient scintillating material.

Gd-containing organic liquid scintillators are commercially available [Banerjee 2007]. Like all liquid scintillators, they require very careful handling and must be stored and used in oxygen-free and water-free environment. Containers for these liquids must be sealed, and the liquids must be thoroughly bubbled with inert gas prior to sealing. At the same time, very few references have been found in a literature search for Gd-containing solid-state scintillators. They include gadolinium oxyorthosilicate  $\text{Gd}_2\text{O}_3\text{S}$  (GOS) [Schillinger 2001],  $\text{GdF}_3$  [Shestakova 2005],  $\text{Gd}_2\text{O}_3$  [Shestakova 2007],  $\text{GdI}_3\text{:Ce}$  [Glodo 2006], and Gd-loaded plastic scintillators [Ovechkina 2009]. Under this task, we explore a novel concept of Gd-containing nanocrystalline materials for neutron detection.

### **13.B. Colloidal Synthesis of $\text{LaF}_3\text{:Gd}$ , $\text{GdF}_3$ , and $\text{GdF}_3\text{:Ce}$ Nanocrystals**

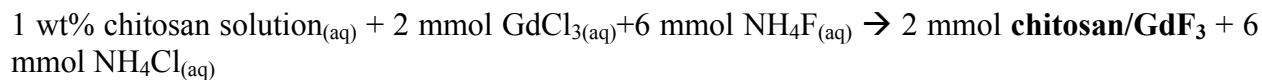
$\text{LaF}_3$  doped with 10% Gd,  $\text{GdF}_3$ , and  $\text{GdF}_3$  doped with 10% Ce NCs were synthesized colloiddally via co-precipitation method adapted from our earlier work on  $\text{LaF}_3$  doped with Ce [Sankar 2009]. The lanthanum chloride ( $\text{LaCl}_3$ , 99.999%), ammonium fluoride ( $\text{NH}_4\text{F}$ , 99.999%), ammonia in methanol solution, hydrochloric acid, and chitosan medium molecular weight were all purchased from Sigma Aldrich. Gadolinium chloride ( $\text{GdCl}_3$ , 99.999%) and cerium chloride ( $\text{CeCl}_3$ , 99.999%) were purchased from MV Laboratories.

The following balanced chemical reaction is expected to occur at the nucleation phase of  $\text{LaF}_3\text{:Gd}$  NCs:



In order to keep the reaction under argon, a three-neck borosilicate glass flask was connected to a Schlenk line gas manifold. 9 ml of 0.2M  $\text{LaCl}_3$ , 1 ml of 0.2M  $\text{GdCl}_3$ , and 10 ml of 0.6M  $\text{NH}_4\text{F}$  were added to the three-neck flask along with 25 ml of 1wt% chitosan solution at a pH of 2. The pH of the chitosan solution was modified using HCl as a way to achieve a stable mixture of  $\text{H}_2\text{O}$  and chitosan. The pH of the reaction mixture was adjusted to 6.5 using ammonia in methanol solution and was allowed to react for 2 hours at  $75^\circ\text{C}$ . After allowing the reaction solution to cool to room temperature, it was collected as is, centrifuged at 4000 rpm, and washed in 0.5% acetic acid in  $\text{H}_2\text{O}$  mixture. Afterwards, the NCs were redispersed in DI  $\text{H}_2\text{O}$  and stabilized by adding 1M HCl in  $\text{H}_2\text{O}$  solution, bringing the sample to a pH of 2.5.

The following balanced chemical reaction is expected to occur at the nucleation phase of  $\text{GdF}_3$  NCs:



10 ml of 0.2M GdCl<sub>3</sub> was reacted with 10 ml of 0.6M NH<sub>4</sub>F in this procedure. Other than that, the synthesis procedure for GdF<sub>3</sub> NCs remained the same as that described above for LaF<sub>3</sub>:Gd NCs.

The following balanced chemical reaction is expected to occur at the nucleation phase of GdF<sub>3</sub>:Ce:



9 ml of 0.2M GdCl<sub>3</sub> and 1 ml of 0.2M CeCl<sub>3</sub> were reacted with 10 ml of 0.6M NH<sub>4</sub>F in order to obtain GdF<sub>3</sub>:Ce NCs, and the synthesis continued along the lines of the previous two procedures in this section.

### **13.C. Characterization of LaF<sub>3</sub>:10%Gd<sup>3+</sup>, GdF<sub>3</sub>, and GdF<sub>3</sub>:Ce<sup>3+</sup> Nanocrystals**

#### **13.C.a. Structural Characterization of LaF<sub>3</sub>:10%Gd<sup>3+</sup>, GdF<sub>3</sub>, and GdF<sub>3</sub>:Ce<sup>3+</sup> Nanocrystals**

For structural characterization, TEM samples were prepared by placing a drop of the colloidal solution in a 200-mesh carbon coated copper grid and the solvent was allowed to dry, fixing the NCs on the grid. High-resolution transmission electron microscope, JEOL-2010F operating at 200 kV, was used with an Oxford Instruments 200 energy-dispersive spectroscopy (EDS) analytical system fitted with an Inca X-Site Ultra Thin Window EDS detector.

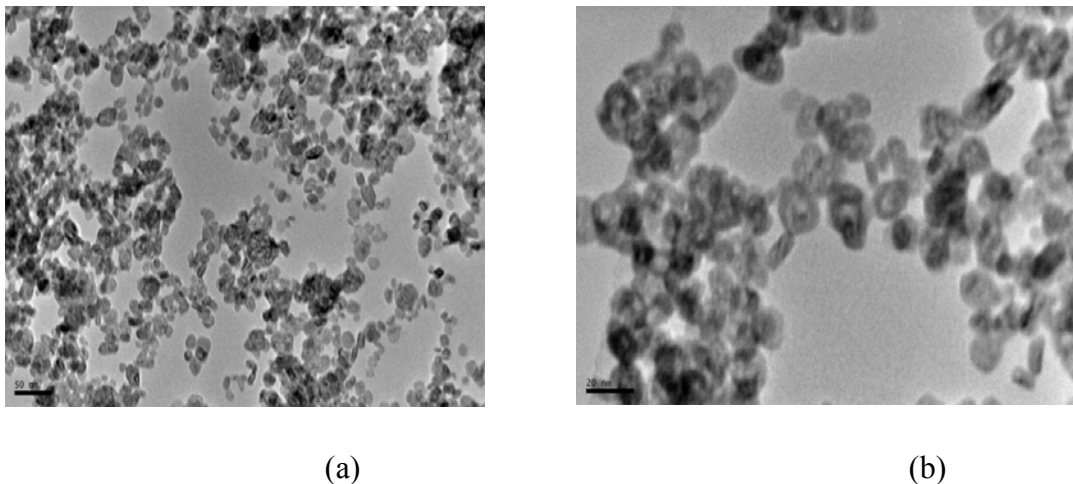


Fig. 13.1. High resolution TEM images of LaF<sub>3</sub>:10%Gd<sup>3+</sup> NCs. Scale bars: (a) 50 nm; (b) 20 nm.

High resolution images of LaF<sub>3</sub>:10%Gd<sup>3+</sup> indicate successful formation of hexagonal platelet nanoparticles (Fig. 13.1). The presence of the chitosan surfactant caused the higher magnification images to appear slightly out of focus. To get the energy dispersion spectrum (EDS) data, the electron beam was focused on a single NC and the peaks were identified using the Oxford Instruments ISIS software. Data obtained from multiple single-NC measurements showed good repeatability. The elemental presence of La, F, and Gd in the composition of the

synthesized nanoparticles was verified from the EDS spectrum shown in Fig. 13.2. The Cu and C peaks originate from the holding grid.

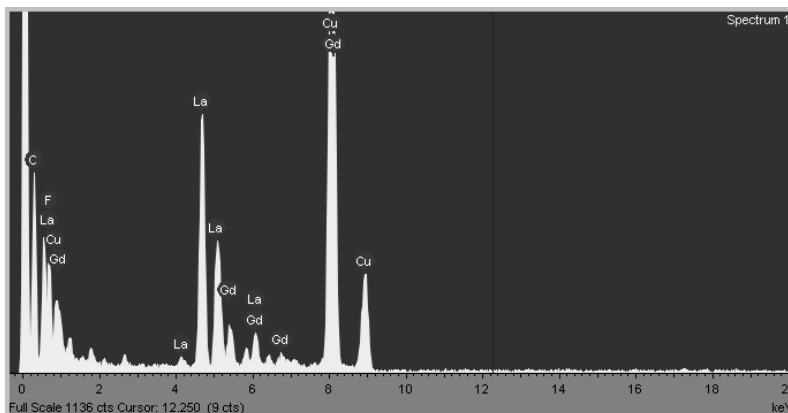


Fig. 13.2. EDS spectrum of  $\text{LaF}_3:10\%\text{Gd}^{3+}$  NCs.

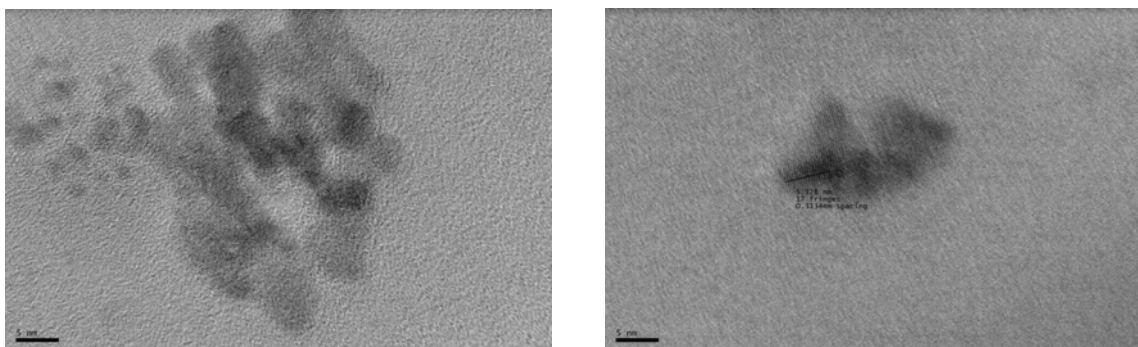


Fig. 13.3. High resolution TEM images of  $\text{GdF}_3$  NCs with 5 nm scale bars.

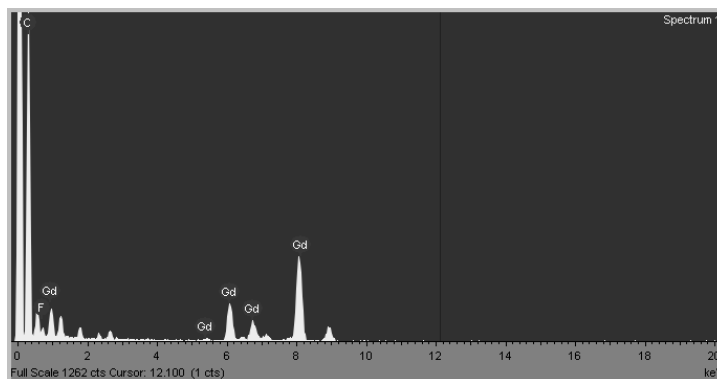


Fig. 13.4. EDS spectrum of  $\text{GdF}_3$  NCs.

Similar TEM analysis was carried out on the  $\text{GdF}_3$  NCs. Imaging of crystalline fringes in the  $\text{GdF}_3$  sample indicates successful NC formation (Fig. 13.3). The EDS spectrum shown in Fig. 13.4 confirms the elemental presence of Gd and F in the sample.

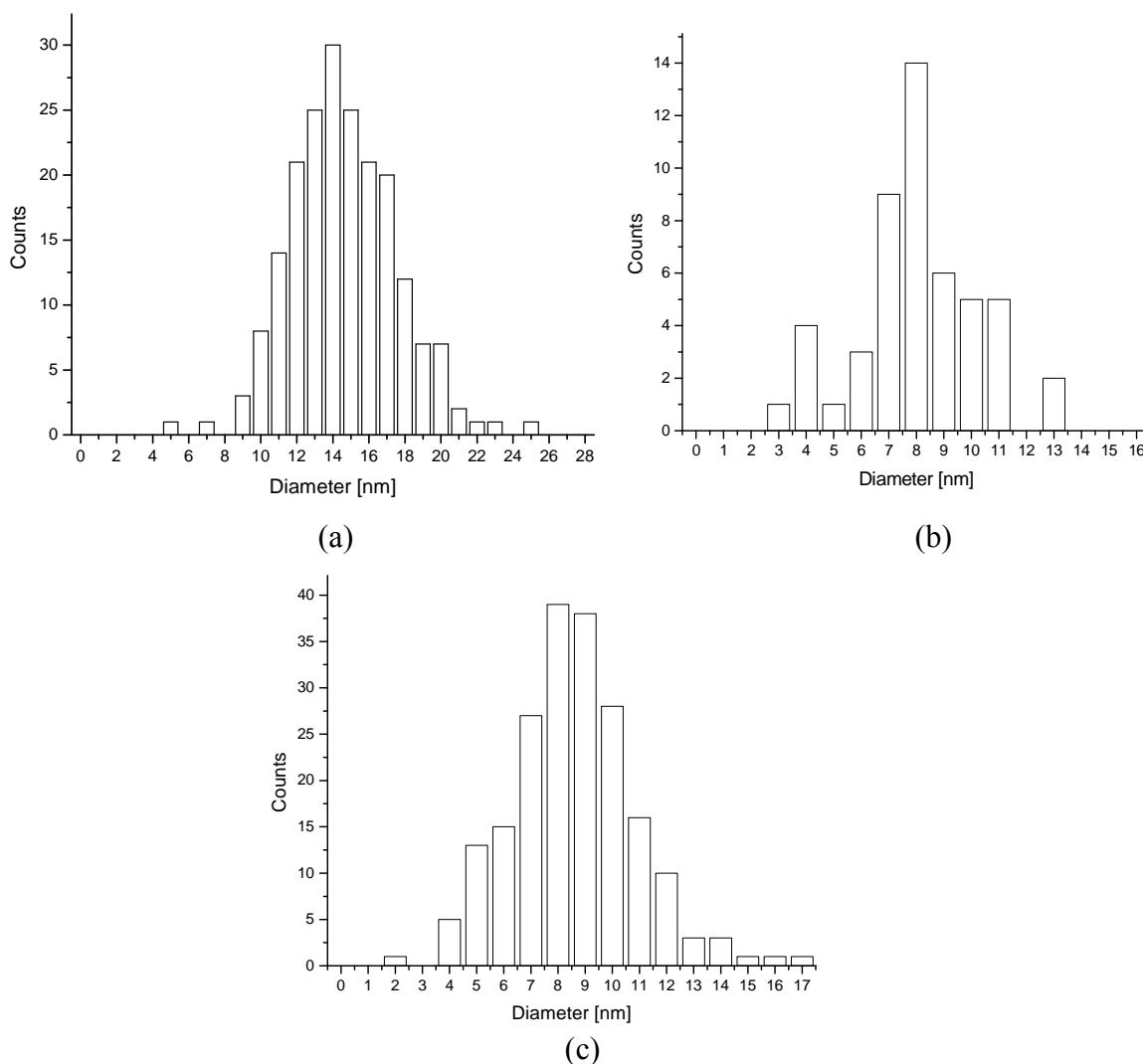


Fig. 13.5. Size distribution of (a) LaF<sub>3</sub>:10%Gd<sup>3+</sup>, (b) GdF<sub>3</sub>, and (c) GdF<sub>3</sub>:10%Ce<sup>3+</sup> NCs as obtained from DLS analysis.

The TEM analysis is known to somewhat underestimate the size of the measured crystalline objects by not properly detecting their outermost surface atomic layers. Dynamic light scattering (DLS) analysis, on the other hand, provides information about hydrodynamic size of particles, which also accounts for any ligand molecules modifying the surface of the nanoparticles. DLS measurements were taken with a DynaPro Titan dynamic light scattering module from Wyatt Technology Corporation. Fig. 13.5 shows the hydrodynamic size distributions for LaF<sub>3</sub>:10%Gd<sup>3+</sup>, GdF<sub>3</sub>, and GdF<sub>3</sub>:10%Ce<sup>3+</sup> NCs.

DLS measurements of LaF<sub>3</sub>:10%Gd<sup>3+</sup> NCs [Fig. 13.5(a)] reveal a size distribution about 10 nm wide with an average hydrodynamic size of 14 nm. In the case of GdF<sub>3</sub> NCs [Fig. 13.5(b)], DLS measurements suggest the presence of NCs with a 7 nm wide hydrodynamic size distribution with a peak diameter of 8 nm. The size distribution for GdF<sub>3</sub>:Ce<sup>3+</sup> NCs obtained from DLS analysis [Fig. 13.5(c)] is similar to that of undoped GdF<sub>3</sub> NCs.

### **13.C.b. Optical Characterization of $\text{LaF}_3:10\%\text{Gd}^{3+}$ , $\text{GdF}_3$ , and $\text{GdF}_3:\text{Ce}^{3+}$ Nanocrystals**

Absorption measurements were performed on a Varian Cary-5000-UV-VIS-NIR spectrophotometer. Corrected for their actual concentrations determined from calcination experiments, the absorption spectra for the  $\text{LaF}_3:10\%\text{Gd}^{3+}$ ,  $\text{GdF}_3$ , and  $\text{GdF}_3:10\%\text{Ce}^{3+}$  NC samples are shown in Fig. 13.6. Absorption spectrum of  $\text{GdCl}_3$  precursor is shown for comparison. Photoluminescence spectra were measured with a Horiba Jobin Yvon Fluorolog-3 spectrofluorometer. The optimal excitation wavelengths of 270 nm, 278 nm, and 260 nm for the  $\text{LaF}_3:10\%\text{Gd}^{3+}$ ,  $\text{GdF}_3$ , and  $\text{GdF}_3:10\%\text{Ce}^{3+}$  NCs were determined from PL excitation spectroscopy measurements. The PL emission spectra of Fig. 12.7 for the corresponding NCs were taken at those optimal excitation wavelengths. For the measurements, the slit widths on the excitation monochromator were set to 1 nm spectral bandwidth for all 3 samples, while the slit widths on the emission monochromator were set to 2 nm bandwidth for  $\text{LaF}_3:10\%\text{Gd}^{3+}$  and  $\text{GdF}_3:10\%\text{Ce}^{3+}$  samples, and to 3 nm bandwidth for the  $\text{GdF}_3$  NC sample.

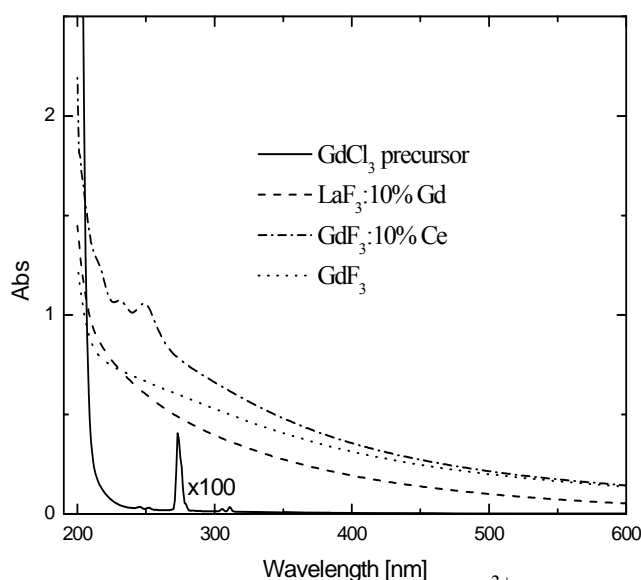


Fig. 13.6. Absorption spectra of  $\text{GdCl}_3$  precursor,  $\text{LaF}_3:\text{Gd}^{3+}$ ,  $\text{GdF}_3$ , and  $\text{GdF}_3:\text{Ce}^{3+}$  NCs corrected for their actual concentrations.

A single narrow emission line at  $\sim 311$  nm was observed in the  $\text{LaF}_3:\text{Gd}^{3+}$  NC sample, which was ascribed to emission of  $\text{Gd}^{3+}$  ions in the  $\text{LaF}_3$  matrix. The same emission line was also observed in  $\text{GdF}_3:\text{Ce}^{3+}$  NC sample along with much wider emission line centered around 350 nm. The latter was identified as emission of  $\text{Ce}^{3+}$  ions in the  $\text{GdF}_3$  host matrix. Interestingly enough, no pronounced emission peak related to  $\text{Gd}^{3+}$  ion emission was observed in the un-doped  $\text{GdF}_3$  NC sample, which suggests energy transfer between  $\text{Ce}^{3+}$  and  $\text{Gd}^{3+}$  in the  $\text{GdF}_3:\text{Ce}^{3+}$  NC sample. Similar energy transfer phenomena have been reported in [Kobayashi 2003] and [Chen 2008].

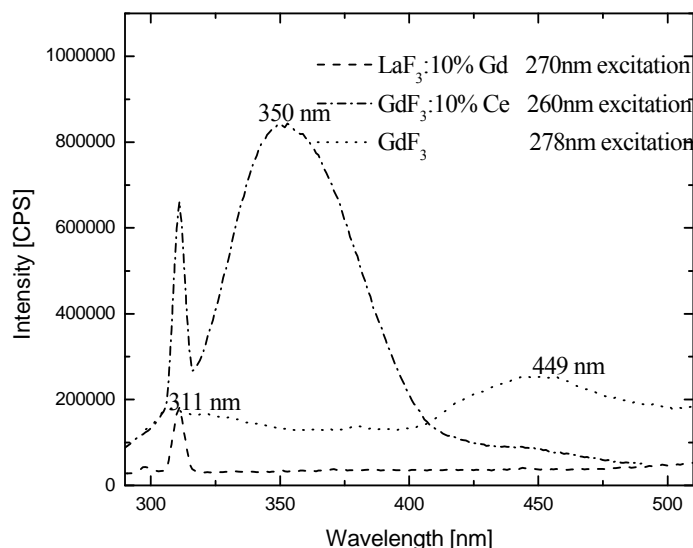


Fig. 13.7. PL emission spectra of  $\text{LaF}_3:\text{Gd}^{3+}$ ,  $\text{GdF}_3$ , and  $\text{GdF}_3:\text{Ce}^{3+}$  NCs.

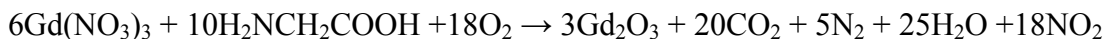
#### 14. COLLOIDAL SYNTHESIS AND CHARACTERIZATION OF Gd-CONTAINING NANOCRYSTALS FOR NEUTRON DETECTION (MODIFIED TASK 8)

In order to further explore the possibility of using Gd-containing NCs as a scintillating thermal neutron captor, we have expanded the original Task 8 into a variety of Gd-containing materials. In order to explore possible enhancement of PL emission, 2 different doping lanthanides were used, either as a single dopant or as co-dopants. The doping percentages were 0%, 10%Ce, 10%Eu, and 5%Eu,5%Ce.

##### 14.A. Colloidal Synthesis of Undoped and Doped $\text{Gd}_2\text{O}_3$ Scintillating Nanocrystals Capped with Oleic Acid

NCs of undoped  $\text{Gd}_2\text{O}_3$ ,  $\text{Gd}_2\text{O}_3$  doped with Ce, and  $\text{Gd}_2\text{O}_3$  doped with Eu were synthesized colloiddally via co-precipitation method adapted from [Söderlind 2005]. The gadolinium(III) nitrate hexahydrate  $\text{Gd}(\text{NO}_3)_3 \cdot 6\text{H}_2\text{O}$  9.999%, cerium(III) nitrate hexahydrate  $\text{Ce}(\text{NO}_3)_3 \cdot 6\text{H}_2\text{O}$  99.999%, and europium(III) nitrate hexahydrate  $\text{Eu}(\text{NO}_3)_3 \cdot 6\text{H}_2\text{O}$  99.999% were all purchased from MV Labs. The sodium hydroxide NaOH 99.999%, diethylene glycol (DEG)  $(\text{HOCH}_2\text{CH}_2)_2\text{O}$ , oleic acid  $\text{CH}_3(\text{CH}_2)_7\text{CH}=\text{CH}(\text{CH}_2)_7\text{COOH}$ , and toluene were all purchased from Sigma Aldrich.

The following balanced chemical reaction is expected to occur at the nucleation phase of  $\text{Gd}_2\text{O}_3$  NCs:



For the reaction, 2 mmol of  $\text{Gd}(\text{NO}_3)_3 \cdot 6\text{H}_2\text{O}$ , 6 mmol of NaOH, and 30 mL of DEG were added to a three-neck flask. The solution was allowed to soak at 210 °C for 30 minutes. Next, a solution of 1.6 mmol of oleic acid and 5 mL of DEG was added to the three-neck flask and the solution

was allowed to cool down to room temperature. The solution was then mixed with chloroform and cooled to below  $-11\text{ }^{\circ}\text{C}$ , and the chloroform removed with the NCs from the frozen DEG. This procedure was repeated until the chloroform no longer fluoresced under UV irradiation. Finally, the solution was distributed evenly into three centrifuge tubes and mixed with toluene. The toluene phase was collected with the NCs suspended in it. The choice of oleic acid as a surfactant was dictated by our plans of using a hydrophobic polyvinyl toluene (PVT) polymer as a host for  $\text{Gd}_2\text{O}_3$  NCs.

For the synthesis of  $\text{Gd}_2\text{O}_3$  doped with cerium and europium, the only difference was that the molar amounts of Ce or Eu precursors combined with the Gd precursor were equal to 2 mmol and were varied, depending on the desired doping percentage.

#### **14.B. Characterization of Undoped and Doped $\text{Gd}_2\text{O}_3$ Scintillating Nanocrystals Capped with Oleic Acid**

##### **14.B.a. Structural Characterization of Undoped and Doped $\text{Gd}_2\text{O}_3$ Scintillating Nanocrystals Capped with Oleic Acid**

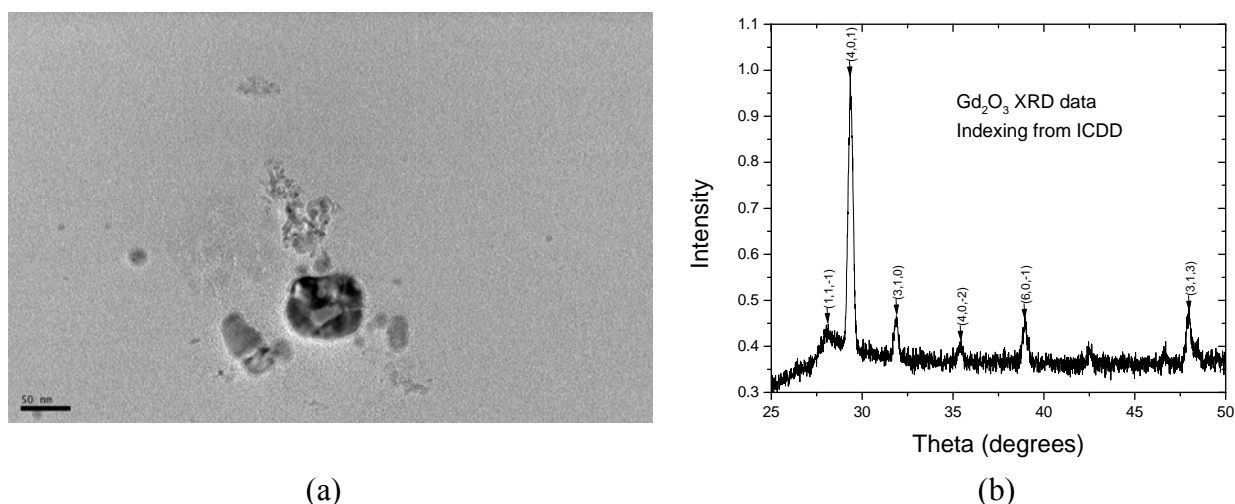


Fig. 14.1. (a) Low-resolution bright-field TEM images of  $\text{Gd}_2\text{O}_3$  NCs capped with oleic acid. Scale bar 50 nm; (b) XRD data confirming the NC crystal structure as that of  $\text{Gd}_2\text{O}_3$ .

For structural characterization, TEM samples were prepared by placing a drop of the colloidal solution onto a 200-mesh carbon coated copper grid and the solvent was allowed to dry, fixing the NCs on the grid. High-resolution transmission electron microscope, JEOL-2010F operating at 200 kV, was used with an Oxford Instruments 200 energy-dispersive spectroscopy (EDS) analytical system fitted with an Inca X-Site Ultra Thin Window EDS detector.

Low-resolution TEM images of undoped  $\text{Gd}_2\text{O}_3$  NCs show platelets that seem to agglomerate (Fig. 14.1a). Similar TEM analysis was carried out on the  $\text{Gd}_2\text{O}_3\text{:Ce}$  (Fig. 14.2) and  $\text{Gd}_2\text{O}_3\text{:Eu}$  (Fig. 14.3) NCs. The TEM image in Fig. 14.2a reveal an irregular spherical shape of the NCs. Fig. 14.2b shows a dark field image that confirms crystallinity of the NC sample. The EDS data

in Fig. 14.4 further confirm the expected elemental composition of the NCs. Fig. 14.1b shows the XRD data from a sample of  $\text{Gd}_2\text{O}_3$  NCs dried onto a zero background holder, taken with a Rigaku SmartLab system. As expected, the experimental results matched very well with the ICDD data for  $\text{Gd}_2\text{O}_3$ .

The TEM analysis is known to somewhat underestimate the size of the measured crystalline objects by not properly detecting their outermost surface atomic layers. Dynamic light scattering (DLS) analysis, on the other hand, provides information about hydrodynamic size of particles, which also accounts for any ligand molecules modifying the surface of the nanoparticles. DLS measurements were taken with a DynaPro Titan dynamic light scattering module from Wyatt Technology Corporation. Fig. 14.5 shows the hydrodynamic size distributions for  $\text{Gd}_2\text{O}_3$ ,  $\text{Gd}_2\text{O}_3$ :10%Ce,  $\text{Gd}_2\text{O}_3$ :10%Eu, and  $\text{Gd}_2\text{O}_3$ :5%Ce,5%Eu NCs.

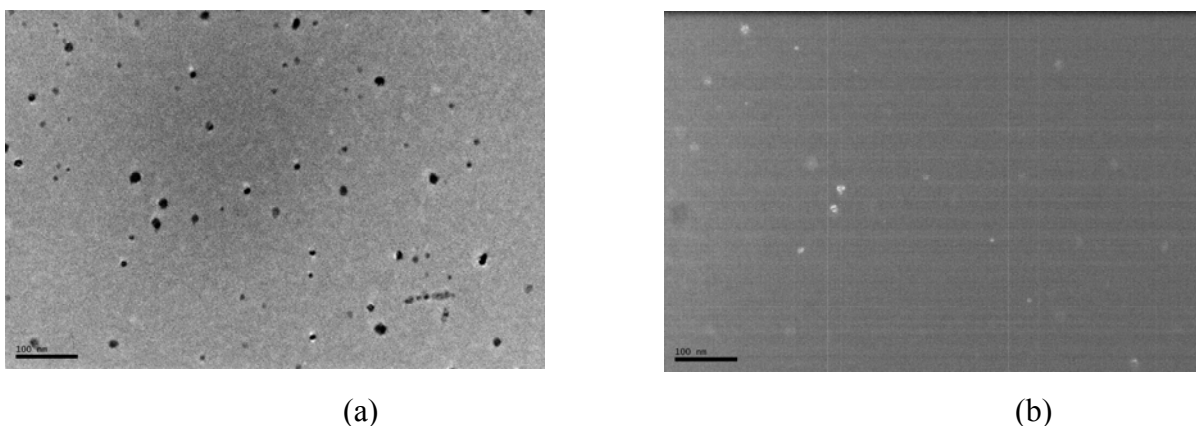


Fig. 14.2. Bright-field TEM image (a) and dark field TEM image (b) of  $\text{Gd}_2\text{O}_3$ :10%Ce NCs capped with oleic acid. Scale bar 100 nm.

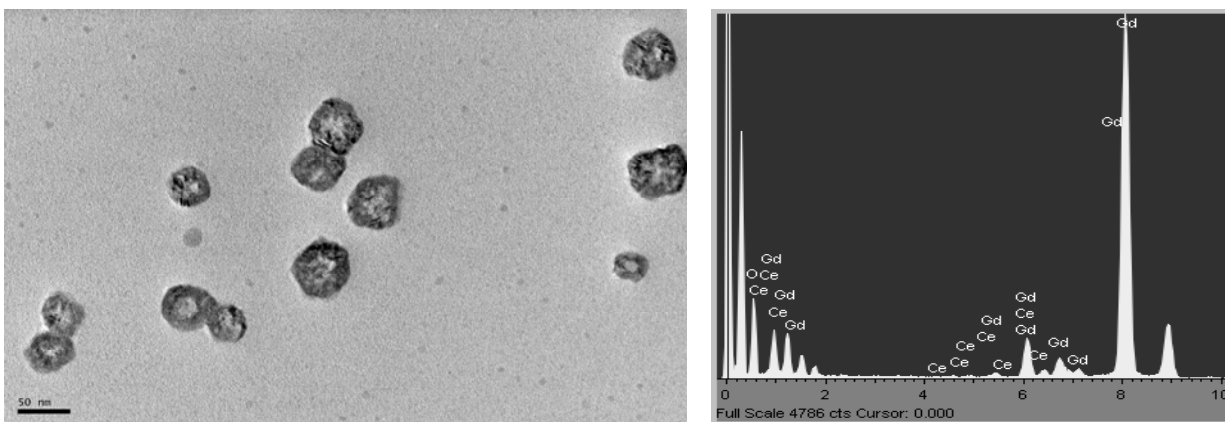


Fig. 14.3. Low-resolution bright-field TEM images of  $\text{Gd}_2\text{O}_3$ :10%Eu NCs capped with oleic acid. Scale bar 50 nm.

Fig. 14.4. EDS data for  $\text{Gd}_2\text{O}_3$ :10%Ce NCs.

DLS measurements of  $\text{Gd}_2\text{O}_3$  NCs [Fig. 14.5(a)] reveal a size distribution with a standard deviation of 2.33 nm and with an average hydrodynamic size of 5.70 nm. In the case of



Gd<sub>2</sub>O<sub>3</sub>:10%Ce NCs [Fig. 14.5(b)], DLS measurements suggest the presence of NCs with a 1.23 nm standard deviation and with an average diameter of 2.73 nm. The DLS size distribution measurements for Gd<sub>2</sub>O<sub>3</sub>:10%Eu suggest the presence of NCs with a 2.37 nm standard deviation and with an average diameter of 13.6 nm [Fig. 14.5(c)]. The Gd<sub>2</sub>O<sub>3</sub>:5%Ce,5%Eu NCs appear to have a standard deviation of 1.48 nm and an average diameter of 7.61 nm [Fig. 14.5(d)].

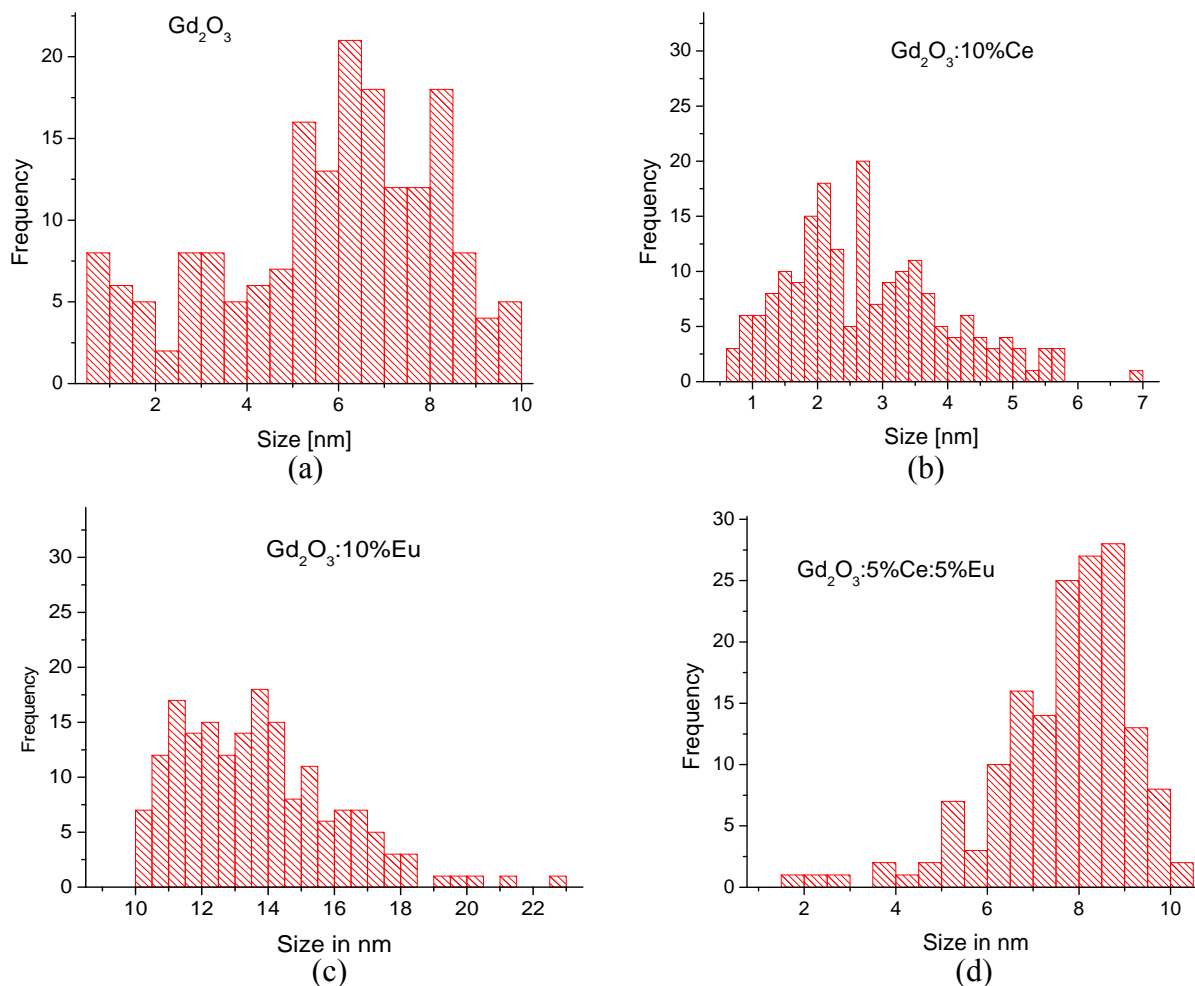


Fig. 14.5. Hydrodynamic size distribution of (a) Gd<sub>2</sub>O<sub>3</sub>, (b) Gd<sub>2</sub>O<sub>3</sub>:10%Ce, (c) Gd<sub>2</sub>O<sub>3</sub>:10%Eu, and (d) Gd<sub>2</sub>O<sub>3</sub>:5%Ce,5%Eu NCs as obtained from DLS analysis.

#### **14.B.b. Optical Characterization of Undoped and Doped Gd<sub>2</sub>O<sub>3</sub> Scintillating Nanocrystals Capped with Oleic Acid**

Absorption measurements were performed on a Varian Cary-5000-UV-VIS-NIR spectrophotometer. The absorption spectra for the Gd<sub>2</sub>O<sub>3</sub>, Gd<sub>2</sub>O<sub>3</sub>:10%Ce, Gd<sub>2</sub>O<sub>3</sub>:10%Eu, and Gd<sub>2</sub>O<sub>3</sub>:5%Ce,5%Eu NC samples are shown in Fig. 14.6.

PL spectra were measured with a Horiba Jobin Yvon Fluorolog-3 spectrofluorometer, with the excitation and emission monochromator slits set for 3 nm spectral widths. The optimal wavelengths for excitation of the NC samples were determined from PL excitation spectroscopy

measurements, and the PL emission spectra of Fig. 14.7 for the corresponding NCs were taken at those optimal excitation wavelengths.

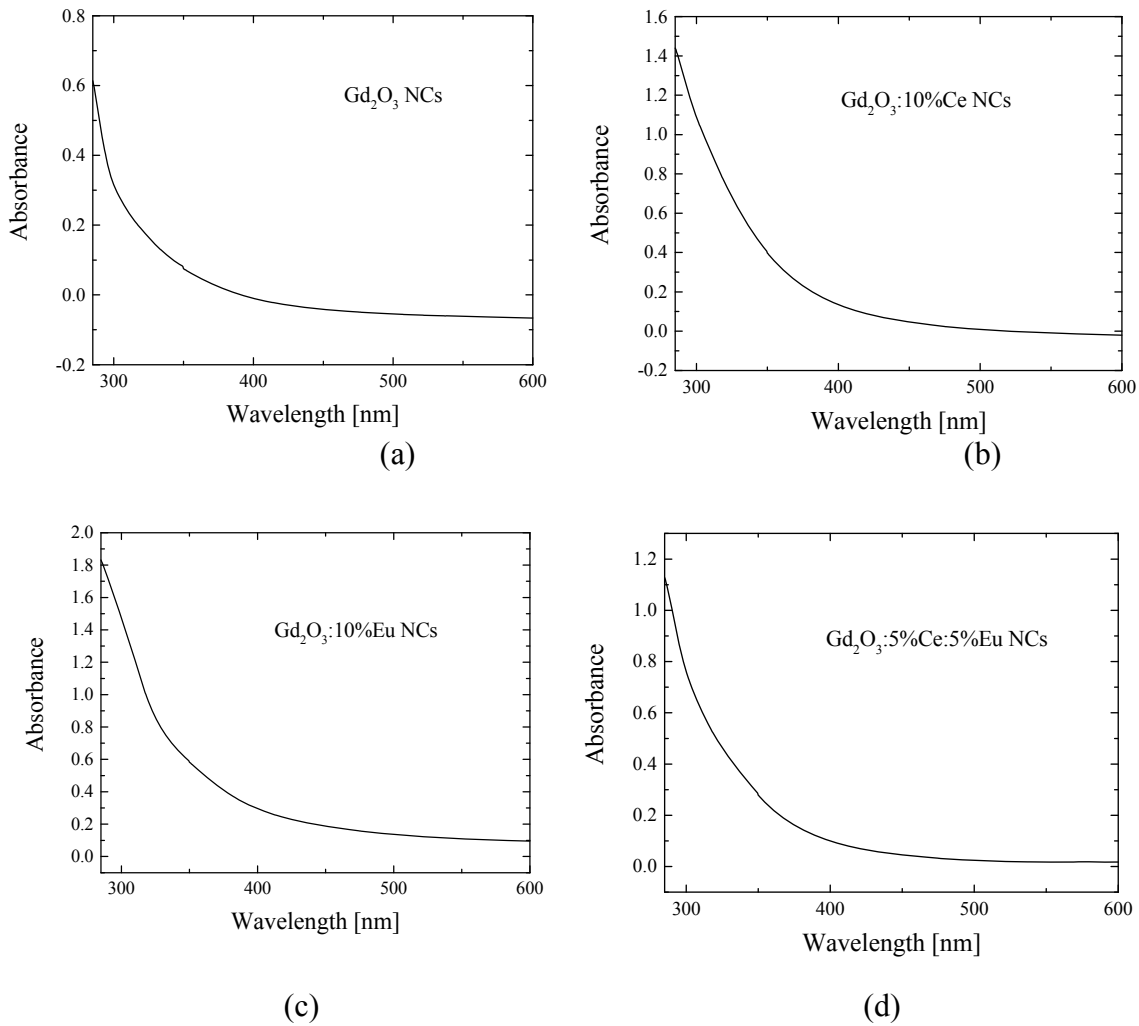


Fig. 14.6. Absorption spectra of (a)  $\text{Gd}_2\text{O}_3$ , (b)  $\text{Gd}_2\text{O}_3:10\%\text{Ce}$ , (c)  $\text{Gd}_2\text{O}_3:10\%\text{Eu}$ , and (d)  $\text{Gd}_2\text{O}_3:5\%\text{Ce},5\%\text{Eu}$  NCs.

Fluorescence lifetime measurements performed using the same tool yielded a three-component fit, with similar results for all 4 types of samples indicating a very fast response time (see Fig. 14.8). For example, for  $\text{Gd}_2\text{O}_3:10\%\text{Ce}$ , the three lifetime components were 0.79 ns with 48.11% weight, 2.87 ns with 41.38% weight, and 8.09 ns with 10.51% weight.

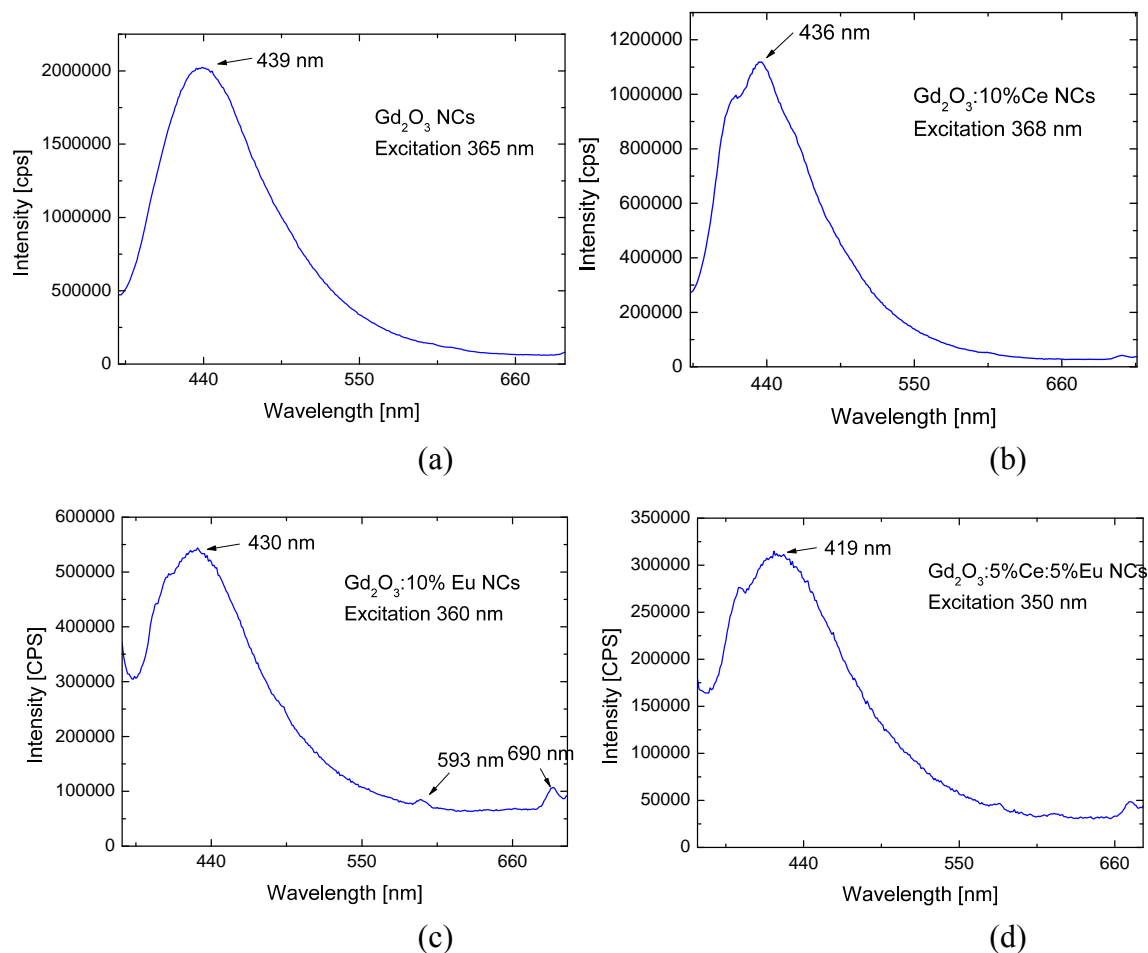
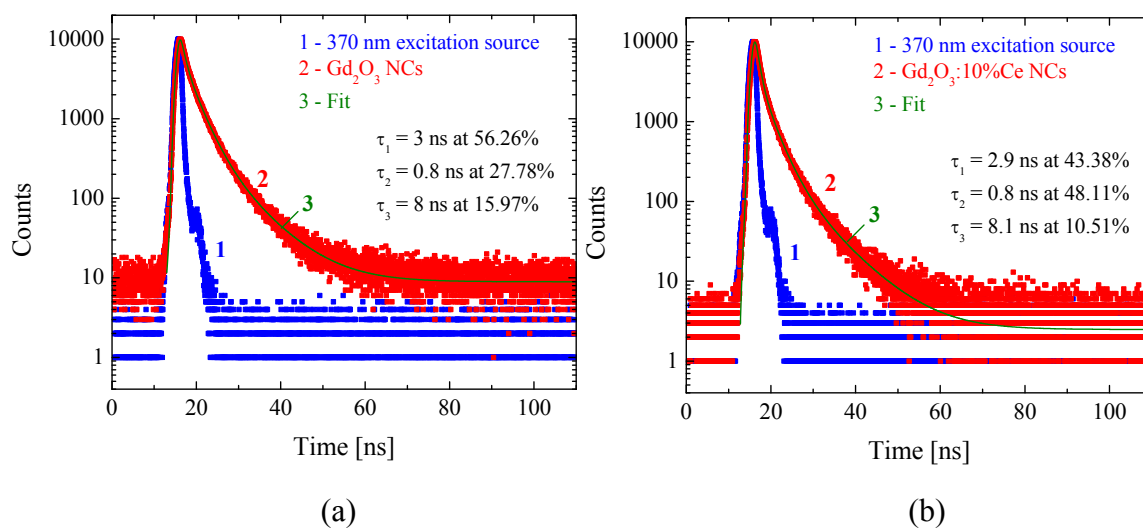


Fig. 14.7. PL emission spectra of (a)  $\text{Gd}_2\text{O}_3$ , (b)  $\text{Gd}_2\text{O}_3:10\%\text{Ce}$ , (c)  $\text{Gd}_2\text{O}_3:10\%\text{Eu}$ , and (d)  $\text{Gd}_2\text{O}_3:5\%\text{Ce},5\%\text{Eu}$  NCs.



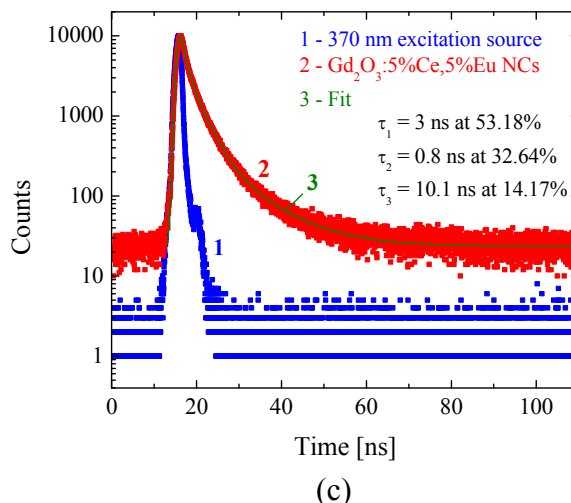


Fig. 14.8. Results of PL lifetime measurements for (a)  $\text{Gd}_2\text{O}_3$ , (b)  $\text{Gd}_2\text{O}_3:10\%\text{Ce}$ , and (c)  $\text{Gd}_2\text{O}_3:5\%\text{Ce}:5\%\text{Eu}$  NCs.

#### **14.C. NANOCOMPOSITE PVT LOADED WITH $\text{Gd}_2\text{O}_3:10\%\text{Ce}$ NANOCRYSTALS**

##### **14.C.a. Loading Gadolinium Oxide Nanocrystals into Poly(Vinyl Toluene)**

For the purpose of making a nanocomposite, the solution of  $\text{Gd}_2\text{O}_3:10\%\text{Ce}$  described in Section 14.A., rather than being mixed with toluene, was dried to a powder at 245 °C to remove any remaining DEG, and the powder was weighed. Prior to synthesis, vinyl toluene (VT) monomer was passed through a distillation column to remove an inhibitor that was put into the VT by the manufacturer in order to prevent polymerization during shipping and storage. Pre-weighed NCs were added to the monomer solution. Under inert atmosphere, an azobisisobutyronitrile (AIBN) initiator was added, and polymerization was set by heating the sample in an oven at 90 °C for 24 hours. Periodic sonication was used to remove bubbles. The nanocomposite was obtained as a homogeneous mixture due to colloidal stability of the NCs coated with oleic acid, which has been verified by machining the polymer and checking whether the photoluminescence remained stable. Visual inspection revealed a considerable difference in appearance of a plain PVT sample and a sample of PVT loaded with  $\text{Gd}_2\text{O}_3:10\%\text{Ce}$  NCs. Under room light, the nanocomposite sample appeared opaque, while the plain PVT sample was transparent. Under UV excitation, bright blue luminescence due to oleic acid surfactant was observed from the nanocomposite, while the plain PVT remained dark. The obtained nanocomposite was used in neutron detection experiments.

##### **14.C.b. Optical Characterization of Gadolinium Oxide NCs Loaded into Poly(Vinyl Toluene)**

PL spectra of  $\text{Gd}_2\text{O}_3:10\%\text{Ce}$  NCs suspended in toluene, PVT loaded with  $\text{Gd}_2\text{O}_3:10\%\text{Ce}$  NCs, and plain PVT, all taken at 250 nm excitation wavelength, are shown in Fig. 14.9. A rather broad 285-nm Ce emission line was observed from  $\text{Gd}_2\text{O}_3:10\%\text{Ce}$  NCs suspended in toluene. With very strong competition from PVT for the 250-nm excitation light, the Ce emission was not

observed in PVT loaded with  $\text{Gd}_2\text{O}_3:10\%\text{Ce}$  NCs; instead, the PL emission was dominated by the 313 nm emission from PVT.

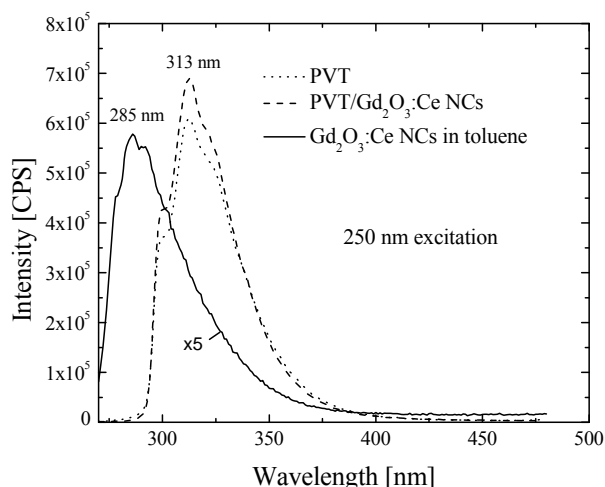


Fig. 14.9. Photoluminescence spectra of  $\text{Gd}_2\text{O}_3:10\%\text{Ce}$  NCs suspended in toluene (magnified 5 times for better visibility), PVT loaded with  $\text{Gd}_2\text{O}_3:10\%\text{Ce}$  NCs, and plain PVT.

## 15. NUMERICAL SIMULATION OF NEUTRON DETECTION IN NANOCRYSTALS (TASK 9)

### 15.A. MCNPX Simulations of $\text{Gd}_2\text{O}_3$ Response to $^{252}\text{Cf}$

In order to theoretically predict the neutron detection sensitivity of  $\text{Gd}_2\text{O}_3$  NCs, Monte Carlo N-particle extended (MCNPX) simulations were carried out. The experimental setup used in irradiation experiments (Figs. 15.1 and 16.4) was modeled using the MCNPX 2.6.0 code. MCNPX<sup>TM</sup> was developed by combining the capabilities of LAHET<sup>TM</sup> and MCNP<sup>TM</sup> into a single code [Pelowitz 2008]. This major extension of MCNP capabilities includes tracking of all particles at all energies and allows for the use of physics models in the code to compute interaction probabilities, whenever table-based data are not available.

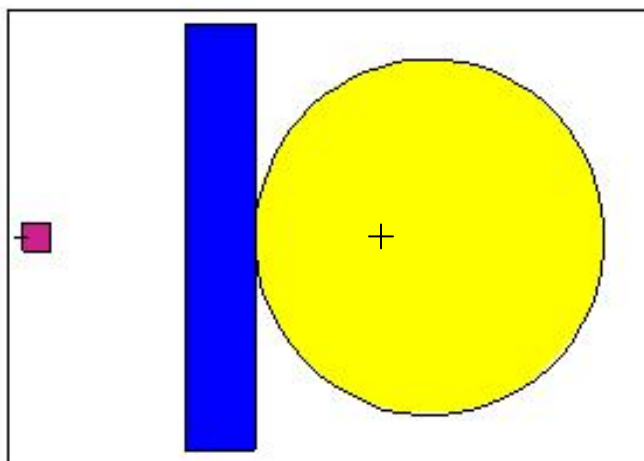


Fig. 15.1. The setup geometry from left to right: polyethylene sphere, borated polyethylene board, and cuvette.

The gamma source model featured a monoenergetic energy point source in the center of the polyethylene sphere, as in the experimental setup described in Section 16.C. The cross in Fig. 15.1 indicates the position of the source. The borated polyethylene boards, described in Section 16.C, were also accounted for. No structural support for the cuvette containing the NC solution was included in the model. Normal atmosphere surrounded all the components. The modeling included propagation in all 3 spatial dimensions. The gamma flux crossing from the cuvette into the PM tube located behind it was tallied in a 9.3-mm-radius circular area located behind the cuvette, representing the entrance window of the PMT used in actual experiments of Section 16.

The gamma source energies used for the runs were in the 1-10 MeV range. While the primary gammas from spontaneous fission of  $^{252}\text{Cf}$  are under 1 MeV [Bowman 1964], there are higher-energy gammas from the relaxation of the daughter nuclei. As these higher energy photons are more likely to be confused with the multi-MeV gammas from neutron absorption by  $^{157}\text{Gd}$ , the higher energies were run to try to capture the potential signal distortion. The neutron energy distribution from spontaneous fission of  $^{252}\text{Cf}$  is modeled by a two-parameter Maxwell's distribution, known as a Watt's fission spectrum [Shultis 2007]:

$$W(a,b,E) = C \exp(-E/a) \sinh[(bE)^{1/2}] , \quad (15.1)$$

where the normalization constant  $C$  is given by

$$C = 2(\pi ab)^{-1/2} \exp(-ab/4)/a . \quad (15.2)$$

The values of coefficients  $a$ ,  $b$ , and  $C$  for  $^{252}\text{Cf}$  are  $a = 1.025 \text{ MeV}$ ,  $b = 2.926 \text{ MeV}^{-1}$ , and  $C = 0.30033 \text{ MeV}^{-1}$  [Miri Hakimabad 2007]. Calculated Watt's fission spectrum for  $^{252}\text{Cf}$  is shown in Fig. 15.2. While the peak energy is slightly less than 1 MeV, the average actually comes out closer to 2 MeV. Therefore, a monoenergetic 2 MeV neutron source was used in simulations.

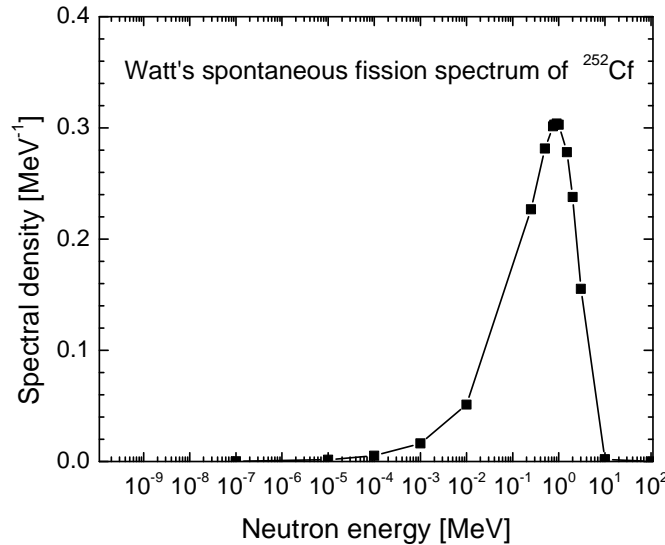
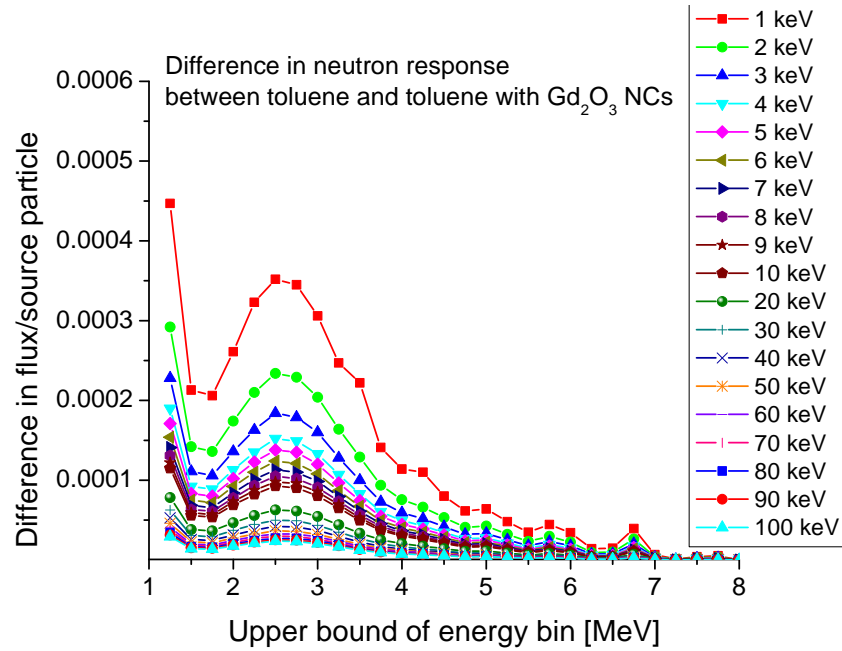
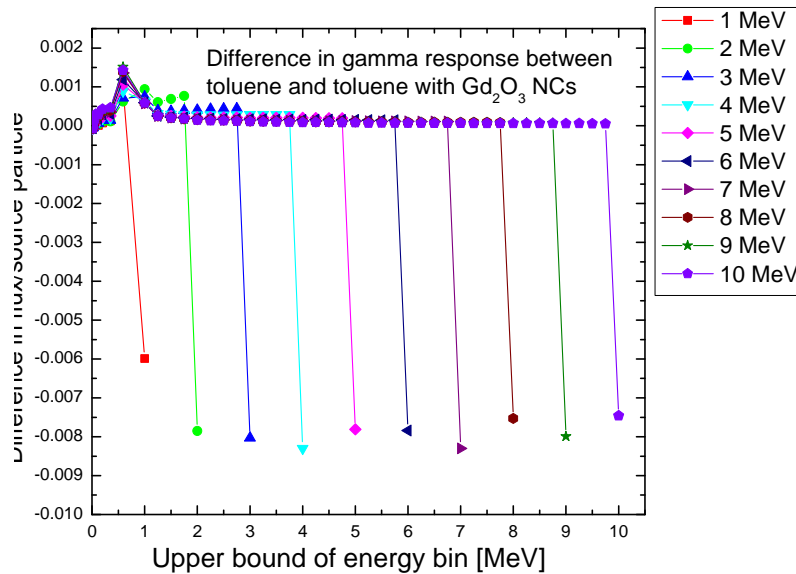


Fig. 15.2. Simulated  $^{252}\text{Cf}$  neutron energy spectrum.



(a)



(b)

Fig. 15.3. Difference in response between toluene-based  $\text{Gd}_2\text{O}_3$  NC solution and pure toluene obtained for (a) slowed down neutrons with energies ranging from 1 keV to 100 keV, and (b) gamma source with photon energies ranging from 1 MeV to 10 MeV.

A monoenergetic 2-MeV neutron source, approximating a  $^{252}\text{Cf}$  source, was then run in geometry of Fig. 15.1 to find the energy range of neutrons impinging on the  $\text{Gd}_2\text{O}_3$ -based NC solution. It was determined that the polyethylene sphere and borated polyethylene sheets were not fully thermalizing the neutrons. Based on these results, we changed the geometry of the simulation by placing a monoenergetic neutron source with energies ranging from 1-100 keV right in front of the cuvette, to avoid energy spreading. For gamma calculations, the gamma

source was still positioned in the center of the polyethylene sphere, as shown in Fig. 15.1. Simulations were run for the NCs dispersed in toluene and for pure toluene samples for comparison. Note that while the gamma irradiation only produces photons up to the energy of the incident gamma ray, transfer of the neutron binding energy to the photons emitted in the neutron capture process results in production of multi-MeV photons even with thermal neutrons.

Fig. 15.3 contains the MCNPX simulation results for the response difference between toluene-based  $\text{Gd}_2\text{O}_3$  NC solutions and pure toluene obtained for (a) slowed down neutrons with energies ranging from 1 keV to 100 keV, and (b) a gamma source with photon energies ranging from 1 MeV to 10 MeV. When reading Fig. 15.3, it is important to realize that the fluxes graphed have been normalized by the number of source particles run. The statistical nature of MCNPX means that even when identical decks are run for identical times, different numbers of particles will be run. If the runs are long enough, this should be a negligible difference. However, when different energies or different particles are run, this is not the case. For example, the gamma simulation in Fig. 15.3(b) varied from ~10 million for 10 MeV photons to ~40 million for 1 MeV photons in 10 hr runs. The number of neutrons in Fig. 15.3(a) varied from ~911 million for 1 keV neutrons to ~1.705 billion for 100 keV neutron during similar 10 hr runs. Normalizing the fluxes in this form makes it easier to compare different runs, and it also makes comparison with other potential detection materials easier. Essentially, the normalized flux is the detection efficiency of the material.

As expected, based on the high thermal neutron absorption cross-section of Gd, the NCs in toluene outperformed pure toluene for neutron detection [Fig. 15.3(a)]. The lower the energy of the neutron source, the better the observed improvement in performance. It is interesting to compare Fig. 15.3(a) with Fig. 16.8, in which it can be noticed that the actual measurements using pure toluene and toluene with NCs result in similar spectral envelopes in MCA. The difference between the measured spectra from pure toluene and toluene with NCs would show a remarkably similar shape to that of Fig 15.3(a). Given that the flux profile is similar across the tested neutron energies, it would be logical to expect that the same shape should be seen with and without the borated boards present. The energy spectrum recorded on MCA, assuming no large distortion from the intervening electronics, should simply be a linear combination of the spectra given by the MCNPX simulation, weighted by the energy spectrum of the source. The fact that similar shaping is indeed observed in the MCA results likely indicates a minimal distortion from the electronics, as well as a low flux. Higher flux rates would lead to photons from multiple events registering in the same time bin, which would distort the pulse shape.

While Fig. 15.3(a) shows what could be expected for low flux rates from a pure neutron source, we need to take into account the fact that  $^{252}\text{Cf}$  produces gamma rays as well. When gamma source simulation was run [Fig. 15.3(b)], pure toluene and toluene with NCs performed very similarly. The difference between the photon flux from pure toluene and toluene with NCs in Fig. 15.3(b) is for the most part zero. There are two exceptions to this; the first is the source energy for each run, the second is the lower energy bins. As the source energy signal for each run is much higher in pure toluene and there are more low energy photons in presence of NCs, it can be concluded that more gamma interactions are occurring with the NCs, leading to more down-scattered photons. Conversely, that also means that there is a higher uncollided flux in pure toluene. Future work with non-monoenergetic sources to determine if the difference in



uncollided gamma flux can be used for distinguishing between gamma and neutron radiation could prove valuable.

## 16. DEMONSTRATION OF NANOCRYSTALLINE DETECTORS OF NEUTRON RADIATION (TASK 10)

Thermal neutrons captured by Gd atoms result in emission of gamma and X-ray radiation. Therefore, gamma ray detection techniques similar to those described in Section 10 have been adopted for thermal neutron detection using Gd-containing NCs.

### 16.A. Scintillation Event Measurement Setup

For both the  $\gamma$ -ray and neutron detection experiments, the same amplification and pulse shaping system was used to record scintillation events. A schematic of the scintillation detections system is shown in Fig. 16.1. Light was collected with a Hamamatsu R7449 bi-alkali PMT, with a quartz front window providing sensitivity up to 185 nm in the deep ultraviolet. A Hamamatsu C90280-01 socket assembly accommodated both high voltage supply that could be adjusted from 0 to 1,250 V and resistance ladder for the dynodes in the PMT. The data from the PMT collected during experiments were analyzed using Maestro-32 Ortec pulse height discriminator for  $\gamma$ -ray spectroscopy.

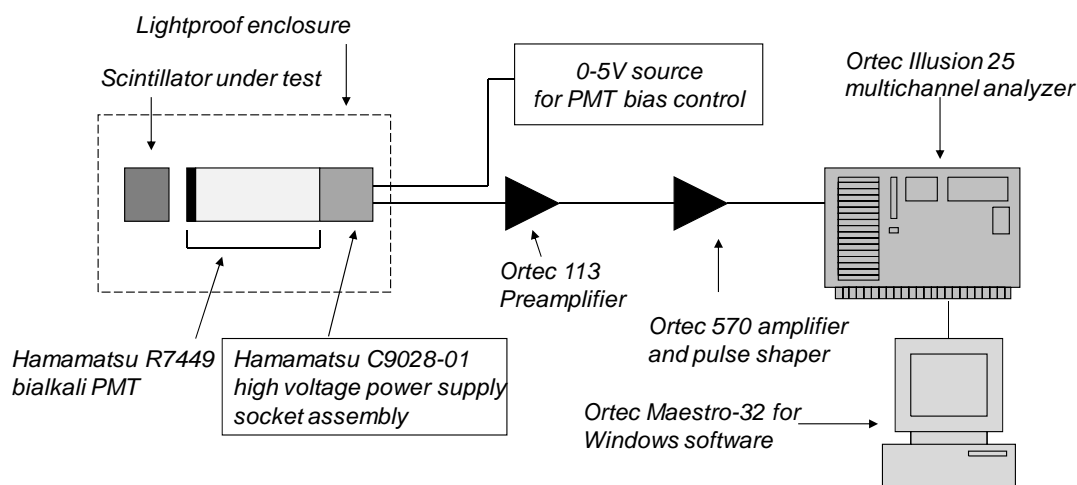


Fig. 16.1. Block diagram of amplification and pulse shaping system.

The hardware included an Ortec 113 transimpedance pre-amplifier, an Ortec 570 amplifier with RC-CR pulse shaping and an MCA emulator with TRUMP-PCI card for multichannel pulse-height analysis. All measurements were taken for 1,000 s of live time. In order to allow the multichannel analyzer to accurately measure the peak height, all tests were performed with the RC time constants of the differentiating and integrating networks set to 1  $\mu$ s. The pulses were amplified 200 times (V/V), which provided sufficient resolution to detect a single-photon peak.

### 16.B. Gamma-Ray Detection Experiments

The scintillation materials under test were contained in a cylindrical quartz cuvette [Fig. 16.2(a)] with a path length of 20 mm between two polished windows and an inner diameter of 19 mm, containing approximately 5.6 ml of fluid. The rear window and curved surfaces of the cuvette were covered with Teflon tape to reflect scintillation light into the PMT. Optical grease was used to reduce reflection between the cuvette and the PMT, and the cuvette was held in place with a lens holder.

At the time of measurement, a 0.768  $\mu\text{Ci}$  (28,400 Bq) 3 mm-radius  $^{57}\text{Co}$  disc source [Fig. 16.2(b)] was placed 6 mm behind the rear wall of the cuvette for a total distance of 18.75 mm between the radioactive source and the mid-plane of the scintillation fluid. In order to calculate the solid angle  $\Omega$  for the mid-plane of the fluid sample under test, we used an approximate solution of the following integral:

$$\Omega = \frac{4\pi a}{s} \int_0^\infty \frac{\exp(-Lk) J_1(sk) J_1(ak)}{k} dk, \quad (16.1)$$

given in [Knoll 2000], where  $s$  is the radius of a disc source,  $a$  is the radius of the scintillation cuvette,  $s$  is the source radius,  $L$  is the distance between the source and the mid-plane of the cuvette, and  $J_1(x)$  is the Bessel function of  $x$ . The numerical approximation used provided a value of 4.84 sr, which resulted in a flux of 3,800  $\gamma\text{-ray}/\text{cm}^2\text{s}$  at the mid-plane of the scintillation fluid sample under test.



Fig. 16.2. (a) Scintillation test cuvette with 1" NaI test crystal, and (b)  $^{57}\text{Co}$  source.

For the  $\gamma$ -ray detection experiments, the bias voltage on the PMT was set to 910 V, and each 1,000-s live time measurement was repeated 2-3 times to provide standard deviation error bars. The results, shown in Fig. 15.3, are represented as counts above background, with the results of background measurement subtracted from the results in presence of the  $^{57}\text{Co}$  gamma source. The error bars are the geometric sum of the background measurement error and the measurement error under  $^{57}\text{Co}$  irradiation.

Contrary to what was expected, all of the Gd-containing nanocrystalline samples showed less response than the control sample of 2 mg/ml chitosan solution. Our current hypothesis is that

these low count levels are due to high self-absorption in UV region in the NC samples, as evidenced by the absorption spectra in Fig. 13.6. Further work will be devoted to identifying the reasons for enhanced absorption and lowering the absorption level.

Fig. 16.3. Gamma ray detection results.

#### **16.C. Thermal Neutron Detection Experiments with Gd-Containing $\text{LnF}_3$ Nanocrystals**

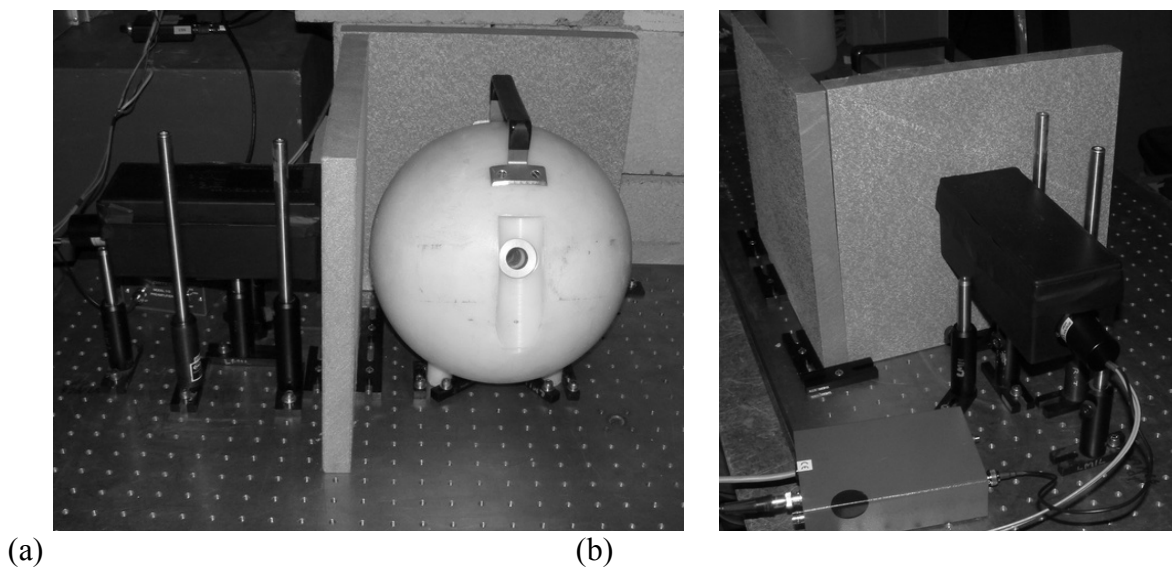


Fig. 16.4. Experimental setup for neutron detection showing (a) moderating polyethylene sphere, and (b) PMT in a light-proof enclosure.

For thermal neutron detection experiments with lanthanide fluoride NCs containing Gd, a 2.29 mCi  $^{252}\text{Cf}$  source was used, generating approximately  $8.45 \times 10^7$  neutrons/s at varying kinetic energies. The source was placed in a 10"-diameter polyethylene sphere used as a moderator, providing a thermal neutron source. Two 1'x1'x1" pieces of 5% borated polyethylene were used

to provide neutron shielding, one piece to lower the neutron dose received by the electronics, and a second removable piece to attenuate neutron flux (but not gamma rays) received by the scintillator. The sphere and borated polyethylene slabs were mounted on an optical table as shown in Fig. 16.4(a).

The PMT was repackaged into a smaller light-proof enclosure in order for us to be able to move the PMT and scintillator under test away from the powerful  $^{252}\text{Cf}$  source for loading a different scintillation material. The rods seen in Fig. 16.4(b) provide a custom kinematic mount allowing the PMT to be returned in exactly the same position each time, to maintain the geometry of the experiment.

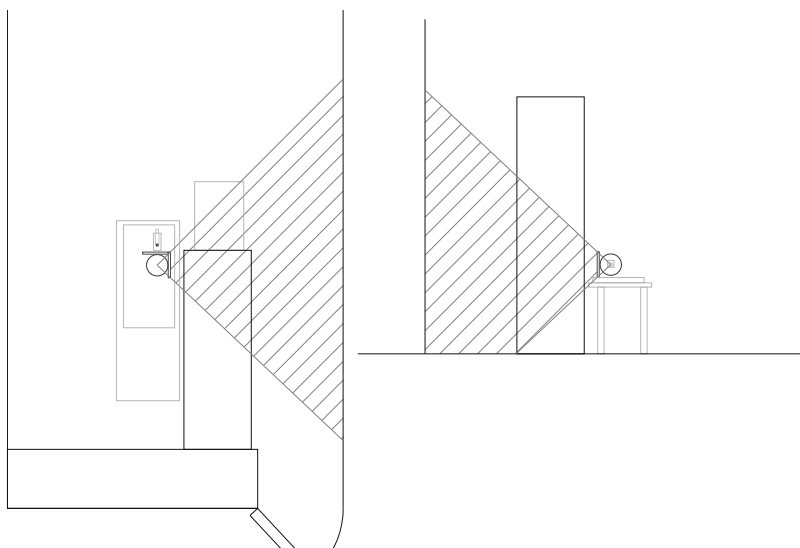


Fig. 16.5. Computer aided design drawing showing area of neutron shielding for experimental setup: top view (on the left) and side view (on the right).

The strong neutron source provided  $\sim 35$  mrem/hr dose rate for neutrons and  $\sim 3$  mrem/hr dose rate for gamma rays at 30 cm distance, and precautions were taken to protect personnel and equipment. When a sheet of borated polyethylene was placed between the source and the detector, the measured neutron dose rate dropped from initial 35 mrem/hr to 7 mrem/hr, attenuating approximately 80% of the neutron flux. In a rough geometry study of the experimental area, neglecting neutron diffusion, we determined the size of the neutron shielding area that the borated polyethylene would provide (shown as the hatched area in Fig. 16.5), and the electronic instrumentation was placed in that area. To minimize dose to the operators, the room was abandoned during the experiment.

Since the neutron source was significantly farther away from the cuvette containing the scintillating NCs, 239 mm vs. 18.75 mm as compared to the gamma response experiments, the point source approximation was used for calculating neutron flux. The calculated solid angle of 0.00496 sr resulted in a neutron flux of  $\sim 11800$  neutrons/cm<sup>2</sup>-s.

Three sets of measurements were taken for each of the three Gd-containing NC materials and the control sample of 2 mg/ml chitosan solution. First, a background measurement was taken with

the neutron source removed from the experimental setup. In the second measurement, the neutron source was blocked with a sheet of the borated polyethelene placed between the source and NC scintillating material, and in the final measurement there was no neutron block between the source and NC scintillating material under test. The background-subtracted results of these experiments are shown in Fig. 16.6.

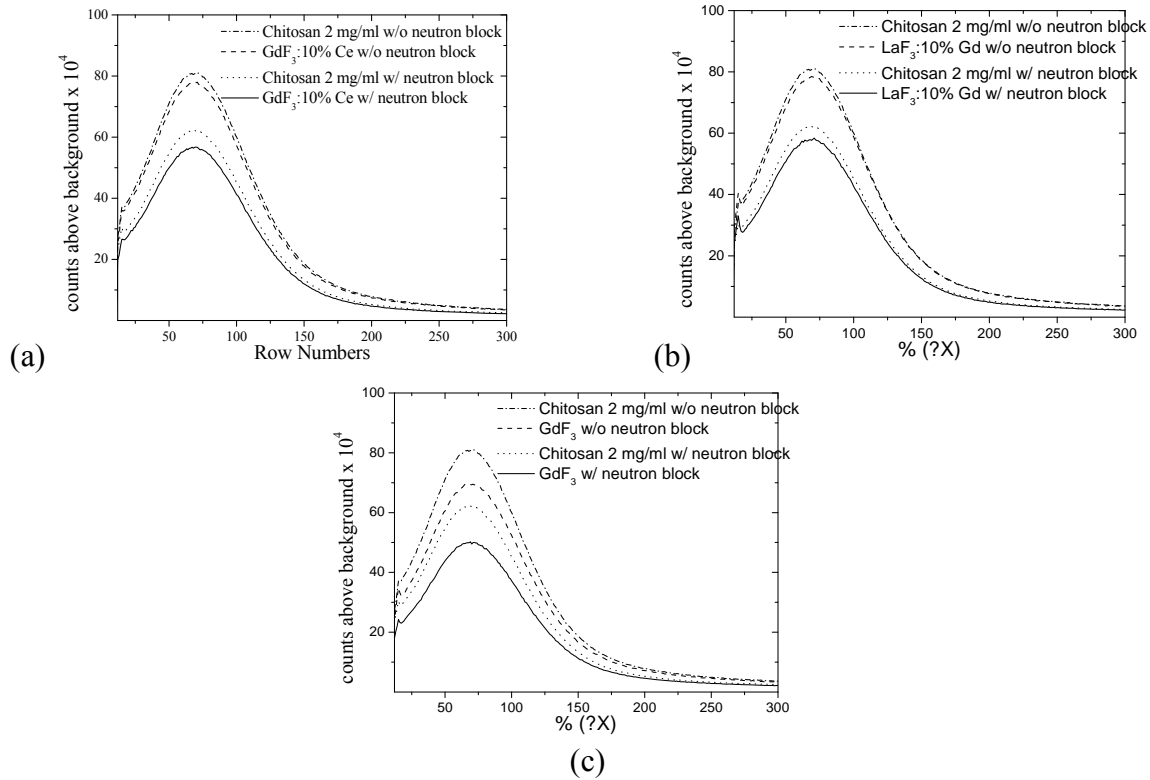


Fig. 16.6. Neutron detection results for (a) GdF<sub>3</sub>:10%Ce; (b) LaF<sub>3</sub>:10%Gd; and (c) GdF<sub>3</sub> NCs.

All of the Gd-containing materials showed fewer absolute counts than the control chitosan solution, which was consistent with the results from the gamma ray detection experiments and was attributed to high levels of self-absorption in the material. The important observation, however, was the increased counts detected from all three unshielded Gd-containing NC materials in comparison with a similar increase in counts detected from unshielded control sample of 2 mg/ml chitosan solution (Fig. 16.7). In all three cases, the Gd-containing NC materials showed a larger change in counts than the chitosan control sample. Since borated polyethylene is an electron-poor material, it is assumed that the gamma ray flux is largely unaffected by it. The larger change in count rates in Gd-containing NC materials is therefore due to the absorption and detection of thermalized neutrons by Gd-containing NCs.

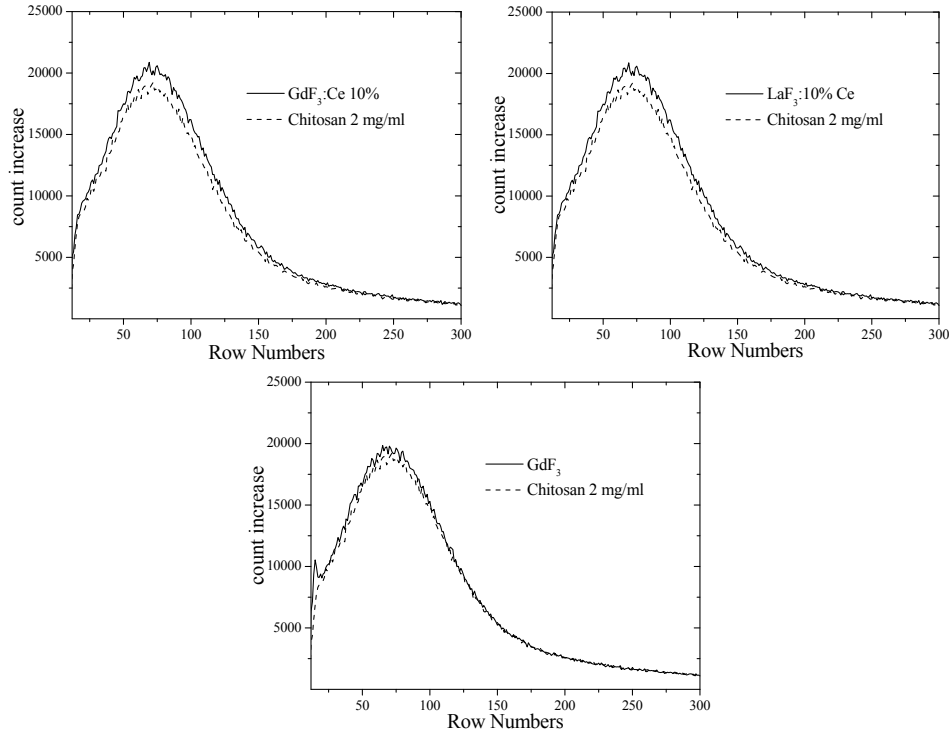


Fig. 16.7. The increase in counts in unshielded  $\text{GdF}_3:10\% \text{ Ce}$  (top left),  $\text{LaF}_3:10\% \text{ Gd}$  (top right), and  $\text{GdF}_3$  (center) NC samples versus similar increase in counts in unshielded control sample of 2 mg/ml chitosan solution.

#### **16.D. Thermal Neutron Detection Experiments with Gd-Containing $\text{Ln}_2\text{O}_3$ Nanocrystals**

##### **16.D.a. Thermal Neutron Detection Experiments with Gd-Containing $\text{Ln}_2\text{O}_3$ Nanocrystals Suspended in Toluene**

For the detection of neutrons, a 1.17 mCi  $^{252}\text{Cf}$  source was used with an activity of 0.14 mCi, generating approximately  $5.3 \times 10^6$  neutrons/s at varying kinetic energies, with an average of 2.3 MeV [Reinig 1968]. The source was placed in a 10-inch diameter polyethylene sphere used as a moderator, providing a thermal neutron source. Two 1'×1'×1" pieces of 5% borated polyethylene were used to provide neutron shielding, one piece to lower the neutron dose received by the electronics, and a second removable piece to attenuate neutron flux (but not gamma rays) received by the scintillator. The sphere and borated polyethylene slabs were mounted on an optical table as shown in Fig. 16.4(a).

The photomultiplier tube was repackaged into a smaller light-proof enclosure in order to facilitate moving the PMT and scintillator under test away from the powerful  $^{252}\text{Cf}$  source for loading a different scintillation material, thus minimizing the human exposure time. The rods seen in Fig. 16.4 provide a custom kinematic mount, allowing the PMT to be returned in exactly the same position each time, in order to maintain the geometry of the experiment.

The  $\text{Gd}_2\text{O}_3$  NCs with various dopants, capped with oleic acid and dispersed in toluene were subjected to neutron detection testing, with  $8.3 \times 10^3$  n/s passing through the midpoint of the cuvette with a plane surface area of  $2.835 \text{ cm}^2$ . The neutron flux density was  $2.95 \times 10^3 \text{ n/s-cm}^3$ , with each spontaneous fission event producing  $\sim 6.95 \text{ MeV}$  of prompt  $0.87 \text{ MeV}$  gammas. The experiments were performed with and without the borated polyethylene boards, providing neutron shielding. Predictably, the  $^{252}\text{Cf}$  source without the borated polyethylene boards produced the largest signal in all the samples. Therefore, the trends present in the data are easiest to see in that example (Fig. 16.8). While during the measurements higher count rate was consistently observed from all the NC samples as compared to pure toluene, most of the NC samples demonstrated also much higher sensitivity to the normal background radiation. Therefore, in Fig. 16.8, we show the results after the background subtraction. A definite enhancement of scintillation over the solvent was observed for the NCs of gadolinium oxide doped with 10% cerium.

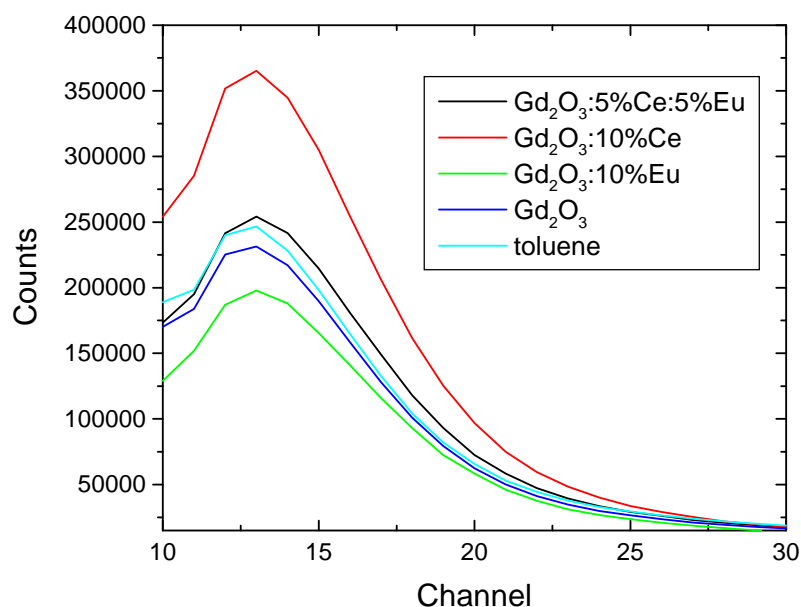


Fig. 16.8. Neutron detection results for toluene (light blue),  $\text{Gd}_2\text{O}_3$  (dark blue),  $\text{Gd}_2\text{O}_3$ :10%Eu (green),  $\text{Gd}_2\text{O}_3$ :10%Ce (red), and  $\text{Gd}_2\text{O}_3$ :5%Ce:5%Eu (black) NCs.

#### **16.D.b. Thermal Neutron Detection Experiments with Gadolinium Oxide NCs Loaded into Poly(Vinyl Toluene)**

A  $^{252}\text{Cf}$  source with a calculated activity of  $6.45 \times 10^6$  n/s was placed inside a high-density polyethylene (HDPE) sphere with a 12.7 cm radius to thermalize the neutrons. Because of the mixed nature of the fission source, energy calibration was performed with low activity ( $< 2 \mu\text{Ci}$ ) pure gamma sources placed flush to the sample, opposite the PMT inside a black box. Two 3.5-cm thick samples were prepared, one consisting of plain PVT, and the other having 1.2 wt% of  $\text{Gd}_2\text{O}_3$ :10%Ce NCs loaded into PVT. Measurements were taken both with and without  $1' \times 1' \times 1'$  pieces of 5% borated polyethylene boards in order to determine what part of the signal came from the thermalized neutrons. The boards were placed between the HDPE sphere and the PMT box. Additionally, two pieces were placed to the sides of the sphere to reduce the neutron dose

received by the electronics. The scintillation of the samples was measured by a PMT attached to an ORTEC MCA (Fig. 16.1).

Preliminary neutron irradiation tests have yielded positive results, supporting the concept of neutron detection enhancement by loading Gd-containing NCs in PVT scintillator host. The net detected difference in counts between the PVT loaded with NCs and plain PVT (Fig. 16.9) was statistically significant over the entire energy range, except for a few channels in the 50-60 channel range (the error bars were excluded from the Figure to improve its readability). For both samples, removing the borated boards, absorbing thermal neutrons, resulted in a detection signal increase, which confirms thermal neutron detection.

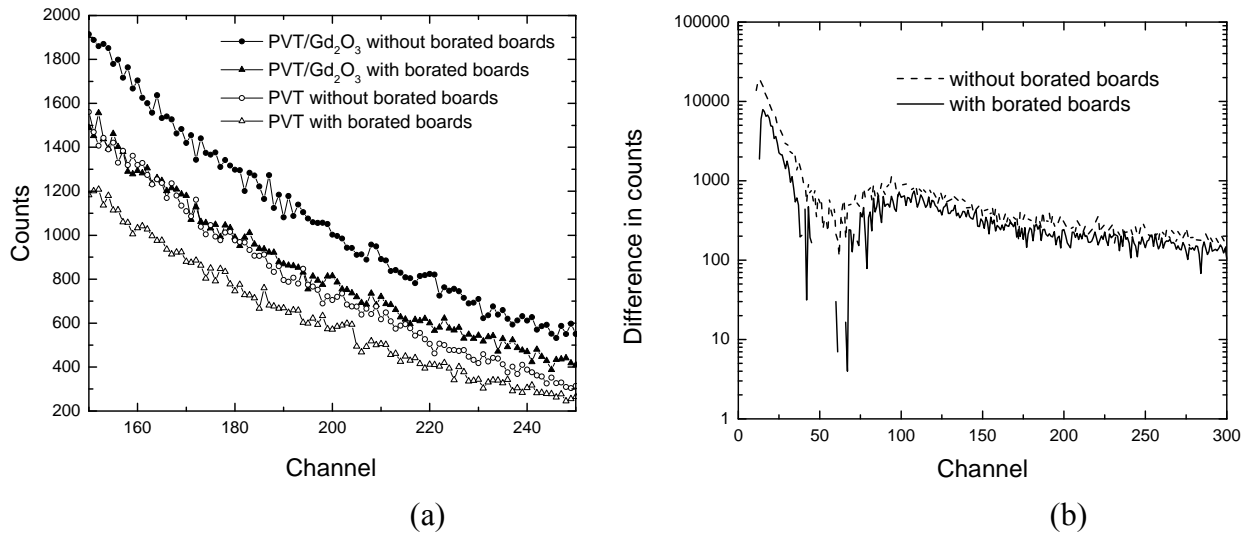
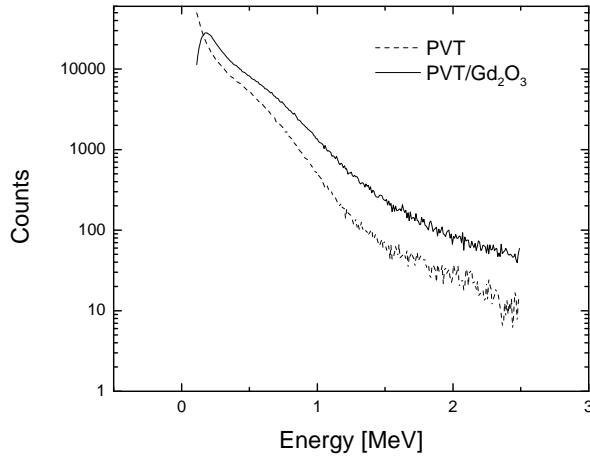
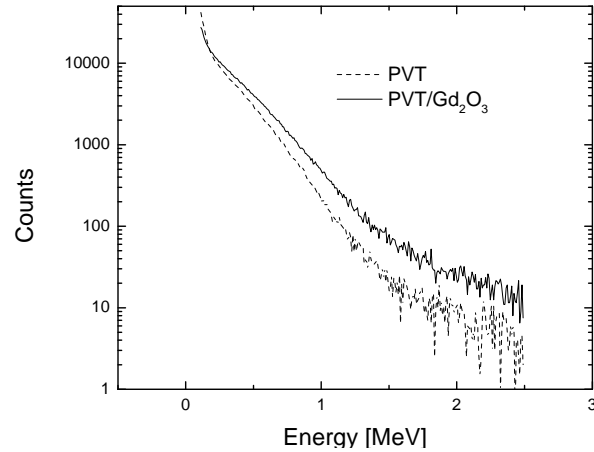
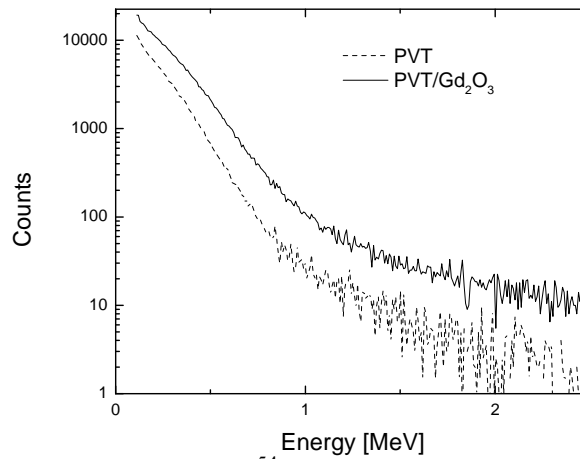


Fig. 16.9. (a)  $^{252}\text{Cf}$  induced signals from the plain PVT sample and the PVT sample loaded with NCs and (b) difference between the signal from the PVT sample loaded with NCs and that from plain PVT sample.

Energy calibration was performed using 1.5- $\mu\text{Ci}$   $^{22}\text{Na}$ , 0.8- $\mu\text{Ci}$   $^{152}\text{Eu}$ , and 1- $\mu\text{Ci}$   $^{54}\text{Mn}$  sources (Figs. 16.10 – 16.12). The full energy peaks of 1.27 MeV, 1.41 MeV, and 0.835 MeV, respectively, have not been resolved in  $\gamma$  spectra of our PVT-based samples. With Compton scattering dominating in PVT, the Compton edges of 1.06 MeV, 1.19 MeV, and 0.64 MeV, respectively, were used for the purpose of energy calibration. However, the  $^{252}\text{Cf}$  activity was  $\sim 6$  mCi, and the detection settings had to be lowered to reduce system gain, as compared to those used for calibration. Therefore, the energy calibration carried out with low-activity sources could not be directly applied to the data obtained with the  $^{252}\text{Cf}$  source. While accurate energy calibration is unavailable for the data presented in Fig. 16.9, based on the calibration with the lower activity sources and knowing the way the experimental settings were changed between the calibration and neutron irradiation experiments, the channels with the statistically insignificant difference in counts are likely to be below 1 MeV. This is further supported by MCNPX simulations that predicted the  $\gamma$ -photon signal from the plain PVT sample and that from the PVT sample loaded with Gd<sub>2</sub>O<sub>3</sub>:10%Ce NCs to be almost the same at  $\sim 800$  keV, due to contribution from higher energy neutrons.



Fig. 16.10.  $^{22}\text{Na}$  energy calibration.Fig. 16.11.  $^{152}\text{Eu}$  energy calibration.Fig. 16.12.  $^{54}\text{Mn}$  energy calibration.

In summary, we have developed a colloidal synthesis that permitted easy suspension of  $\text{Gd}_2\text{O}_3:10\%\text{Ce}$  NCs in a PVT matrix. The polymer NC composite was obtained as a homogeneous mixture, due to colloidal stability of the NCs coated with oleic acid. The nanocomposite produced gamma and neutron spectra in radiation detection experiments. Preliminary results indicate signal enhancement in PVT scintillator matrix loaded with  $\text{Gd}_2\text{O}_3:10\%\text{Ce}$  NCs as compared with plain PVT. The observed improvement is believed to come from increased thermal neutron capture by the Gd-containing nanocomposite material and from contribution of Ce emission to scintillation. While energy calibrated spectra have been achieved with low-activity  $\gamma$  sources, these measurements will be repeated with high-activity sources to allow accurate energy calibration of  $^{252}\text{Cf}$  radiation detection data.

The PVT emission consists of a large band at  $\sim 313$  nm (a broad  $\sim 315$  nm emission from PVT was reported in literature [Powell 1971]) and significantly overlaps with the absorption spectrum of  $\text{Gd}_2\text{O}_3:10\%\text{Ce}$  NCs (Fig. 7), which raises a concern of possible reabsorption of PVT emission by the NCs. To address this concern, future experiments will be performed on a series of samples of different thickness and with varying concentration of NCs.

PVT without chemical additives is known to have very low light yield. To make it practical, doping PVT polymer matrix with wavelength shifting fluors, such as bisphenyloxazolybenzene (POPOP), p-terphenyl, BPO, BBQ, or butyl-PBD [Quaranta 2003], [Reynolds 2007], [Rakes 2008], will also be undertaken for higher light yield of the PVT-based nanocomposite material.

## **17. REFERENCES**

- [Aldana 2001] J. Aldana, Y. A. Wang, and X.-G. Peng, "Photochemical instability of CdSe nanocrystals coated by hydrophilic thiols", *J. Am. Chem. Soc.*, vol. 123 (#36), pp. 8844-8850, 12 Sept. 2001.
- [Amand 1992] T. Amand, X. Marie, B. Dareys, J. Barrau, M. Brousseau, D. J. Dunstan, J. Y. Emery, and L. Goldstein, "Well-width dependence of the excitonic lifetime in strained III-V quantum-wells", *J. Appl. Phys.*, vol. 72 (#5), pp. 2077-2079, 1 Sept. 1992.
- [Anderson 1989] D. F. Anderson, "Properties of the high-density scintillator cerium fluoride", *IEEE Trans. Nucl. Sci.*, vol. 36 (#1, Pt.1), pp. 137-140, Feb. 1989.
- [Artemyev 1997] M. V. Artemyev, Y. P. Rakovich, and G. P. Yablonski, "Effect of dc electric field on photoluminescence from quantum-confined PbI<sub>2</sub> nanocrystals", *J. Cryst. Growth*, vol. 171 (#3-4), pp. 447-452, 1997.
- [Attix 1986] F. H. Attix, *Introduction to Radiological Physics and Radiation Dosimetry*, John Wiley & Sons, New York 1986, pp. 155-156 and p.187.
- [Banerjee 2007] K. Banerjee, S. Kundu, S. Mukhopadhyay, T. K. Rana, S. Bhattacharya, C. Bhattacharya, S.R. Banerjee, T. K. Ghosh, G. Mukherjee, T. Bandyopadhyay, A. Dey, J. K. Meena, P. Mukhopadhyay, D. Gupta, S. Pal, D. Pandit, and S. Bhattacharya, "Characteristics of Gd-loaded liquid scintillators BC521 and BC525", *Nucl. Instr. and Meth. in Phys. Res. A – Accelerators, Spectrometers, Detectors, & Assoc. Equipment*, vol. 580 (#3), pp. 1383-1389, 11 Oct. 2007.
- [Barbalace 2009] K. Barbalace, "Periodic table of elements – sorted by cross section (thermal neutron capture)", accessed online 10/30/2009, <http://EnvironmentalChemistry.com/yogi/periodic/crosssection.html>.
- [Bawendi 1992] M. G. Bawendi, P. J. Carroll, W. L. Wilson, and L. E. Brus, "Luminescence properties of CdSe quantum crystallites – resonance between interior and surface localized states" *J. Chem. Phys.*, vol. 96 (#2), pp. 946-954, 15 Jan. 1992.
- [Birowosuto 2005] M. D. Birowosuto, P. Dorenbos, C. W. E. van Eijk, K. W. Krämer, and H. U. Güdel, "Scintillation properties of LuI<sub>3</sub>:Ce<sup>3+</sup>-high light yield scintillators", *IEEE Trans. Nucl. Sci.*, vol. 52 (#4), pp. 1114-1118, Aug. 2005.
- [Bizarri 2006] G. Bizarri, T. M. de Haas, P. Dorenbos, and C. W. R. van Eijk, "Scintillation properties of Ø 1×1 inch<sup>3</sup> LaBr<sub>3</sub>:5%Ce<sup>3+</sup> crystal", *IEEE Trans. Nucl. Sci.*, vol. 53 (#2), pp. 615-619, April 2006.
- [Bizarri 2007] G. Bizarri and P. Dorenbos, "Charge carrier and exciton dynamics in LaBr<sub>3</sub>:Ce<sup>3+</sup> scintillators: Experiment and model", *Phys. Rev. B*, vol. 75 (#18), Art. 184302 (10 pp.), May 2007.
- [Bowman 1964] H. R. Bowman, S. G. Thompson, and J. O. Rasmussen, "Gamma-ray spectra from spontaneous fission of <sup>252</sup>Cf", *Phys. Rev. Lett.*, vol. 12 (#8), pp. 195-198, 24 Feb. 1964.
- [Broser 1982] I. Broser, R. Broser, M. Rosenzweig, and A. Hoffmann, in *Numerical Data and Functional Relationships for Science and Technology*, (O. Madelung, M. Schulz, and H. Weiss,

- Eds.), Landolt-Bornstein, New Series, Group III, vol. 17, Pt. B, Springer, Berlin 1982, pp. 166-224.
- [Campbell 2006] I. H. Campbell and B. K. Crone, "Quantum-dot/organic semiconductor composites for radiation detection", *Adv. Mater.*, vol. 18 (#1), pp. 77-79, 2006.
- [Cattaneo 1991] P. W. Cattaneo, "Calibration procedure for irradiation tests on silicon devices", *IEEE Trans. Nucl. Sci.*, vol. 38 (#3), pp. 894-900, June 1991.
- [Chand 1975] M. Chand and G. C. Trigunayat, "Atomic structures of three new rhombohedral polytypes of lead iodide", *Acta Cryst.*, vol. B31, pp. 1222-1223, 1975.
- [Chander 2005] H. Chander, "Development of nanophosphors: A review", *Materials Science & Engineering R, Reports*, vol. 49 (#5), pp. 113-155, 2005.
- [Chen 2006a] H.-S. Chen, C.-K. Hsu, and H.-Y. Hong, "InGaN-CdSe-ZnSe quantum dots white LEDs", *IEEE Photon. Technol. Lett.* **18** (#1-4), pp. 193-195, Jan.-Feb. 2006.
- [Chen 2006b] W. Chen and J. Zhang, "Using nanoparticles to enable simultaneous radiation and photodynamic therapies for cancer treatment", *J. Nanosci. Nanotechnol.*, vol. 6 (#4), pp. 1159-1166, Apr. 2006.
- [Chen 2008] D. Q. Chen, Y. S. Wang, Y. L. Yu, and P. Huang, "Structure and optical spectroscopy of Eu-doped glass ceramics containing GdF<sub>3</sub> nanocrystals", *J. Phys. Chem. C*, vol. 112 (#48), pp. 18943-18947, 2008.
- [Chuang 1998] S.-L. Chuang, N. Nakayama, A. Ishibashi, S. Taniguchi, and K. Nakano, "Degradation of II-VI blue-green semiconductor lasers", *IEEE J. Quantum Electron.*, vol. 34 (#5), pp. 851-857, May 1998.
- [Clapp 2006] A. R. Clapp, E. R. Goldman, and H. Mattoussi, "Capping of CdSe-ZnS quantum dots with DHLA and subsequent conjugation with proteins", *Nature Protocols*, vol. 1 (#3), pp. 1258-1266, 28 Sept. 2006.
- [Crooker 2003] S. A. Crooker, T. Barrick, J. A. Hollingsworth, and V. I. Klimov, "Multiple temperature regimes of radiative decay in CdSe nanocrystal quantum dots: Intrinsic limits to the dark-exciton lifetime", *Appl. Phys. Lett.*, vol. 82 (#17), pp. 2793-2795, 28 April 2003.
- [Dai 2002] S. Dai, S. Saengkerdsud, H.-J. Im, A. C. Stephan, and S. M. Mahurin, "Nanocrystal-based scintillators for radiation detection", in *Unattended Radiation Sensor Systems for Remote Applications*, Washington, DC, *AIP Conf. Proc.*, 15-17 April 2002, vol. 632, pp. 220-224.
- [deMello 1997] J. C. deMello, H. F. Wittmann, and R. H. Friend, "Improved experimental determination of external photoluminescence quantum efficiency", *Adv. Mater.*, vol. 9 (#3), p. 230, 1997.
- [Dennis 1965] J. Dennis, H. K. Henisch, and P. Cherin, "Preparation and properties of lead hydroxy-iodide in single crystal form", *J. Electrochem. Soc.*, vol. 112 (#12), pp. 1240-1241, Dec. 1965.
- [Derenzo 1992] S. E. Derenzo and W. W. Moses, "Experimental efforts and results in finding new heavy scintillators", *Proc. of the CRYSTAL 2000 International Workshop on Heavy Scintillators for Scientific and Industrial Applications*, Chamonix, France, 22-26 Sept. 1992.
- [Derenzo 2002] S. E. Derenzo, M. J. Weber, and M. K. Klintenberg, "Temperature dependence of the fast, near-band-edge scintillation from CuI, HgI<sub>2</sub>, PbI<sub>2</sub>, ZnO:Ga and CdS:In", *Nucl. Instr. & Meth. in Phys. Res. Sect. A – Accelerators, Spectrometers, Detectors, & Assoc. Equipment*, vol. 486 (#1-2), pp. 214-219, 21 June 2002.
- [Derenzo 2005] S. E. Derenzo, "Who needs better nuclear detector materials and how do we find them?", *Interdisciplinary Instrumentation Colloquium*. Berkeley: Ernest Orlando Lawrence Berkeley National Laboratory (2005).

- [DiMaio 2008] J. DiMaio, B. Kokuzo, T. L. James, T. Harkey, D. Monofsky, and J. Ballato, "Photoluminescent characterization of atomic diffusion in core-shell nanoparticles", *Optics Express*, vol. 16 (#16), pp. 11769-11775, 2008.
- [Donega 2003] C. D. Donega, S. G. Hickey, S. F. Wuister, D. Vanmaekelbergh, and A. Meijerink, "Single-step synthesis to control the photoluminescence quantum yield and size dispersion of CdSe nanocrystals", *J. Phys. Chem. B*, vol. 107 (#2), pp. 489-496, 16 Jan. 2003.
- [Donega 2006] C. D. Donega, M. Bode, and A. Meijerink, "Size- and temperature-dependence of exciton lifetimes in CdSe quantum dots", *Phys. Rev. B*, vol. 74 (#8), Art. 085320, Aug. 2006.
- [Dorenbos 2000a] P. Dorenbos, "The  $4f^n \leftrightarrow 4f^{n-1} 5d$  transitions of the trivalent lanthanides in halogenides and chalcogenides", *J. Lumin.*, vol. 91, pp. 91-106, 2000.
- [Dorenbos 2000b] P. Dorenbos, "The 5d level positions of the trivalent lanthanides in inorganic compounds", *J. Lumin.*, vol. 91, pp. 155-176, 2000.
- [Dorenbos 2000c] P. Dorenbos, "5d-level energies of  $Ce^{3+}$  and the crystalline environment. I. Fluoride compounds", *Phys. Rev. B*, vol. 62, no. 23, pp. 15640-15649, 2000.
- [Dorenbos 2000d] P. Dorenbos, "5d-level energies of  $Ce^{3+}$  and the crystalline environment. II. Chloride, bromide, and iodide compounds", *Phys. Rev. B*, vol. 62, no. 23, pp. 15650-15659, 2000.
- [Dorenbos 2005] P. Dorenbos, "Scintillation mechanisms in  $Ce^{3+}$  doped halide scintillators", *Phys. Status Solidi A*, vol. 202 (#2), pp. 195-200, Jan. 2005.
- [Dorenbos 2006] P. Dorenbos, E. V. D. van Loef, A. P. Vink, E. van der Kolk, C. W. E. van Eijk, K. W. Krämer, H. U. Güdel, W. M. Higgins, and K. S. Shah, "Level location and spectroscopy of  $Ce^{3+}$ ,  $Pr^{3+}$ ,  $Er^{3+}$ , and  $Eu^{2+}$  in  $LaBr_3$ ", *J. Lumines.*, vol. 117 (#2), pp. 147-155. Apr. 2006.
- [Eckerman 2003] K. Eckerman, *Radiological Toolbox Computer Program*, Oak Ridge National Lab., 2003.
- [Efros 1996] A. L. Efros, M. Rosen, M. Kuno, M. Nirmal, D. J. Norris, and M. Bawendi, "Band-edge exciton in quantum dots of semiconductors with a degenerate valence band: Dark and bright exciton states", *Phys. Rev. B*, vol. 54 (#7), pp. 4843-4856, 15 Aug. 1996.
- [Finlayson 2006] C. E. Finlayson and P. J. A. Sazio, "Highly efficient blue photoluminescence from colloidal lead-iodide nanoparticles", *J. Phys. D-Appl. Phys.*, vol. 39 (#8), pp. 1477-1480, 2006.
- [Glodo 2005] J. Glodo, W. W. Moses, W. M. Higgins, E. V. D. van Loef, P. Wong, S. E. Derenzo, M. J. Weber, K. S. Shah, "Effects of Ce concentration on scintillation properties of  $LaBr_3:Ce$ ", *IEEE Trans. Nucl. Sc.*, vol. 52 (#5), pp. 1805-1808, Oct. 2005.
- [Glodo 2006] J. Glodo, W. M. Higgins, E. V. D. van Loef, and K. S. Shah, " $GdI_3:Ce$  – A new gamma and neutron scintillator", *IEEE Nuclear Science Symposium Conference Record*, Vol. 3, San Diego, CA, pp. 1574-1577, 2006.
- [Gupta 2009] N. Gupta, G. F. Alapatt, R. Podila, R. Singh, and K. F. Poole, "Prospects of nanostructure-based solar cells for manufacturing future generations of photovoltaic modules", *International J. Photoenergy*, vol. 2009, Art. 154059, 2009 (13 pp).
- [Gurler 2009] O. Gurler, H. Oz, S. Yalcin, and O. Gundogdu, "Mass absorption and mass energy transfer coefficients for 0.4-10 MeV gamma rays in elemental solids and gases", *Appl. Radiat. Isot.*, vol. 67 (#1), pp. 201-205, Jan. 2009.
- [Hamamatsu 2008] Hamamatsu Photonics, "Photomultiplier tubes, basics and applications", 3rd Edition, pp 152 (2008)  
[http://sales.hamamatsu.com/assets/applications/ETD/pmt\\_handbook\\_complete.pdf](http://sales.hamamatsu.com/assets/applications/ETD/pmt_handbook_complete.pdf).

- [Higgins 2008] W. M. Higgins, A. Churilov, E. van Loef, J. Glodo, M. Squillante, and K. Shah, "Crystal growth of large diameter  $\text{LaBr}_3\text{:Ce}$  and  $\text{CeBr}_3$ ", *J. Crystal Growth*, vol. 310 (#7-9), pp. 2085-2089, April 2008.
- [Hubbel 2004] J. H. Hubbel and S. M. Seltzer, *Tables of X-Ray Mass Attenuation Coefficients and Mass Energy-Absorption Coefficients (V 1.4)*, 12 July 2004 [Online database available at <http://physics.nist.gov/xaamdi>].
- [Katagiri 2003] M. Katagiri, A. Birumachi, K. Sakasai, and K. Takahashi, "Portable gamma-ray monitor composed of a compact electrically cooled Ge detector and a mini-MCA system", *IEEE Trans. Nucl. Sci.*, vol. 50 (#4, Pt. 1), pp. 1043-1047, Aug. 2003.
- [Khanna 2005] R. Khanna, S. Y. Han, S. J. Pearton, D. Schoenfeld, W. V. Schoenfeld, and F. Ren, "High dose Co-60 gamma irradiation of InGaN quantum well light-emitting diodes", *Appl. Phys. Lett.*, vol. 87 (#21), Art. 212107, 21 Nov. 2005.
- [Kim 2004] Y. K. Kim, H. K. Kim, D. K. Kim, and G.-S. Cho, "Synthesis of Eu-doped  $(\text{Gd,Y})_2\text{O}_3$  transparent optical ceramic scintillator", *J. Materials Res.*, vol. 19 (#2), pp. 413-416, Feb. 2004.
- [Klein 1967] P. H. Klein and W. J. Croft, "Thermal conductivity, diffusivity, and expansion of  $\text{Y}_2\text{O}_3$ ,  $\text{Y}_3\text{Al}_5\text{O}_{12}$ , and  $\text{LaF}_3$  in the range  $77^\circ\text{--}300^\circ\text{K}$ ", *J. Appl. Phys.*, vol. 38 (#4), 1603-1607, 15 March 1967.
- [Klimov 2006] V. I. Klimov, "Mechanisms for photogeneration and recombination of multiexcitons in semiconductor nanocrystals: Implications for lasing and solar energy conversion", *J. Phys. Chem. B*, vol. 110, no.34, pp. 16827-16845, Aug. 2006.
- [Klink 2000] S. I. Klink, G. A. Hebbink, L. Grave, F. G. A. Peters, F. C. J. M. Van Veggel, D. N. Reinhoudt, and J. W. Hofstraat, "Near-infrared and visible luminescence from terphenyl-based lanthanide(III) complexes bearing amido and sulfonamido pendant arms", *Eur. J. Org. Chem.*, vol. 10, pp.1923-1931, 2000.
- [Klintonberg 2002] M. Klintonberg, S. E. Derenzo, and M. J. Weber, "Potential scintillators identified by electronic structure calculations", *Nucl. Instr. & Meth. in Phys. Res. Sect. A – Accelerators, Spectrometers, Detectors, & Assoc. Equipment*, vol. 486 (#1-2), pp. 298-302, 21 June 2002.
- [Klintonberg 2003] M. K. Klintonberg, M. J. Weber, and D. E. Derenzo, "Luminescence and scintillation of  $\text{PbI}_2$  and  $\text{HgI}_2$ ", *J. Lumin.*, vol. 102, pp. 287-290, May 2003.
- [Knoll 2000] G. F. Knoll, *Radiation Detection and Measurement*, 3<sup>rd</sup> Ed., John Wiley & Sons, p. 119, 2000.
- [Kobayashi 2003] M. Kobayashi, R. Nakamura, M. Ishii, N. Solovieva, and M. Nikl, "Energy transfer phenomena in  $\text{GdF}_3\text{:Mn}$  co-doped with  $\text{Ce}^{3+}$ ,  $\text{Pr}^{3+}$  or  $\text{Zr}^{4+}$ ", *Jpn. J. Appl. Phys. Pt. 1*, vol. 42 (#4A), pp. 1648-1654, 2003.
- [Kramer 1985] V. Kramer, E. Post, "Preparation and structural characterization of the lead oxide iodide  $\text{Pb}_3\text{O}_2\text{I}_2$ ", *Mat. Res. Bull.*, vol. 20, pp 407-412, 1985.
- [Krämer 2006] K. W. Krämer, P. Dorenbos, H. U. Güdel, and C. W. E. van Eijk, "Development and characterization of highly efficient new cerium doped rare earth halide scintillator materials", *J. Mater. Chem.*, vol. 16 (#27), pp. 2773-2780, 18 May 2006.
- [Krivandina 2006] E. A. Krivandina, Z. I. Zhmurova, B. P. Sobolev, T. M. Glushkova, D. F. Kiselev, M. M. Firsova, and A. P. Shtyrkova, "Growth of  $R_{1-y}\text{Sr}_y\text{F}_{3-y}$  crystals with rare earth elements of the cerium subgroup ( $R = \text{La, Ce, Pr, or Nd}$ ;  $0 \leq y \leq 0.16$ ) and the dependence of their density and optical characteristics on composition", *Crystallogr. Rep.*, vol. 51 (#5), pp. 895-901, Sept. 2006.

- [Kuno 1997] M. Kuno, J. K. Lee, B. O. Dabbousi, F. V. Mikulec, and M. G. Bawendi, "The band edge luminescence of surface modified CdSe nanocrystallites: Probing the luminescing state", *J. Chem. Phys.*, vol. 106 (#23), pp. 9869-9882, 15 June 1997.
- [Labeau 2003] O. Labeau, P. Tamarat, and B. Lounis, "Temperature dependence of the luminescence lifetime of single CdSe/ZnS quantum dots", *Phys. Rev. Lett.*, vol. 90 (#25), Art. 257404, 27 June 2003.
- [Lecoq 2000] P. Lecoq and M. Korzhik, "Scintillator developments for high energy physics and medical imaging", *IEEE Trans. Nucl. Sci.*, vol. 47 (#4, Pt.1), pp. 1311-1314, Aug. 2000.
- [Létant 2006a] S. E. Létant and T.-F. Wang, "Study of porous glass doped with quantum dots or laser dyes under alpha irradiation", *Appl. Phys. Lett.*, vol. 88, no. 10, Art. 103110, 8 March 2006.
- [Létant 2006b] S. E. Létant and T. F. Wang, "Semiconductor quantum dot scintillation under  $\gamma$ -ray irradiation", *Nano Lett.*, vol. 6, no. 12, pp. 2877-2880, 13 Dec. 2006.
- [Li 2007] Y.-Q. Li, A. Rizzo, R. Cingolani, and G. Gigli, "White-light-emitting diodes using semiconductor nanocrystals", *Microchimica Acta*, vol. 159, no. 3-4, pp. 207-215, July 2007.
- [Liu 2006] X.-J. Liu; H.-L. Li; R.-J. Xie; N. Hirosaki; X. Xu; and L.-P. Huang, "Cerium-doped lutetium aluminum garnet optically transparent ceramics fabricated by a sol-gel combustion process", *J. Mater. Res.*, vol. 21 (#6), pp. 1519-1525, June 2006.
- [Liu 2007] X. J. Liu, H. L. Li, R. J. Xie, N. Hirosaki, X. Xu, and L. P. Huang, "Synthesis, characterization, and luminescent properties of  $\text{Lu}_2\text{O}_3\text{:Eu}$  phosphors", *J. Lumines.*, vol. 127 (#2), pp. 469-473, Dec. 2007.
- [Locock 2003] A. Locock and P. Burns, "The crystal structure of synthetic autunite,  $\text{Ca}[(\text{UO}_2)(\text{PO}_4)]_2(\text{H}_2\text{O})_{11}$ ", *Am. Mineral.*, vol. 88, pp. 240-244, 2003.
- [Lozano 2006] K. Lozano, C. Hernandez, T. W. Petty, M. B. Sigman, and B. Korgel, "Electrorheological analysis of nano laden suspensions", *J. of Colloid and Interface Sci.*, vol. 297, pp. 618-624, 2006.
- [Matsui 2005] I. Matsui, "Nanoparticles for electronic device applications: A brief review", *J. Chem. Eng. Japan*, vol. 38, no. 8, pp. 535-546, Aug. 2005.
- [McCallum 2005] S. McCallum, P. Clowes, and A. Welch, "A four-layer attenuation compensated PET detector based on APD arrays without discrete crystal elements", *Phys. Med. Biol.*, vol. 50(#17), pp. 4187-4207, 2005.
- [McIlwain 2008] M. E. McIlwain, D. Gao, and N. Thompson, "First principle quantum description of the energetics associated with  $\text{LaBr}_3$ ,  $\text{LaCl}_3$ , and Ce doped scintillators", 2008 *Am. Phys. Soc. March Meeting*, New Orleans, LA, 10-14 March 2008, Idaho National Lab., Preprint INL/CON-07-13547.
- [McKigney 2007] E. A. McKigney, R. E. Del Sesto, L. G. Jacobsohn, P. A. Santi, R. E. Muenchausen, K. C. Ott, T. M. McCleskey, B. L. Bennett, J. F. Smith, and D. W. Cooke, "Nanocomposite scintillators for radiation detection and nuclear spectroscopy", *Nucl. Instr. & Meth. in Phys. Res. Sect. A – Accelerators, Spectrometers, Detectors, & Assoc. Equipment*, vol. 579 (#1), pp. 15-18, 21 Aug. 2007.
- [Meiser 2004] F. Meiser, C. Cortez, and F. Caruso, "Biofunctionalization of fluorescent rare-earth-doped lanthanum phosphate colloidal nanoparticles", *Angew. Chem. Int. Ed.*, vol. 43 (#44), pp. 5954-5957, 2004.
- [Miri Hakimabad 2007] H. Miri Hakimabad, R. Izadi, A. R. Vejdani, and H. Panjeh, "Reduction of the gamma dose equivalent due to  $^{252}\text{Cf}$  and  $^{241}\text{Am}$ -Be neutron sources in the patients soft tissues when using body chemical composition analyzer bed", *Asian J. Exp. Sci.*, vol. 21 (#1), pp. 133-144, 2007.

- [Moses 1990a] W. W. Moses and S. E. Derenzo, "Lead carbonate, a new fast, heavy scintillator", *IEEE Trans. Nucl. Sci.*, vol. 37 (#2), pp. 96-100, April 1990.
- [Moses 1990b] W. W. Moses and S. E. Derenzo, "The scintillation properties of cerium-doped lanthanum fluoride", *Nucl. Instr. & Meth. in Phys. Res. Sect. A – Accelerators, Spectrometers, Detectors, & Assoc. Equipment*, vol. 299 (#1-3), pp. 51-56, 20 Dec. 1990.
- [Moses 1992] W. W. Moses, S. E. Derenzo, and P. J. Shlichta, "Scintillation properties of lead sulfate", *IEEE Trans. Nucl. Sci.*, vol. 39 (#5), pp. 1190-1194, Oct. 1992.
- [Moses 2005] W. W. Moses and K. S. Shah, "Potential for  $\text{RbGd}_2\text{Br}_7\text{:Ce}$ ,  $\text{LaCl}_3\text{:Ce}$ ,  $\text{LaBr}_3\text{:Ce}$ , and  $\text{LuI}_3\text{:Ce}$  in nuclear medical imaging", *Nucl. Instr. & Meth. in Phys. Res. Sect. A – Accelerators, Spectrometers, Detectors, & Assoc. Equipment*, vol. 537 (#1-2), pp. 317-320, 21 Jan. 2005.
- [Mutlugun 2007] E. Mutlugun, I. M. Soganci, and H. V. Demir, "Nanocrystal hybridized scintillators for enhanced detection and imaging on Si platforms in UV", *Optics Express*, vol. 15 (#3), pp. 1128-1134, 5 Feb. 2007.
- [Mutlugun 2008] E. Mutlugun, I. M. Soganci, and H. V. Demir, "Photovoltaic nanocrystal scintillators hybridized on Si solar cells for enhanced conversion efficiency in UV", *Optics Express*, vol. 16 (#6), pp. 3537-3545, 17 March 2008.
- [Nakayama 2002] M. Nakayama, N. Ando, T. Miyoshi, J. Hirai, and H. Nishimura, "Scintillation from NaI nanoparticles formed in  $\text{CsI:Na}$  thin films", *Jpn. J. Appl. Phys. Pt. 2*, vol. 41 (#3A), pp. L263-L265, 1 March 2002.
- [Nakayama 2005] M. Nakayama, K. Okuda, N. Ando, and H. Nishimura, "Scintillation properties of  $\text{CsI:Na}$  thin films from viewpoint of nanoparticle formation", *J. Lumines.*, vol. 112 (#1-4), pp. 156-160, April 2005.
- [Nakayama 2004] M. Nakayama, N. Ando, J. Hirai, and H. Nishimura, "Scintillation activated by nanoparticle formation in  $\text{CsI:Na}$  thin films", *J. Lumines.*, vol. 108 (#1-4), pp. 359-363, June 2004.
- [Nirmal 1994] M. Nirmal, C. B. Murray, and M. G. Bawendi, "Fluorescence-line narrowing in  $\text{CdSe}$  quantum dots – surface localization of the photogenerated exciton", *Phys. Rev. B*, vol. 50 (#4), pp. 2293-2300, 1994.
- [Normand 2007] S. Normand, A. Iltis, F. Bernard, T. Domenech, and P. Delacour, "Resistance to gamma irradiation of  $\text{LaBr}_3\text{:Ce}$  and  $\text{LaCl}_3\text{:Ce}$  single crystals", *Nucl. Instrum. Methods Phys. Res. Sect. A - Accel. Spectrom. Detect. Assoc. Equip.*, vol. 572 (#2), pp. 754-759, 11 March 2007.
- [Okuyama 1997] K. Okuyama, I. W. Lenggoro, N. Tagami, S. Tamaki, and N. Tohge, "Preparation of  $\text{ZnS}$  and  $\text{CdS}$  fine particles with different particle sizes by a spray-pyrolysis method", *J. Mater. Sc.*, vol. 32 (#5), pp. 1229-1237, 1997.
- [Osiński 2006] M. Osiński, K. Yamamoto, and T. M. Jovin (Eds.), *Colloidal Quantum Dots for Biomedical Applications*, SPIE International Symp. on Biomedical Optics BiOS 2006, San Jose, CA, 22-24 Jan. 2006, *Proc. SPIE*, vol. 6096.
- [Osiński 2007] M. Osiński, T. M. Jovin, and K. Yamamoto (Eds.), *Colloidal Quantum Dots for Biomedical Applications II*, SPIE International Symp. on Biomedical Optics BiOS 2007, San Jose, CA, 20-23 Jan. 2007, *Proc. SPIE*, vol. 6448.
- [Osiński 2008] M. Osiński, T. M. Jovin, and K. Yamamoto (Eds.), *Colloidal Quantum Dots for Biomedical Applications III*, SPIE International Symp. on Biomedical Optics BiOS 2008, San Jose, CA, 19-21 Jan. 2008, *Proc. SPIE*, vol. 6866.

- [Osiński 2009] M. Osiński, T. M. Jovin, and K. Yamamoto (Eds.), *Colloidal Quantum Dots for Biomedical Applications IV*, SPIE International Symp. on Biomedical Optics BiOS 2009, San Jose, CA, 24-26 Jan. 2009, *Proc. SPIE*, vol. 7189.
- [Osiński 2010] M. Osiński, W. J. Parak, T. M. Jovin, and K. Yamamoto (Eds.), *Colloidal Quantum Dots for Biomedical Applications V*, SPIE International Symp. on Biomedical Optics BiOS 2010, San Francisco, CA, 23-25 Jan. 2010, *Proc. SPIE*, vol. 7575.
- [Ovechkina 2009] L. Ovechkina, K. Riley, S. Miller, Z. Bell, and V. Nagarkar, "Gadolinium loaded plastic scintillators for high efficiency neutron detection", *Physics Procedia*, vol. 2 (#2), pp. 161-170, Aug. 2009.
- [Papavassiliou 1997] G. C. Papavassiliou, "Three- and low-dimensional inorganic semiconductors", *Prog. Solid State Chem.*, vol. 25 (#3-4), pp. 125-270, 1997.
- [Parak 2011] W. J. Parak, K. Yamamoto, and M. Osiński (Eds.), *Colloidal Quantum Dots/Nanocrystals for Biomedical Applications VI*, SPIE International Symp. on Biomedical Optics BiOS 2011, San Francisco, CA, 22-24 Jan. 2011, *Proc. SPIE*, vol. 7909.
- [Parak 2012] W. J. Parak, K. Yamamoto, and M. Osiński (Eds.), *Colloidal Nanocrystals for Biomedical Applications VII*, SPIE International Symp. on Biomedical Optics BiOS 2012, San Francisco, CA, 23-26 Jan. 2012, *Proc. SPIE*, vol. 8255.
- [Pelowitz 2008] D. B. Pelowitz, Ed., *MCNPX<sup>TM</sup> User's Manual*, Version 2.6.0, LA-CP-07-1473, ORNL/RSICC, April 2008.
- [Pidol 2004] L. Pídol, A. Kahn-Harari, B. Viana, E. Virey, B. Ferrand, P. Dorenbos, J. T. M. de Haas, and C. W. E. van Eijk, "High efficiency of lutetium silicate scintillators, Ce-doped LPS, and LYSO crystals", *IEEE Trans. Nucl. Sci.*, vol. 51 (#3), pp. 1084-1087, June 2004.
- [Porres 2006] L. Porres, A. Holland, L. O. Palsson, A. P. Monkman, C. Kemp, and A. Beeby, "Absolute measurements of photoluminescence quantum yields of solutions using an integrating sphere", *J. Fluoresc.*, vol. 16 (#2), pp. 267-272, 2006.
- [Powell 1971] R. C. Powell, "Energy transfer in poly(vinyl toluene)", *J. Chem. Phys.*, vol. 55, no. 4, pp. 1871-1877, Aug. 1971.
- [Quaranta 2003] A. Quaranta, A. Vomiero, S. Carturan, G. Maggioni, and G. Della Mea, "New high radiation resistant scintillating thin films", *Synthetic Metals*, vol. 138, pp. 275-279, 2 June 2003.
- [Rakes 2008] K. D. Rakes, *Evaluating The Response of Polyvinyl Toluene Scintillators Used In Portal Detectors*, MS Thesis, Air Force Institute of Technology, AFIT/GNE/ENP/08-M04, 2008.
- [Reinig 1968] W. C. Reinig, "Californium-252: A new isotopic source for neutron radiography", *Savannah River Lab. Report DP-MS-68-48*, 15 July 1968.
- [Reynolds 2007] J. G. Reynolds and G. E. Lawson, "Polymers and materials for antiterrorism and homeland defense: An overview", *Symp. on Polymers and Materials for Antiterrorism and Homeland Defense* (J. G. Reynolds, G. E. Lawson, and C. J. Koester, Eds.), Anaheim, CA, 28 March – 1 April 2004, *ACS Symp. Series*, vol. 980, pp. 3-16, 2007.
- [Sankar 2009] K. Sankar, J. B. Plumley, B. A. Akins, T. A. Memon, N. J. Withers, G. A. Smolyakov, and M. Osiński, "Synthesis and characterization of scintillating cerium-doped lanthanum fluoride nanocrystals", in *Colloidal Quantum Dots for Biomedical Applications IV*, (M. Osiński, T. M. Jovin, and K. Yamamoto, Eds.), SPIE International Symp. on Biomedical Optics BiOS 2009, San Jose, CA, 24-26 Jan. 2009, *Proc. SPIE*, vol. 7189, Art. 7189-09 (12 pp.).
- [Schillinger 2001] B. Schillinger, "Neutron detectors using CCD cameras", *Proceedings of International Workshop on Position-Sensitive Neutron Detectors*, 28-30 June, 2001, Hahn-Meitner-Institut, Berlin, Germany.



- [Schwartz 1973] A. Schwartz and J. C. O'Connell, "Photoluminescence of gel-grown Pb(OH)I single crystals", *J. Electrochem. Soc.: Solid-State Sci. and Tech.*, vol. 120 (#5), pp. 697-698, May 1973.
- [Shah 2003] K. S. Shah, J. Glodo, M. Klugerman, W. W. Moses, S. E. Derenzo, and A. J. Weber, "LaBr<sub>3</sub>:Ce scintillators for gamma-ray spectroscopy", *IEEE Trans. Nucl. Sci.*, vol. 50 (#6, Pt. 2), pp. 2410-2413, Dec. 2003.
- [Shah 2004] K. S. Shah, J. Glodo, M. Klugerman, W. M. Higgins, T. Gupta, and P. Wong, "High energy resolution scintillation spectrometers", *IEEE Trans. Nucl. Sci.*, vol. 51 (#5, Pt. 1), pp. 2395-2399, Oct. 2004.
- [Shang 2006] H.-M. Shang, Y. Wang, B. Milbrath, M. Bliss, and G.-Z. Cao, "Doping effects in nanostructured cadmium tungstate scintillation films", *J. Lumines.*, vol. 121 (#2), pp. 527-534, Dec. 2006.
- [Shestakova 2005] I. Shestakova, S. V. Tipnis, V. Gaysinskiy, J. J. Antal, L. Bobek, and V. V. Nagarkar, "A new sensor for thermal neutron imaging", *IEEE Trans. Nucl. Sci.*, vol. 52 (#4), pp. 1109-1113, 2005.
- [Shestakova 2007] I. Shestakova, V. Gaysinskiy, J. Antal, L. Bobek, V. V. Nagarkar, "A new scintillator structure for thermal neutron imaging", *Nucl. Instr. & Meth. in Phys. Res. B*, vol. 263 (#1), pp. 234-238, 2007.
- [Shibuya 2004a] K. Shibuya, M. Koshimizu, K. Asai, and H. Shibata, "Quantum confinement for large light output from pure semiconducting scintillators", *Appl. Phys. Lett.*, vol. 84 (#22), pp. 4370-4372, 31 May 2004.
- [Shibuya 2004ba] K. Shibuya, M. Koshimizu, H. Murakami, Y. Muroya, Y. Katsumura, and K. Asai, "Development of ultra-fast semiconducting scintillators using quantum confinement effect", *Jpn. J. Appl. Phys. Pt. 2*, vol. 43 (#10B), pp. L1333-L1336, 15 Oct. 2004.
- [Shultis 2007] J. K. Shultis and R. E. Faw, *Fundamentals of Nuclear Science and Engineering*, 2<sup>nd</sup> Ed., CRC Press, 2007, p. 145.
- [Söderlind 2005] F. Söderlind, H. Pedersen, R. M. Petoral, Jr., P.-O. Käll, K. Uvdal, "Synthesis and characterisation of Gd<sub>2</sub>O<sub>3</sub> nanocrystals functionalised by organic acids", *J. Colloid & Interface Sci.*, vol. 288 (#1), pp. 140-148, 1 Aug. 2005.
- [Sommers 2007] R. C. Somers, M. G. Bawendi, and D. G. Nocera, "CdSe nanocrystal based chem-/bio-sensors", *Chem. Soc. Rev.*, vol. 36 (#4), pp. 579-591, 2007.
- [Sonzongi 2009] A. Sonzongi, "Nudat 2.5", <http://www.nndc.bnl.gov/nudat2/>, Online Database.
- [Stouwdam 2003] J. W. Stouwdam, G. A. Hebbink, J. Huskens, and F. C. J. M. van Veggel, "Lanthanide-doped nanoparticles with excellent luminescent properties in organic media", *Chem. Mater.*, vol. 15 (#24), pp. 4604-4616, 2003.
- [Stouwdam 2004] J. W. Stouwdam and F. C. J. M. van Veggel, "Improvement in the luminescence properties and processability of LaF<sub>3</sub>/Ln and LaPO<sub>4</sub>/Ln nanoparticles by surface modification", *Langmuir*, vol. 20 (#26), pp. 11763 -11771, 21 Dec. 2004.
- [Stubicar 2005] N. Stubicar, P. Zipper, and B. Cherney, "Variety of aggregation and growth processes of lanthanum fluoride as a function of La/F activity ratio", *Crystal Growth & Design*, vol. 5 (#1), pp. 123-128, 2005.
- [Surti 2007] S. Surti, A. Kuhn, M. Werner, A. Perkins, J. Kolthammer, and J. Karp, "Performance of Philips Gemini TF PET/CT scanner with special considerations for its time-of-flight imaging capabilities", *J. Nucl. Med.*, vol. 48 (#3), pp. 471-480, 2007.

- [Tada 2009] H. Tada, T. Kiyonaga, and S. Naya, "Rational design and applications of highly efficient reaction systems photocatalyzed by noble metal nanoparticle-loaded titanium(IV) dioxide more options", *Chem. Soc. Rev.*, vol. 38 (#7), pp. 1849-1858, 2009.
- [van Loef 2001a] E. V. D. van Loef, P. Dorenbos, C. W. E. van Eijk, K. Krämer, and H. U. Güdel, "Scintillation properties of  $\text{LaCl}_3\text{:Ce}^{3+}$  crystals: Fast, efficient, and high-energy resolution scintillators", *IEEE Trans. Nucl. Sci.*, vol. 48 (#3), pp. 341-345, June 2001.
- [van Loef 2001b] E. V. D. van Loef, P. Dorenbos, C. W. E. van Eijk, K. Krämer, and H. U. Güdel, "High-energy-resolution scintillator:  $\text{Ce}^{3+}$  activated  $\text{LaBr}_3$ ", *Appl. Phys. Lett.*, vol. 79 (#10), pp. 1573-1575, 3 Sept. 2001.
- [van Loef 2003] E. V. D. van Loef, P. Dorenbos, C. W. E. van Eijk, K. W. Krämer, and H. U. Güdel, "Influence of the anion on the spectroscopy and scintillation mechanism in pure and  $\text{Ce}^{3+}$ -doped  $\text{K}_2\text{LaX}_5$  and  $\text{LaX}_3$  ( $\text{X}=\text{Cl}, \text{Br}, \text{I}$ )", *Phys. Rev. B*, vol. 68 (#4), Art. 045108 (9 pp), July 2003.
- [Verger 2005] L. Verger, P. Ouvrier-Buffet, F. Mathy, G. Montemont, M. Picone, J. Rustique, and C. Riffard, "Performance of a new CdZnTe portable spectrometric system for high energy applications", *IEEE Trans. Nucl. Sci.*, vol. 52 (#5, Pt. 3), pp. 1733-1738, Oct. 2005.
- [Wald 2009] M. L. Wald, "Shortage slows a program to detect nuclear bombs", *The New York Times*, 22 Nov. 2009.
- [Wang 2006] F. Wang, Y. Zhang, X.-P. Fan, and M.-Q. Wang, "One-pot synthesis of chitosan/ $\text{LaF}_3\text{:Eu}^{3+}$  nanocrystals for bio-applications", *Nanotechnology*, vol. 17 (#5), pp. 1527-1532, 14 March 2006.
- [Wang 2007] Z. Wang, J. Bo, S. Song, L. Hu, J. Liu, and X. Zhen, "One-step synthesis of highly water-soluble  $\text{LaF}_3\text{:Ln}^{3+}$  nanocrystals in methanol without using any ligands", *Nanotechnology*, vol. 18 (#46), pp. 465-476, 2007.
- [Weber 2002] M. J. Weber, "Inorganic scintillators: Today and tomorrow", *J. Lumines.*, vol. 100 (#1-4), pp. 35-45, Dec. 2002.
- [Wilkinson 2004] J. Wilkinson, K. B. Ucer, and R. T. Williams, "Picosecond excitonic luminescence in ZnO and other wide-gap semiconductors", *Radiation Measurements*, vol. 38 (#4-6), pp. 501-505, Aug.-Dec. 2004.
- [Wojtowicz 1994] A. J. Wojtowicz, M. Balcerzyk, and A. Lempicki, "Optical spectroscopy and scintillation mechanisms of  $\text{Ce}_x\text{La}_{1-x}\text{F}_3$ ", *Phys. Rev. B*, vol. 49 (#21), pp. 14880-14895, 1 June 1994.
- [Xie 2005] R.-G. Xie, U. Kolb, J.-X. Li, T. Basché, and A. Mews, "Synthesis and characterization of highly luminescent CdSe-Core CdS/ $\text{Zn}_{0.5}\text{Cd}_{0.5}\text{S}$ /ZnS multishell nanocrystals", *J. Am. Chem. Soc.*, vol. 127 (#20), pp. 7480-7488, 25 May 2005.
- [Xu 1993] Z. Y. Xu, S. R. Jin, C. P. Luo, and J. Z. Xu, "Well width dependence of the exciton lifetime in narrow GaAs/GaAlAs quantum-wells", *Solid State Commun.*, vol. 87 (#9), pp. 797-800, Sept. 1993.
- [Yao 2008] M.-Z. Yao, "The Synthesis and Luminescence Properties of Lanthanide-Based Nanoparticles for Biological Application", *Master Thesis, The University of Texas at Arlington*, Aug. 2008.
- [Zhang 2005] H. Zhang, M. Zuo, G. Li, S. Tan and S. Zhang, "Laurionite nanowires and nanoribbons: rapid mechanochemical solution synthesis and optical properties", *Nanotechnology*, vol. 16, pp. 3115-3119, 2005.

## **18. PERSONNEL SUPPORTED**

The following personnel has been supported by and/or associated with the research effort:

**Marek Osinski** (PI), Professor of Electrical and Computer Engineering (ECE), Physics and Astronomy, and Computer Science, and a CHTM faculty member. Prof. Osinski was responsible for the overall management of the program and for meeting the reporting requirements. He served as advisor of the graduate students working on this project. The level of support for Prof. Osinski was 0.25 month per year.

**Robert D. Busch** (Co-I), Director of the Nuclear Engineering Laboratory and Chief Reactor Supervisor. Dr. Busch was responsible for design of  $\gamma$ - and neutron-irradiation experiments and for analysis of experimental data taken during the irradiation experiments. He supervised the undergraduate student in the Department of Chemical and Nuclear Engineering who worked on this project. The level of support for Dr. Busch was 0.25 month per year.

**Gennady A. Smolyakov** (Co-I), Research Assistant Professor of ECE and a CHTM faculty member. Prof. Smolyakov was responsible for preparations of experimental setups for measurements of optical properties of colloidal nanocrystals, as well as for analytical modeling and numerical simulation of their interaction with  $\gamma$  and neutron radiation. He acted as a mentor to the undergraduate students from ECE and Physics and trained the students in optical measurement techniques. The level of support for Prof. Smolyakov was 2.5 month per year.

**Petr G. Eliseev**, Research Professor of ECE and a CHTM faculty member. Prof. Eliseev was responsible for analysis of optical spectra and fluorescence lifetime measurements and extraction of relevant parameters from the experimental data. The level of support for Prof. Eliseev was 0.5 month during 2008.

**Abdel-Rahman A. El-Emawy**, Research Associate Professor of ECE and a CHTM faculty member. Prof. El-Emawy was responsible for conducting x-ray diffraction measurements on colloidal nanocrystals and for maintenance of X-ray equipment. The level of support for Prof. El-Emawy was 1 month during 2008.

**Gordon Zwartz**, Postdoctoral Research Associate. Dr. Zwartz was responsible for conducting neutron and gamma irradiation experiments with CNCs. The level of support for Dr. Zwartz was 4 months during 2009.

**José M. Vargas**, Postdoctoral Research Associate. Dr. Vargas was responsible for colloidal synthesis of NCs and for conducting neutron and gamma irradiation experiments with CNCs and their interpretation. The level of support for Dr. Vargas was 6 months during the calendar year 2010.

**Daniel D. Bryant**, CHTM Building Manager. Mr. Bryant was responsible for coordination and management of technical support required during the course of the project. He was also responsible for compliance with safety requirements, including safe storage and disposal of

hazardous materials used in this project. The level of support for Mr. Bryant was 0.5 month per year.

**Michael Fairchild**, CHTM Research Engineer. Mr. Fairchild was responsible for maintenance of CHTM's Chemistry Laboratory and the Schlenk line dedicated to colloidal synthesis of nanocrystals. The level of support for Mr. Fairchild was 0.5 month in 2008.

**Andrew Frauenglass**, CHTM Research Engineer. Mr. Frauenglass was responsible for laser safety training and maintenance of optical instrumentation. The level of support for Mr. Frauenglass was 0.25 month per year.

**Ronald R. Kay**, CHTM Research Engineer. Mr. Kay was responsible for cleanroom training and technical support of CHTM's optical laboratories used in this project. The level of support for Mr. Kay was 0.5 month per year.

**Krishnaprasad Sankar**, a graduate student pursuing MS degree in Electrical Engineering, was working on this project as Graduate Research Assistant. He was responsible for colloidal synthesis and structural characterization of the nanocrystals described in this report. The level of support for Mr. Sankar was 4 months at 50% FTE in 2008. Mr. Sankar graduated With Distinction in December 2008 with a thesis entitled "*Synthesis and Characterization of Cerium-Doped Lanthanum Halide Colloidal Nanocrystals*".

**Omar Qassim**, a graduate student pursuing MS degree in Electrical Engineering, was working on this project as Graduate Research Assistant. He was responsible for computer-aided design and setup of gamma- and neutron irradiation experiments. The level of support for Mr. Qassim was 8 months at 50% FTE during the academic year 2008/2009.

**Nathan J. Withers**, a graduate student pursuing PhD degree in Electrical Engineering, was working on this project as Student Research Assistant, supported by DTRA under the SRA program and by NSF under the UNM IGERT program on Integrating Nanotechnology with Cell Biology and Neuroscience. Mr. Withers has been trained as Radiation Safety Supervisor and was authorized to conduct experiments involving radioactive materials. He was responsible for radiation hardness testing, including comprehensive optical characterization of nanocrystals prior to and after irradiation, for design of scintillation experiments, and for insertion of the nanocrystals into porous glass and aerogel hosts.

**John B. Plumley**, a graduate student pursuing PhD degree in Nanoscience and Microsystems, was working on this project as Graduate Research Assistant. He was responsible for colloidal synthesis and structural characterization of the nanocrystals described in this report. The level of support for Mr. Plumley was 10 months at 50% FTE during 2008 and 2010. He was subsequently supported by the NSF-funded UNM IGERT program on Integrating Nanotechnology with Cell Biology and Neuroscience.

**Vichiksha Shah**, a graduate student pursuing MS degree in Biomedical Sciences, was assisting in colloidal synthesis of the nanocrystals and in measurements of their optical properties. The level of support for Ms. Shah was 9 months at 50% FTE during the academic year 2009/2010.

**Darcy Kruse**, a graduate student pursuing MS degree in Physics, was involved in colloidal synthesis of scintillating nanocrystals and their characterization. She graduated in Spring 2011 semester. Her level of support during the academic year 2010/2011 was 4.5 months at 50% FTE.

**Harald Wirsching**, an international exchange student pursuing a Diploma in Physics degree with concentration in Nanotechnology at the University of Würzburg, Germany, was working on this project as Graduate Research Assistant. He was responsible development of procedures for maintaining chemical safety and waste disposal. He also participated in colloidal nanocrystal synthesis. The level of support for Mr. Wirsching was 5.25 months during the reporting period. Mr. Wirsching returned to Germany in August 2009.

**Brian A. Akins**, an undergraduate student pursuing BS degree in Electrical Engineering, was assisting in colloidal synthesis of the nanocrystals, in measurements of absorption and X-ray diffraction, and in scintillation experiments. The level of support for Mr. Akins was 5 months at 50% FTE during the academic year 2008/2009. Mr. Akins graduated in May 2009, and continued to be involved in DTRA-funded 6.1 and 6.2 DTRA projects as a graduate student.

**Antonio C. Rivera**, an undergraduate student pursuing BS degree in Physics, was assisting in TEM, SEM, FTIR, and absorption measurements of the nanocrystals. The level of support for Mr. Rivera was 15 months at 50%FTE from Dec. 2008 till May 2010. Mr. Rivera graduated in May 2010, and continued to be involved in DTRA-funded 6.1 and 6.2 DTRA projects as a graduate student, specializing in Gd-containing nanocrystals.

**Nicole Triño**, an undergraduate student pursuing BS degree in Chemical Engineering, was assisting in colloidal synthesis of the nanocrystals and their optical characterization. The level of support for Miss Triño was 5.5 months at 50% FTE during the academic year 2008/2009. Miss Triño graduated in May 2009.

**Gloria Medina**, an undergraduate student pursuing BS degree in Biochemistry, was assisting in development of procedures for colloidal synthesis of the nanocrystals described in this report. The level of support for Miss Medina was 18 months at 50% FTE over the period from June 2008 till January 2010.

**David Dixon**, an undergraduate student pursuing BS degree in Nuclear Engineering, was associated with this project and examined suitability of the MCNP simulation package, a general Monte Carlo *N*-particle transport code, to model nano-size devices. He determined that the version of MCNP available at UNM at that time could not handle structures of nanometer size.

**Carlos A. Cruz Teran**, an undergraduate student pursuing BS degree in Chemical Engineering, was assisting in development of procedures for colloidal synthesis of the nanocrystals described in this report. The level of support for Mr. Teran was 3 months at 50% FTE during the Fall 2009 semester.

**Ryan Bergsmith**, an undergraduate student pursuing BS degree in Electrical Engineering, was assisting in optical characterization of the nanocrystals. The level of support for Mr. Bergsmith was 2 months at 50% FTE during the Spring 2010 semester.

**Kai Du**, an international exchange student pursuing MS degree in Electronic Engineering at Shanghai Jiao Tong University, China, was associated with this project and examined suitability of the Geant 4 simulation package, another general Monte Carlo transport code developed at CERN in Switzerland, to model nano-size devices. We have concluded that the program was not suitable for modeling of nanosized objects.

**Shiva Bernath**, an undergraduate student pursuing BS degree in Electrical Engineering, was assisting in optical characterization of the nanocrystals. The level of support for Mr. Bernath was 7 months at 50% FTE during the academic year 2010/2011.

**Salomon Maestas**, an undergraduate student pursuing BS degree in Physics, was assisting in colloidal synthesis and optical characterization of the nanocrystals. The level of support for Mr. Maestas was 14 months over the period from November 2010 till February 2012.

**Dimple Mathew**, an undergraduate student pursuing BS degree in Biology, was assisting in insertion of the nanocrystals described in this report into polymer hosts. The level of support for Miss Mathew was 3 months at 50% FTE during the Fall 2011 semester.

## **19. PUBLICATIONS**

The following peer-reviewed publications report the results obtained under this project:

J1. N. J. Withers, K. Sankar, B. A. Akins, T. A. Memon, T.-Y. Gu, J.- J. Gu, G. A. Smolyakov, M. R. Greenberg, T. J. Boyle, and M. Osiński, “*Rapid degradation of CdSe/ZnS colloidal quantum dots exposed to gamma irradiation*”, Applied Physics Letters, vol. 93, no. 17, Art. 173101 (3 pages), 28 Oct. 2008.

J2. N. J. Withers, K. Sankar, B. A. Akins, T. A. Memon, G. A. Smolyakov, R. D. Busch, and M. Osiński, “*Synthesis and characterization of  $\text{LaF}_3\text{:}5\%\text{Ce}^{3+}$  scintillating nanocrystals*”, submitted to IEEE Transactions on Nuclear Science.

J3. A. C. Rivera, N. N. Glazener, N. C. Cook, S. R. Maestas, B. A. Akins, L. M. Armijo, J. B. Plumley, N. J. Withers, K. Carpenter, G. A. Smolyakov, R. D. Busch, and M. Osiński, “*Thermal neutron detection with  $\text{Gd}_2\text{O}_3\text{:}10\%\text{Ce}$  nanocrystals loaded into a polyvinyl toluene matrix*”, submitted to IEEE Transactions on Nuclear Science.

J4. A. C. Rivera, N. N. Glazener, N. C. Cook, S. R. Maestas, L. M. Armijo, J. B. Plumley, B. A. Akins, N. J. Withers, K. Carpenter, G. A. Smolyakov, R. D. Busch, and M. Osiński, “*Thermal neutron detection with dysprosium-containing nanocrystals suspended in toluene*”, submitted to Nanomaterials.

The following Master Thesis has been successfully defended in December 2008 and was recognized as deserving “With Distinction” annotation:

M1. K. Sankar, “*Synthesis and Characterization of Cerium-Doped Lanthanum Halide Colloidal Nanocrystals*”, M.S. in Electrical Engineering, University of New Mexico.

## **20. INTERACTIONS/TRANSITIONS**

The following papers have been presented, published in conference proceedings, accepted for presentation, or submitted awaiting acceptance at prestigious international conferences:

C1. N. J. Withers, K. Sankar, T. A. Memon, B. A. Akins, J.-J. Gu, T.-Y. Gu, G. A. Smolyakov, and M. Osiński, “*Fast-decay-time scintillation of LaF<sub>3</sub>:Ce colloidal nanocrystals*”, Technical Digest CD-ROM, Twenty Eighth Annual Conference on Lasers and Electro-Optics CLEO 2008, San Jose, CA, 5-9 May 2008, Paper CWM6.

C2. N. J. Withers, K. Sankar, B. A. Akins, T. A. Memon, T.-Y. Gu, J.-J. Gu, G. A. Smolyakov, and M. Osiński, “*Effects of gamma irradiation on optical properties of CdSe/ZnS colloidal quantum dots*”, Technical Digest CD-ROM, Twenty Eighth Annual Conference on Lasers and Electro-Optics CLEO 2008, San Jose, CA, 5-9 May 2008, Paper JThA66.

C3. M. Osiński, “*Colloidal synthesis and optical properties of lead-iodide-based nanocrystals*”, Proceedings of the International Conference on Transport and Optical Properties of Nanomaterials (ICTOPON) (M. R. Singh and R. H. Lipson, Eds.), Allahabad, India, 5-8 Jan. 2009, AIP Conference Proceedings, Vol. 1147, pp. 62-69.

C4. K. Sankar, J. B. Plumley, B. A. Akins, T. A. Memon, N. J. Withers, G. A. Smolyakov, and M. Osiński, “*Synthesis and characterization of scintillating cerium-doped lanthanum fluoride nanocrystals*”, Colloidal Quantum Dots for Biomedical Applications IV (M. Osiński, T. M. Jovin, and K. Yamamoto, Eds.), SPIE International Symposium on Biomedical Optics BiOS 2009, San Jose, CA, 24-26 Jan. 2009, Proceedings of SPIE, Vol. 7189, Paper 718909 (12 pp.).

C5. N. J. Withers, J. B. Plumley, N. D. Triño, K. Sankar, B. A. Akins, A. C. Rivera, G. A. Smolyakov, G. S. Timmins, and M. Osiński, “*Scintillating-nanoparticle-induced enhancement of radiation damage in living cells*”, Colloidal Quantum Dots for Biomedical Applications IV (M. Osiński, T. M. Jovin, and K. Yamamoto, Eds.), SPIE International Symposium on Biomedical Optics BiOS 2009, San Jose, CA, 24-26 Jan. 2009, Proceedings of SPIE, Vol. 7189, Paper 718917 (8 pp.).

C6. N. J. Withers, B. A. Akins, A. C. Rivera, J. B. Plumley, G. A. Smolyakov, and M. Osiński, “*Lead-iodide based nanoscintillators for detection of ionizing radiation*”, Chemical, Biological, Radiological, Nuclear, and Explosives (CBRNE) Sensing X (A. W. Fountain, III and P. J. Gardner, Eds.), SPIE Defense, Security, and Sensing Symposium, Orlando, FL, 14-16 April 2009, Proceedings of SPIE, Vol. 7304, Paper 73041N (12 pp.).

C7. M. Osiński, K. Sankar, N. J. Withers, J. B. Plumley, A. C. Rivera, B. A. Akins, and G. A. Smolyakov, “*Lanthanide-halide-based nanoscintillators for portable radiological detectors (Invited Paper)*”, Optics and Photonics in Global Homeland Security V and Biometric Technology for Human Identification VI (C. S. Halvorson, Š. O. Southern, B. V. K. V. Kumar, S. Prabhakar, and A. A. Ross, Eds.), SPIE Defense, Security, and Sensing Symposium, Orlando, FL, 13-16 April 2009, Proceedings of SPIE, Vol. 7306, Paper 730617 (16 pp.).

C8. N. J. Withers, K. Sankar, J. B. Plumley, B. A. Akins, T. A. Memon, A. C. Rivera, G. A. Smolyakov, and M. Osiński, “*Optimization of Ce content in  $Ce_xLa_{1-x}F_3$  colloidal nanocrystals for gamma radiation detection*”, Nuclear Radiation Detection Materials – 2009 (D. L. Perry, A. Burger, L. Franks, K. Yasuda, and M. Fiederle, Eds.), 2009 MRS Spring Meeting, San Francisco, CA, 13-17 April 2009, MRS Symposium Proceedings, Vol. 1164, Paper L07-02 (6 pp.).

C9. N. J. Withers, J. B. Plumley, B. A. Akins, G. Medina, G. Timmins, G. A. Smolyakov, and M. Osiński, “*Radiation sensitivity enhancement in cells using high-Z nanoparticles*”, Colloidal Quantum Dots for Biomedical Applications V (M. Osiński, W. J. Parak, T. M. Jovin, and K. Yamamoto, Eds.), SPIE International Symposium on Biomedical Optics BiOS 2010, San Francisco, CA, 23-25 Jan. 2010, Proceedings of SPIE, Vol. 7575, Paper 75750Z (10 pp.).

C10. M. Osiński, J. B. Plumley, N. J. Withers, B. A. Akins, G. Medina, A. C. Rivera, and G. A. Smolyakov, “*Synthesis and characterization of lanthanide halide scintillating nanocrystals for gamma radiation detection*”, Proceedings of the 2010 International Conference on Nanoscience and Nanotechnology ICONN 2010 (A. Dzurak, Ed.), Sydney, Australia, 22-26 Feb. 2010, pp. 189-192.

C11. J. B. Plumley, N. J. Withers, A. C. Rivera, B. A. Akins, J. M. Vargas, K. Carpenter, G. A. Smolyakov, R. D. Busch, and M. Osiński, “*Thermal neutron detectors based on gadolinium-containing lanthanide-halide nanoscintillators*”, Chemical, Biological, Radiological, Nuclear, and Explosives (CBRNE) Sensing XI (A. W. Fountain, III and P. J. Gardner, Eds.), SPIE Defense, Security, and Sensing Symposium, Orlando, FL, 6-8 April 2010, Proceedings of SPIE, Vol. 7665, Paper 76651F (13 pp.).

C12. N. J. Withers, J. B. Plumley, A. McBride, B. A. Akins, A. C. Rivera, N. C. Cook, G. A. Smolyakov, G. S. Timmins, and M. Osiński, “*Locally increased mortality of gamma-irradiated cells in presence of lanthanide-halide nanoparticles*”, Colloidal Quantum Dots/Nanocrystals for Biomedical Applications VI (W. J. Parak, M. Osiński, and K. Yamamoto, Eds.), SPIE International Symposium on Biomedical Optics BiOS 2011, San Francisco, CA, 22-24 Jan. 2011, Proceedings of SPIE, Vol. 7909, Paper 7909-0L (12 pp.).

C13. A. C. Rivera, N. N. Glazener, N. C. Cook, B. A. Akins, J. B. Plumley, N. J. Withers, K. Carpenter, G. A. Smolyakov, R. D. Busch, and M. Osiński, “*Detection of thermal neutrons using gadolinium-oxide-based nanocrystals*”, Chemical, Biological, Radiological, Nuclear, and Explosives (CBRNE) Sensing XII (A. W. Fountain, III and P. J. Gardner, Eds.), SPIE Defense, Security, and Sensing Symposium, Orlando, FL, 25-29 April 2011, Proceedings of SPIE, Vol. 8018, Paper 80180F (12 pp.).



C14. N. J. Withers, Y. Brandt, A. C. Rivera, N. C. Cook, L. M. Armijo, and M. Osiński, “*Effects of LaF<sub>3</sub>:Ce nanoparticles capped with polyethylene glycol on human astrocytoma cells in vitro*”, Colloidal Nanocrystals for Biomedical Applications VII (W. J. Parak, M. Osiński, and K. Yamamoto, Eds.), SPIE International Symposium on Biomedical Optics BiOS 2012, San Francisco, CA, 21-23 Jan. 2012, Proceedings of SPIE, Vol. 8232, Paper 82320R (9 pp.).

Prof. Osinski has presented the following two invited papers at international conferences abroad:

I1. M. Osiński, “*Colloidal nanocrystals for applications in detection of ionizing radiation (Invited Paper)*”, Symposium A: Nanophotonics, IEEE PhotonicsGlobal@Singapore 2008 Conference (IPGC), 8-11 Dec. 2008, Singapore.

I2. M. Osiński, “*Colloidal synthesis and optical properties of heavy-metal halide nanocrystals (Invited Paper)*”, International Conference on Transport and Optical Properties of Nanomaterials (ICTOPON), 5-8 Jan. 2009, Allahabad, India.

## **21. NEW DISCOVERIES, INVENTIONS, OR PATENT DISCLOSURES**

The following inventions have been disclosed to the Science and Technology Corporation at UNM (STC.UNM) and protected through provisional filing followed by patent applications:

P1. M. Osiński, N. J. Withers, B. A. Akins, G. A. Smolyakov, and K. Sankar, “*Lead-halide-based scintillator materials*”, United States Provisional Patent Application 61/072,636 filed on 31 March 2008, United States Utility Patent Application filed on 30 March 2009, allowed in January 2013, Notice of Allowance issued in Dec. 2012.

P2. M. Osiński, K. Sankar, B. A. Akins, G. A. Smolyakov, and N. J. Withers, “*Lanthanide-halide core/shell scintillator materials*”, United States Provisional Patent Application 61/046,035 filed on 18 April 2008, United States Utility Patent Application filed on 17 April 2009.

P3. M. Osiński, J. B. Plumley, G. A. Smolyakov, N. J. Withers, A. C. Rivera, B. A. Akins, and J. M. Vargas, “*Thermal neutron detectors based on gadolinium-containing nanoscintillators*”, United States Provisional Patent Application 61/473,071 filed on 7 April 2011, Utility Patent Application 13/506,240 filed on 5 April 2012.

P4. N. Glazener, M. Osiński, R. D. Busch, N. J. Withers, and A. C. Rivera, “*Filtratable neutron poisons*”, United States Provisional Patent Application filed on 14 December 2011.

## **22. HONORS/AWARDS**

Prof. Osinski holds the following lifetime achievement honors:

H1. In 2002, elected to the grade of *Fellow of SPIE, The International Society for Optical Engineering*, in recognition of “achievements in novel optoelectronic devices, semiconductor

laser physics, design, and simulation, wide bandgap group-III nitride light emitters, and technical optoelectronics meeting organization”.

H2. In 2003, elected to the grade of ***Fellow of the Optical Society of America (OSA)*** in recognition of contributions to the theory and simulation of semiconductor lasers.

H3. In 2007, Prof. Osinski received ***ECE Distinguished Researcher Award***, from the ECE Department of the University of New Mexico in recognition of outstanding research achievements.

H4. In 2008, Prof. Osinski was awarded a ***Gardner Zemke Professorship*** in Research Category by the ECE Department of the University of New Mexico in recognition of his continuous record of excellence in research.

**DISTRIBUTION LIST**  
**DTRA-TR-16-81**

**DEPARTMENT OF DEFENSE**

DEFENSE THREAT REDUCTION  
AGENCY  
8725 JOHN J. KINGMAN ROAD  
STOP 6201  
FORT BELVOIR, VA 22060  
ATTN: D. PETERSEN

DEFENSE TECHNICAL  
INFORMATION CENTER  
8725 JOHN J. KINGMAN ROAD,  
SUITE 0944  
FT. BELVOIR, VA 22060-6201  
ATTN: DTIC/OCA

**DEPARTMENT OF DEFENSE  
CONTRACTORS**

QUANTERION SOLUTIONS, INC.  
1680 TEXAS STREET, SE  
KIRTLAND AFB, NM 87117-5669  
ATTN: DTRIAC